Dendritic integration in hippocampal dentate gyrus granule cells

Dissertation
zur
Erlangung des Doktorgrades (Dr. rer. nat.)
der
Mathematisch-Naturwissenschaftlichen Fakultät
der
Rheinischen Friedrich-Wilhelms-Universität Bonn

vorgelegt von
Roland Krüppel
aus Neuss

Bonn 2010

Angefertigt mit Genehmigung der
Mathematisch-Naturwissenschaftlichen Fakultät
der Rheinischen-Friedrich-Wilhelms-Universität Bonn

1. Gutachter: Prof. Dr. Heinz Beck
2. Gutachter: Prof. Dr. Ulrich Kubitscheck

Tag der Promotion: 8.4.2011
Erscheinungsjahr: 2011

Erklärung

Hiermit erkläre ich, daß ich die vorliegende Dissertation selbständig angefertigt habe. Es wurden nur die in der Arbeit ausdrücklich benannten Quellen und Hilfsmittel benutzt. Wörtlich oder sinngemäß übernommenes Gedankengut habe ich als solches kenntlich gemacht.

Ort, Datum Unterschrift

Abstract

Hippocampal granule cells are critical relay stations to transfer spatial information from the entorhinal cortex into the hippocampus proper. Therefore, the integrative properties of the small-caliber granule cell dendrites were examined in this thesis, using a combination of dual somato-dendritic patch-clamp recordings and two-photon glutamate uncaging. These experiments revealed unusual integrative properties that differ substantially from other principal neurons. Due to a strong dendritic voltage attenuation, the impact of individual synapses on granule cell output is low. At the same time, integration is linear, only weakly affected by input synchrony, and is independent of the spatial location of input sites. These integrative properties can enhance contrast in the generation of place-specific firing maps from entorhinal inputs and contribute to the sparse representation of space in the dentate gyrus.

Contents

1. Introduction

1.1. Synaptic integration in neuronal dendrites

A fundamental problem in neuroscience is to understand how neurons convert synaptic input into action potential output. Most synapses of a neuron are located on its dendrites, elaborate tree-like processes emanating from the somatic compartment with a summed length of up to 1 cm. These dendritic trees are optimized to expand the space for the placement of input synapses (Chklovskii, 2004; Wen et al., 2009), form the substrate for integration of thousands of inputs (Nauta and Feirtag, 1988; Häusser et al., 2000), and function as an important stage for signal processing in a neuron (Lorente de Nó, 1935; Häusser and Mel, 2003). They are endowed with a large repertoire of passive, voltage-independent, as well as active, voltage-dependent mechanisms to process complex patterns of synaptic input (Häusser et al., 2000; Gulledge et al., 2005; Sjöström et al., 2008). The signals that finally reach the soma are highly transformed versions of the original inputs; thus dendritic processing has a profound influence on the input-output transformation of neurons.

1.1.1. Passive properties of neuronal dendrites

The passive properties provide the backbone for all electrical signaling in dendritic trees. A passive dendritic tree can be described as a linear system using cable theory as introduced by Rall (1962): a time-dependent voltage change $V_j(t)$ at a location j in response to an arbitrary current input $I_i(t)$ at location i can always be expressed as

$$V_j(t) = K_{ij} \otimes I_i(t), \tag{1.1}$$

where $K_{ij}(t)$ is the impulse response or Green's function of the linear system and $\otimes$ is the convolution operator. The Fourier transform $\widetilde{K}_{ij}(f)$, where f is the temporal frequency, is referred to as transfer impedance and relates current inputs to voltage

changes by Ohm's law. Its stationary or dc value $\widetilde{K}_{ij}(f=0)$ is the transfer resistance. A current input at a location j causes a voltage change at this point that is proportional to the input impedance $\widetilde{K}_{jj}(f)$. The exact structures of K_{ij} and $\widetilde{K}_{ij}$ depend on the morphology and the electrotonic properties of the dendritic tree; nevertheless, some general relations for the steady state can be derived (see e.g. Koch, 1999).

We will start with the description of the local voltage change due to an activated synapse. A current input at location j caused by opening of synaptic channels upon presynaptic (or uncaging-evoked) transmitter release can be described by Ohm's law as

$$I_{syn,j}(t) = g_{syn,j}(t) \cdot \left(V_j(t) - E_{syn}\right), \tag{1.2}$$

where $g_{syn,j}$ is the synaptic conductance and E_{syn} its reversal potential. The local steady-state membrane potential reached upon synaptic activation at j can then be expressed with the help of the input impedance as

$$V_j = \frac{\widetilde{K}_{jj} E_{syn} g_{syn,j}}{1 + \widetilde{K}_{jj} g_{syn,j}}. \tag{1.3}$$

For small synaptic inputs with $g_{syn,j} \cdot \widetilde{K}_{jj} \ll 1$, the membrane potential changes only little and the input can be approximated as a current source by

$$V_j \approx \widetilde{K}_{jj} E_{syn} g_{syn,j}. \tag{1.4}$$

In this case of small input the local membrane potential changes linearly with the input. Equation 1.3 implies that the local membrane potential V_j does not increase indefinitely with $g_{syn,j}$. Indeed, the local membrane potential saturates when it approaches the synaptic equilibrium potential. This can be seen explicitly in the case of large synaptic input with $g_{syn,j} \cdot \widetilde{K}_{jj} \gg 1$ where the synaptic membrane potential saturates at

$$V_j \approx E_{syn}. \tag{1.5}$$

Any further increase in the synaptic conductance does not change the membrane potential, since there is no more net driving force across the membrane for ions conducted by the synaptic channels.

After this description of the *local* membrane potential change upon synaptic activation, we will examine the somatic impact of a synapse in the dendritic tree: a

current injection I_j at location j in the dendrite leads to a voltage change at the soma of

$$V_{soma} = \widetilde{K}_{j,soma} \cdot I_j \tag{1.6}$$

where $\widetilde{K}_{j,soma}$ is the transfer impedance between the dendritic site j and the soma. An important property of the transfer impedance[1] is its symmetry, i.e. $\widetilde{K}_{j,soma} = \widetilde{K}_{soma,j}$. A current injected at location j generates the same membrane potential change at the soma as a somatic current injection of the same magnitude generates at location j. A second property of $\widetilde{K}$ is its positivity $\widetilde{K}_{j,soma} \leq \widetilde{K}_{jj}$: the input impedance is always larger than the transfer impedance, thus the biggest membrane potential change is always at the point of current injection. Additionally, the larger the electrotonic distance between the soma and j is, the smaller is the transfer impedance. Hence, $\widetilde{K}_{j,soma}$ is related to the degree of coupling between the two sites. Importantly, since the maximal local membrane potential change is limited by the synaptic equilibrium potential, the impact of any input at the soma is also limited.

Until now we only introduced steady-state relationships, but due to the membrane capacitance both input and transfer impedance are frequency-dependent. The membrane becomes increasingly more conductive as the frequency of an injected current increases and thus the impedances show a low-pass behavior,

$$\left|\widetilde{K}_{j,soma}\left(f\right)\right| < \left|\widetilde{K}_{j,soma}\left(f'\right)\right| \tag{1.7}$$

for any $f > f'$.

The relationship between the local and the somatic voltage can be quantified by the voltage transfer ratio or voltage attenuation

$$A_{j,soma} = \frac{V_{soma}}{V_j} = \frac{\widetilde{K}_{j,soma}}{K_{jj}}. \tag{1.8}$$

The inequality of $\widetilde{K}_{j,soma}$ and $\widetilde{K}_{jj}$ ensures that, unlike the transfer impedance, the voltage transfer is not symmetrical ($A_{j,soma} \neq A_{soma,j}$), but depends on the direction of signal propagation. Since $K_{jj} > K_{j,soma}$, it follows that attenuation of signals propagating in the direction of the soma is much stronger than vice versa: $A_{soma,j} > A_{j,soma}$.

For a small synaptic input at location j that can be described as a current source

[1] This and most other properties also hold true for any two points in the neuron.

the somatic membrane potential change is given by

$$V_{soma} = \widetilde{K}_{j,soma} I_{syn,j}. \tag{1.9}$$

Hence, the variability of the somatic membrane potential amplitude with synaptic location is governed by the variation of $\widetilde{K}_{j,soma}$ throughout the dendritic tree. Writing this expression with the help of the voltage attenuation as

$$V_{soma} = A_{j,soma} V_j = A_{j,soma} \widetilde{K}_{jj} I_j \tag{1.10}$$

it becomes clear that for a current source synapse the somatic voltage is a function of both the voltage attenuation and the local input impedance. If, as in many neurons (Jaffe and Carnevale, 1999), $\widetilde{K}_{jj}$ increases with distance from the soma, the voltage attenuation may decrease, while—contrary to intuition—the somatic voltage V_{soma} remains relatively unaffected by the location of the synapse. This passive normalization of synaptic input was demonstrated for e.g. CA3 pyramidal neurons (Jaffe and Carnevale, 1999).

The above relations are derived for only one synaptic input. Colocalization of multiple inputs in time and space, however, leads to nonlinear interactions between the inputs. As an example, coincident activation of two colocalized inputs at location j in the dendritic tree leads to sublinear summation in the soma:

$$V_{soma} = \frac{g_{syn1,j} E_{syn} \widetilde{K}_{j,soma}}{1 + \left(g_{syn1,j} + g_{syn2,j}\right) \widetilde{K}_{jj}} + \frac{g_{syn2,j} E_{syn} \widetilde{K}_{j,soma}}{1 + \left(g_{syn1,j} + g_{syn2,j}\right) \widetilde{K}_{jj}}. \tag{1.11}$$

This sublinear summation is caused by two mechanisms. First, activation of one synapse increases the membrane conductance ($g_{syn1,j} + g_{syn2,j}$ in the denominator) and acts as a shunt for the other activated synapse (Barrett and Crill, 1974; Bernander et al., 1991). Second, the depolarization caused by the one synapse reduces the driving force for the other synapse, since the local membrane potential approaches the synaptic equilibrium potential. Both effects are increasingly more pronounced for stronger and more numerous inputs and depend on the electrotonic distance between the synapses. When two synaptic sites at i and j are electrotonically remote,

i.e. $\widetilde{K}_{ij} \to 0$, the somatic voltage is simply the linear sum of both synapses

$$V_{soma} = \frac{g_{syn1,i} E_{syn} \widetilde{K}_{i,soma}}{1 + g_{syn1,i} \widetilde{K}_{ii}} + \frac{g_{syn2,j} E_{syn} \widetilde{K}_{j,soma}}{1 + g_{syn2,j} \widetilde{K}_{jj}}. \tag{1.12}$$

The interactions between synapses also depend on their relative timing (Tamás et al., 2002) and, for synapses located on dendritic spines, on the electrotonic isolation of the synaptic site at the spine head from the dendritic shaft (Shepherd et al., 1985; Nimchinsky et al., 2002; Araya et al., 2006).

It has been observed experimentally that small excitatory postsynaptic potentials (EPSPs) sum linearly (Langmoen and Andersen, 1983; Cash and Yuste, 1998, 1999) and that summation of large EPSPs becomes sublinear (Langmoen and Andersen, 1983), indicating the importance of driving force loss and local shunting on dendritic integration. A sublinear summation of inputs might be beneficial for certain computational tasks, for example coincidence detection in the auditory system (Agmon-Snir et al., 1998).

At the end of this section we want to emphasize that most of the relations introduced above are derived for the stationary case, but under physiological conditions synaptic input is evidently far from stationary. Solving analytically for the voltage responses to transient conductance changes is difficult and thus the coupled differential equations describing electrical signaling in a neuron are mostly solved numerically (but see e.g. Butz and Cowan, 1974; Cao and Abbott, 1993). It is important to note that synaptic saturation and sublinear addition of nearby synapses are phenomena also described for transient synaptic inputs (Rall and Rinzel, 1973; Rinzel and Rall, 1974; Koch et al., 1982).

1.1.2. Voltage-gated ion channels in neuronal dendrites

The presence of voltage-gated and transmitter-gated ion channels in postsynaptic sites and dendrites makes the integration of inputs much more complex in that an analytical treatment as introduced above is no longer possible (Häusser et al., 2000; Gulledge et al., 2005; Sjöström et al., 2008). These active elements modulate dendritic integration and can also trigger regenerative events in many neuronal dendrites (Häusser et al., 2000).

A plethora of voltage-gated ion channels is present in dendrites, but only a

selection of prominent examples of currents influencing synaptic integration is presented here:

- Activation of the dendritic transient potassium current I_A can prevent large, rapid dendritic depolarizations and thereby regulate propagation of dendritic signals. The I_A contributes to the attenuation of backpropagating action potentials (Kampa and Stuart, 2006), reduces EPSP size (Hoffman et al., 1997), and takes part in the sublinear summation of EPSPs in CA1 pyramidal cells (Cash and Yuste, 1999).

- The hyperpolarization activated cation current I_h is deactivated upon depolarization and thus enhances repolarization of the membrane potential. It shortens EPSP waveforms and thereby reduces the time window over which temporal summation takes place (Magee, 1998, 1999; Liu and Shipley, 2008; Williams and Stuart, 2000).

- Dendritic sodium currents can be activated by synaptic input (Magee and Johnston, 1995b) and elevate EPSP amplitudes (Lipowsky et al., 1996). The backpropagation of somatic action potentials into the dendrites can be actively boosted by activation of dendritic sodium channels (Spruston et al., 1995).

- Calcium channels, mostly of the low-voltage activated T-type, are functionally expressed in many dendrites, e.g. of CA1 pyramidal neurons (Magee and Johnston, 1995a), layer V pyramidal neurons (Markram and Sakmann, 1994), or cerebellar Purkinje cells (Mouginot et al., 1997). These channels can be locally activated by synaptic input (Magee and Johnston, 1995b) and can amplify EPSPs (Gillessen and Alzheimer, 1997). Other, high-voltage activated calcium channels in dendrites are usually only activated by backpropagating action potentials. All dendritic calcium channels can also activate local, calcium-dependent signaling cascades.

Above a certain voltage or current threshold regenerative events, termed dendritic spikes, can be generated in many dendrites incorporating voltage-gated conductances. There are two different nonlinear mechanisms, using voltage-dependent ion channels, that can generate these dendritic spikes:

- Many types of neurons incorporate voltage-gated sodium channels in their dendrites which support sodium-mediated, fast dendritic spikes (Wong et al.,

1979; Benardo et al., 1982; Turner et al., 1989; Poolos and Kocsis, 1990; Andreasen and Lambert, 1995). These fast sodium spikes were also observed in experiments in-vivo (Kamondi et al., 1998). The generation of these sodium spikes depends on a fast dendritic depolarization; they can be triggered by spatially clustered and highly synchronous input or strong local current injection (Losonczy and Magee, 2006; Golding and Spruston, 1998). Dendritic sodium spikes can be undetectable at the soma due to filtering in the dendrites; but they nevertheless lead to supralinear integration, probably by facilitation of local NMDA receptor unblock (Nettleton and Spain, 2000). Depending on where sodium spiked are generated in the dendritic tree, they can also reach the soma and have profound influence on the timing of action potential output (Golding and Spruston, 1998; Ariav et al., 2003). It was also demonstrated that neuronal output can be sensitive to the detection of even sub-millisecond coincident input via dendritic sodium spikes (Softky, 1994).

- Activation of calcium channels can lead to large calcium-dominated dendritic spikes. A calcium spike initiation zone in the apical stem dendrite of layer V pyramidal neurons was shown to overcome the very weak coupling between the apical tuft and the soma in these cells (Amitai et al., 1993; Larkum et al., 1999; Schiller et al., 1997; Larkum et al., 2003). Calcium spikes can also occur in terminal branches of CA1 pyramidal neurons, either alone (Wei et al., 2001) or in combination with dendritic sodium spikes (Andreasen and Lambert, 1995; Golding et al., 1999). Usually, NMDA receptors contribute to calcium spike evoked depolarizations but are not mandatory for its initiation (Wei et al., 2001).

1.1.3. Transmitter-gated ion channels in neuronal dendrites

There are two main types of transmitter-gated ion channels present in excitatory spine synapses on dendrites. The first is the α-amino-3-hydroxy-5-methyl-4-isoxazole propionic acid (AMPA) type glutamate receptor, which usually has a linear current-voltage relationship and can thus be described by the linear cable theory introduced above. The second type is the N-methyl-D-aspartate (NMDA) type glutamate receptor. At resting membrane potential a proportion of NMDA receptors are blocked by magnesium ions. Upon depolarization this block is relieved and the total synaptic

conductance is increased by the now unblocked NDMA receptors (Mayer et al., 1984). Both receptors have a reversal potential near 0 mV. The NMDA receptors have a unitary channel conductance of 50 ps and are roughly equi-permeable to Na^+ and K^+ and higher permeable for Ca^{2+}. AMPA type receptors usually have a unitary channel conductance of 0.2–50 pS and are permeable[2] to Na^+ and K^+. The activation of NMDA receptors is much slower (10-50 ms) than the gating of AMPA receptors and their deactivation time course is much longer than the timecourse of glutamate in the synaptic cleft and thus will dictate the duration of the synaptic current (Dingledine et al., 1999). This nonlinear current-voltage relationship of NMDA receptors can lead to local boosting effects (see fig. 1.1), even in an otherwise passive dendritic tree: "For unto every one that hath shall be given, and he shall have abundance" (King James Bible, Matthew 25:29). This boosting contributes to overcome the loss of local driving force and can linearize the summation of large EPSPs (Cash and Yuste, 1998). Depending on the exact properties of the dendrites and synapses, e.g. the ratio of maximal NMDA to AMPA receptor conductances, summation can even be supralinear (Carter et al., 2007). Interestingly, activation of I_A can counteract the NMDA receptor-dependent boosting, which makes the actual summation rule even more complex and probably dependent on developmental regulation of both NMDA receptor and I_A expression (Cash and Yuste, 1999). Unblock of NMDA receptors can also be achieved by dendritic sodium spikes. After an initial fast sodium spike a slow large depolarization which is dependent on NMDA receptors is often observed (Losonczy and Magee, 2006). A high proportion of activated NMDA receptors can not only boost EPSPs but also trigger regenerative events (see fig. 1.1), termed NMDA spikes (Schiller and Schiller, 2001). These NMDA spikes can be evoked in thin basal dendrites (Schiller et al., 2000; Polsky et al., 2004; Major et al., 2008) and also in the thin dendrites of the apical tuft of layer V pyramidal neurons (Larkum et al., 2009). Like fast dendritic sodium spikes, NMDA spikes are generated by synchronous activation of neighboring synapses. Their threshold can be lowered by sodium and calcium conductances, but these are not mandatory for the NMDA spike initiation.

[2] AMPA receptors lacking the GluR2 subunit are also permeable to calcium (Hollmann et al., 1991).

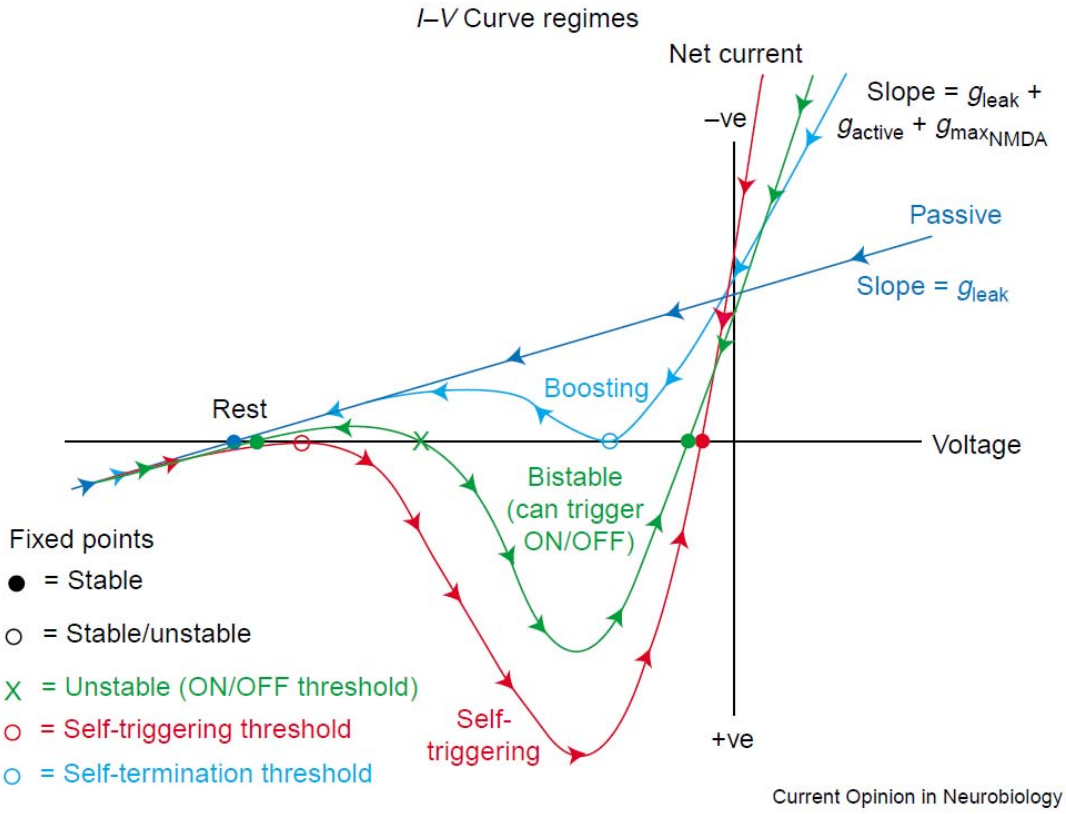

Figure 1.1.: Different regimes of NMDA receptor effects and their current-voltage relations. Arrows indicate the flow of a system towards a fix point indicated by circles. A passive membrane generates a linear I-V curve and the systems moves back to the resting potential upon any input (dark blue). Systems with voltage-dependent elements as glutamate-bound NMDA receptors generate N-shaped I-V curves. The cyan curve shows a regime of input boosting by activation of NMDA receptors upon progressive depolarization. When the total NMDA conductance is large enough, regenerative NMDA spikes can be triggered and the I-V curve (green) crosses the zero axis at three points with the middle point being the spike threshold (green cross). When the total NMDA conductance is further increased the threshold and resting points move together until they merge and the spikes become self-triggered (red). Reprinted from Current Opinion in Neurobiology, 11, J. Schiller and Y. Schiller, "NMDA receptor-mediated dendritic spikes and coincident signal amplification", pp. 343–348, Copyright (2001), with permission from Elsevier.

1.1.4. Dendritic computation

Both boosting mechanisms, by voltage-gated ion channels and by NMDA type glutamate receptors, are voltage-dependent and activate with upon depolarization. Thus, most effective for the activation of boosting mechanisms is locally clustered and synchronous input. This type of input is also most efficient in triggering of local regenerative events, although the restrictions in the synchrony are higher. The dependence on the input pattern has profound implications for the computations that dendrites can perform: it was for example demonstrated in a computational study that local boosting by clustered synapses with a high NMDA receptor content can lead to input pattern discrimination in a layer V pyramidal neuron (Mel, 1992).

The integration in neuronal dendrites that permit dendritic spikes is bimodal: triggering a dendritic spikes switches the local integration from sublinear or linear to a supralinear mode. Therefore, synaptic input integrated with a spike has a higher impact than input that failed to generate such a dendritic spike (Mel, 1993; Ariav et al., 2003). Neurons with dendrites that allow spike generation can thus perform complex computations in two-stages. In the first stage of synaptic integration every dendritic branch can act as an independent detector of clustered and synchronous input. In the second stage all branch outputs are integrated in the soma and, if threshold is reached, an action potential output is generated. The dendritic preprocessing can largely expand the computational capabilities of a neuron (Poirazi and Mel, 2001; Poirazi et al., 2003). In addition, the local spiking can be both trigger (Golding et al., 2002; Remy and Spruston, 2007) and substrate for local short- (Remy et al., 2009) and long-term plasticity (Losonczy et al., 2008). Hence, every single dendritic compartment can work not only as a detector of synchronous and clustered input but also as a storage device for these input patterns. Thereby the total information storage capacity of a neuron can be greatly enhanced in comparison to "simple" synaptic plasticity.

The electrotonic structure (Carnevale et al., 1997), the distribution of ion channels (Migliore and Shepherd, 2002; Nusser, 2009), and receptors (Nusser and Mody, 2002; Huntley et al., 1994), and thus are the computational capabilities, are different in many types of neurons.

The next section will focus on the dentate gyrus, in particular the dentate gyrus granule cells, their function and their dendritic tree. The chapter will then end with a set of questions connecting both topics.

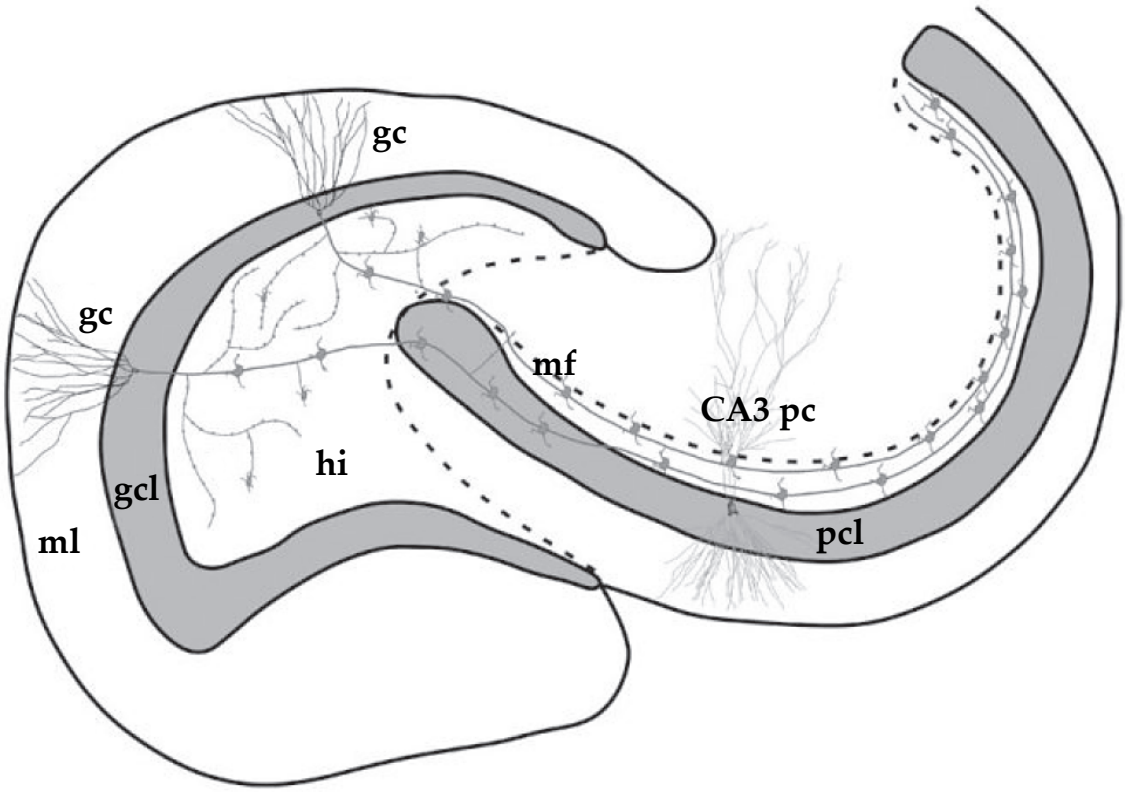

Figure 1.2.: Anatomy of the dentate gyrus. Schematic representation of a part of a horizontal hippocampal brain slice. Depicted are granule cells (gc) in the cell layer of the dentate gyrus (gcl) and their dendrites in the molecular layer (ml). The mossy fiber axons (mf) of the granule cells traverse the hilus (hi) towards the CA3 region and on their course they terminate with mossy fiber boutons on CA3 pyramidal cells (CA3 pc), which are located in the pyramidal cell layer (pcl). Reprinted from Progress in Brain Research, 163, D.G. Amaral, H.E. Scharfman, P. Lavenex, "The dentate gyrus: fundamental neuroanatomical organization (dentate gyrus for dummies)", pp. 3–22, Copyright (2007), with permission from Elsevier.

1.2. Functional anatomy of the dentate gyrus

The dentate gyrus is an allocortical structure and part of the hippocampal formation in the medial temporal lobe of all mammals (Golgi, 1886; Doinikow, 1908; Squire et al., 2004). The granule cells are the major excitatory cell type in the dentate gyrus. Their axons, the mossy fibers, project to the CA3 region of the hippocampus proper (fig. 1.2).

1.2.1. Anatomy of the dentate gyrus

The dentate gyrus[3] forms a longitudinally folded sheet that stretches between the septal and temporal poles of the hippocampal formation. Typical for an allocortical structure, the dentate gyrus consists of three layers (ml, gcl, and hi in fig. 1.2). The outermost, the molecular layer, contains only few cells and comprises mostly of afferent fibers and dendrites of granule cells. The second layer, the granule cell layer, contains the densely packed cell bodies of the granule cells and is 4–8 somata thick. The third and deepest layer is the hilus, interposed between the upper (suprapyramidal) and lower (infrapyramidal) blades of the dentate gyrus and bordered by the CA3 subfield of the hippocampus proper.

The major excitatory cell population in the hilus are the mossy cells which provide feed-back excitation to the granule cell population (Scharfman, 1995). Another excitatory cell group are the semilunar granule cells, sparsely distributed in the molecular layer, which are probably important for up-states in the dentate network (Larimer and Strowbridge, 2009). As in every cortical region, a variety of inhibitory interneurons is present in the dentate gyrus network (Freund and Buzsáki, 1996). The most abundant interneurons are the basket cells, located in the granule cell layer, that densely innervate the perisomatic region and the dendrites of granule cells. Other types of inhibitory interneurons are chandelier or axo-axonic cells (targeting granule cell axons), HICAP cells (hilar border neurons with ascending axons and dendrites), MOPP cells (neurons with axons and dendrites in the molecular layer), and HIPP cells (featuring hilar dendrites and ascending axons). All, except the MOPP cells, are contacted by mossy fiber collaterals and thus can provide feedback inhibition to the granule cells.

The input to the dentate gyrus derives from a number of sources. The most prominent afferent connection is the perforant path which originates in layer II of the entorhinal cortex (EC) and terminates in the outer two thirds of the molecular layer (Blackstad, 1958; Amaral and Witter, 1989; Deller, 1998; Hjorth-Simonsen and Jeune, 1972; Hjorth-Simonsen, 1972). The entorhinal cortex is a multimodal association cortex with six layers that receives inputs from all sensory areas in the brain (from olfactory structures and via the peri- and postrhinal cortices) and from the subicular complex in the hippocampus (van Strien et al., 2009). It can be divided into two

[3]The name “dentate gyrus”, or “gyrus dentatus” in Latin, derives from the serrated macroscopic form of the human dentate gyrus (Aranzi, 1587).

parts, the lateral entorhinal cortex (LEC) and the medial entorhinal cortex (MEC), based on their perforant path projections. Both the MEC and LEC project to the full septotemporal extent of the dentate gyrus. However, the LEC projects via the lateral perforant path to the outer third and the MEC via the medial perforant path to the the middle third of the dentate molecular layer (Hjorth-Simonsen, 1972). These different termination zones are readily discernible in the classical Timm staining for heavy metals. Both parts of the perforant path exhibit a rough topographic organization: the mediolateral axis of the EC is mapped onto the proximodistal axis along the granule cell dendrites in the molecular layer of the dentate gyrus (Tamamaki and Nojyo, 1993; Tamamaki, 1997; Amaral et al., 2007).

Several other afferent projections terminate in the dentate gyrus: the middle molecular layer is the target of fibers that originate in the subicular complex and travel in the alveus. Commissural and associational inputs from the contralateral hilus are mostly targeting the proximal third of the molecular layer (Patton and McNaughton, 1995). Among other hippocampal structures the dentate gyrus also receives several modulatory inputs, e.g. cholinergic fibers from the medial septum (Leranth and Hajszan, 2007).

1.2.2. Morphology of granule cells

The granule cells are the principal cells of the dentate gyrus (Golgi, 1886; Lorente de Nó, 1934). There are an estimated 1.2 million granule cells per hemisphere in rats (West et al., 1991; Rapp and Gallagher, 1996) and around 5 million in the monkey (Seress, 1988). Although there is considerable literature about adult neurogenesis of granule cells and their functional incorporation into the dentate gyrus network (Toni et al., 2008; Clelland et al., 2009), the absolute cell number seems to be stable (Rapp and Gallagher, 1996), arguing for a continuous turnover. Granule cells possess relatively small, spherical somata of 8–12 µm diameter—hence their name—and are exclusively located in the granule cell layer.

They have a characteristic, cone-shaped apical dendritic tree that extends throughout the molecular layer of the dentate gyrus (see gc in fig. 1.2). The tips of the dendritic branches of mature granule cells in the supra- or infrapyramidal blades end at the hippocampal fissure or at the pial surface of the lateral ventricle, respectively. The spread of the cone-shaped dendritic field[4] is up to 283 µm in transverse

[4]Values given here are from studies on rats. See Vuksic et al. (2008) and Williams and Matthysse

and 194 µm in longitudinal directions (Desmond and Levy, 1982). The apical dendritic tree comprises of on average 29 segments and the total dendritic length varies from 2800 µm to 3500 µm, for granule cells in the infra- and suprapyramidal blades, respectively. Typically, a granule cell possesses 2 first order dendrites and nearly 70% of the branching of the dendritic tree occurs within the proximal one-third of the molecular layer. Approximately 25% of branchpoints are located in the middle third and only 6% in the outer third of the molecular layer. This implies that 10–12% of the total dendritic length lie within the granule cell layer and 25% in the proximal one-third of the molecular layer. The residual 60% of the total dendritic length are located in the outer two thirds of the molecular layer in termination zone of the medial and lateral perforant paths (Desmond and Levy, 1982; Claiborne et al., 1990). Basal dendrites, normally absent in rodents, have been observed in 10–20% of primate and human granule cells (Seress and Mrzljak, 1987; Seress and Frotscher, 1990), and also in rodent animal models of chronic epilepsy (Spigelman et al., 1998; Kron et al., 2010). The dendrites are richly covered with spines in the whole molecular layer; the observed spine densities are 1.6 $^{\text{spines}}/_{\mu\text{m}}$ and 1.3 $^{\text{spines}}/_{\mu\text{m}}$, in the supra- and infrapyramidal blades, respectively[5]. This leads to an estimate of approximately 5600 and 3640 excitatory inputs onto a single granule cell (Desmond and Levy, 1985; Amaral et al., 2007) much lower than for example the 30.000 excitatory inputs onto a CA1 pyramidal cell (Megias et al., 2001).

The axons of the dentate gyrus granule cells originate from the basal poles of the somata, travel in the hilus, and form the dense mossy fiber bundle in the CA3 region, which is visible with bare eye as the stratum lucidum. On their course, the mossy fibers terminate with big presynaptic boutons on the apical dendrites of a small number (15–20) of CA3 pyramidal neurons. The many collaterals (with approximately 200 synapses) of mossy fibers contact interneurons in the hilus and inhibitory interneurons in the CA3 region.

(1983) for mouse studies, Baer et al. (1985) for cattle, sheep, and goat, John et al. (1997) for monkey, and Seress and Frotscher (1990) for morphological properties of human granule cells. All of these studies show that the morphology of granule cell dendrites is similar across mammals, although, in particular the vertical extent of the dendritic tree is larger in bigger brains.

[5] In contrast to many light microscopic studies several electron microscopic studies report a higher spine density of 2–3.4 $^{\text{spines}}/_{\mu\text{m}}$ (Hama et al., 1989; Trommald and Hulleberg, 1997).

1.2.3. Electrophysiology of granule cells

In vitro studies

After early studies that explored the electrophysiology of single granule cells using sharp microelectrodes (Dudek et al., 1976; Brown et al., 1981; Fricke and Prince, 1984; Biscoe and Duchen, 1985), later studies employed whole-cell or perforated patch-clamp techniques to investigate subthreshold and action potential properties of granule cells (Staley et al., 1992; Spruston and Johnston, 1992). Dentate granule cells show a number of electrophysiological characteristics that distinguish them from pyramidal cells and interneurons in the hippocampal formation: mature granule cells have a hyperpolarized resting membrane potential of -84 mV (Staley et al., 1992) and an approximate input resistance of 150 MΩ. The input resistance varies considerably; it is substantially higher (up to 4 GΩ) in immature granule cells and decreases with the maturation stage of the cells (Liu et al., 1996; Schmidt-Hieber et al., 2004; Ye et al., 2005). In response to hyperpolarizing current steps granule cells show only small sags and rebound depolarizations in comparison to e.g. CA1 pyramidal neurons. The action potential threshold of granule cells at -49 mV is relatively far from the resting membrane potential (Staley et al., 1992). A single action potential features a short afterdepolarization and a long lasting afterhyperpolarization(Zhang et al., 1993). On prolonged firing, granule cells exhibit spike frequency adaptation. The properties of granule cells in other mammals are similar to the ones observed in the rat (for human data see Isokawa et al., 1991; Williamson et al., 1993; Dietrich et al., 1999 and for monkey data see John et al., 1997). There were early attempts to obtain information about the dendritic membrane properties by direct sharp-microelectrode recordings from dendrites (Fricke and Prince, 1984), by peeling of decay time constants from long and short current injections (Brown et al., 1981; Durand et al., 1983), or by inference from extracellular field potential recordings (Jefferys, 1979). In a careful modeling study Schmidt-Hieber et al. (2007) matched a compartmental model made from detailed morphological reconstructions to voltage transients from dual somatic recordings.

However, knowledge about the different voltage-gated currents and the underlying channel composition of granule cells is limited to the somatic compartment and to the axonal mossy fiber boutons. Even regarding the somatic conductances pyramidal cells in the hippocampus appear to be studied far more. The current most studied in granule cells is clearly the A-type potassium current, which is

somatically expressed at a density of 10 $pA/\mu m^2$ (Beck et al., 1992; Riazanski et al., 2001), comparable to the density measured in CA1 somata (Hoffman et al., 1997). A-type potassium current densities in dendrites are probably low and the total current density is developmentally downregulated (Strecker and Heinemann, 1993). Somatic sodium conductances in granule cells are also comparable to the density found in CA1 pyramidal neuron somata (Ketelaars et al., 2001). Indirect evidence—somato-dendritic nucleated patches and laminar field potentials—point to a quite low density of sodium channels in granule cell dendrites. As is indicated by the absence of a pronounced sag in current-clamp recordings, granule cells seem to lack h-currents (Stabel et al., 1992). Granule cells also express calcium channels, but in a lower density than hippocampal pyramidal neurons. The most prominent calcium current is the N-type, additionally some T-type and nearly no L-type currents are detectable (Blaxter et al., 1989; Fisher et al., 1990; Eliot and Johnston, 1994; Beck et al., 1997). As in other neurons, calcium channels shape the form of the action potential afterpotentials (Zhang et al., 1993; Valiante et al., 1997; Aradi and Holmes, 1999) cooperatively with SK and BK calcium-activated potassium channels (Beck et al., 1997). The sodium conductance in mossy fiber boutons (49 mS/cm^2, Engel and Jonas, 2005, comparable to other axonal compartments of e.g. layer V pyramidal neurons Kole et al., 2008) is higher than in the somata of granule cells, which indicates a differential expression in distinct subcellular compartments.

In vivo studies

The earliest studies on granule cell activity were performed in anesthetized rabbits and demonstrated that stimulation of the perforant path evokes EPSPs in intracellular recordings of granule cells (Andersen et al., 1966; Lømo, 1971). Later studies, also under anesthesia, were carried out in rats (Muñoz et al., 1990). After first anecdotal evidence by Rose et al. (1983), a place field firing behavior of granule cells was shown by Jung and McNaughton (1993) in recordings in freely moving rats, similar to what was reported earlier from CA1 and CA3 neurons (O'Keefe and Dostrovsky, 1971; Thompson and Best, 1989). Behavioral modulation of granule cell place fields was then first shown in the groundbreaking study of Leutgeb et al. (2007a), that provided evidence for pattern separation in the dentate gyrus, as discussed below. Granule cells in that study fired with peak frequencies of 11.55±8.16 Hz in their place field, comparable to CA1 pyramidal cells. Strikingly, only a very small proportion

(2–5%) of the whole granule cell population seems to be active (Chawla et al., 2005; Alme et al., 2010) even in population discharge events like sharp wave ripples (Jill Leutgeb, personal communication). This is in striking contrast to the CA1 and CA3 cell populations, where 40% of cells are active during exploratory behavior and an even higher proportion discharges during a sharp wave ripple event (Buzsáki, 1986). Preliminary data from a whole-cell patch-clamp study in awake rats indicate a high frequency of subthreshold events and a very low action potential firing rate in granule cells in-vivo. The excitatory synaptic input granule cells receive in-vivo seems to be correlated to the local field potential, which shows substantial power in the gamma frequency band (Pernia-Andrade and Jonas, 2009).

The downstream effects of granule cell firing were also studied in-vivo and it was discovered that the mossy fiber synapses are strong and can conditionally "detonate" CA3 pyramidal neurons (McNaughton and Morris, 1987; Henze et al., 2002). The effect of granule cell stimulation in vitro is, however, mainly inhibitory because of strong recruitment of feed-forward inhibition (Lawrence and McBain, 2003; Mori et al., 2004, 2007).

1.2.4. Computational properties of the dentate gyrus

In his seminal theoretical study of hippocampal function Marr (1971) saw the dentate gyrus merely as collector for the CA3 autoassociative network. McNaughton and Morris (1987) proposed the idea that the dentate gyrus performs a pattern separation: similar input patterns are converted into orthogonal representations in the dentate gyrus, which expand the number of memories that can be stored and faithfully read out in the CA3 network. A number of theoretical studies have incorporated the proposed pattern separation feature of the dentate gyrus (Treves and Rolls, 1992; Papp et al., 2007; Acsády and Káli, 2007). However, first experimental evidence for pattern separation in the dentate gyrus was found much later in a series of elegant experiments (Leutgeb et al., 2005; Leutgeb and Moser, 2007). By slowly morphing the cage in which granule cells of a rat were recorded, Jill Leutgeb and her coworkers could show that these granule cells show a strong modulation of their place field firing pattern upon small changes in the environment. This sensitivity in the firing pattern was much more pronounced in granule cells than in CA3 pyramidal cells. These findings were supported by a study using knock-out animals in which the essential NMDA receptor subunit NR1 was deleted specifically in the dentate gyrus

granule cells. These animals then showed a decreased performance in a spatial discrimination task (McHugh et al., 2007).

A conserved function of the hippocampal formation is spatial navigation (Mittelstaedt and Mittelstaedt, 1980; Ekstrom et al., 2003; Moser et al., 2008). Sequences of place cell activity during theta cycles compress the animal's spatial trajectory in time and are probably underlying the animal's orientation in the environment (Skaggs et al., 1996; Jensen and Lisman, 2000). It is an open question how place specific firing emerges in the hippocampus. After the discovery of grid like spatial firing patterns in medial entorhinal cortex layer II neurons (Fyhn et al., 2004; Hafting et al., 2005; Moser et al., 2008) it became clear that granule cells are the ideal subject to study the emergence of place field firing. The grid firing patterns of the EC layer II neurons is conveyed by the strong perforant path projection to the granule cells. It could be shown in simple computational models that by selecting certain grid inputs onto a granule cell, this granule cell can fire preferentially at the one location with the maximal overlap of the presynaptic grid fields (Solstad et al., 2006; Ujfalussy et al., 2009; Franzius et al., 2007; Hayman and Jeffery, 2008; Molter and Yamaguchi, 2008a,b; Si and Treves, 2009; de Almeida et al., 2009).

1.3. Key questions

The functional properties of granule cell dendrites are mostly uncharted until now (but see Fricke and Prince, 1984; Schmidt-Hieber et al., 2007). To uncover them is of great importance to understand the computational functions dentate gyrus granule cells perform in the hippocampal network. Several questions have guided this thesis:

- How do physiological signals like action potentials and excitatory postsynaptic potentials travel through the dendrites of granule cells and what are the underlying basic electrophysiological properties of granule cell dendrites?
- Do granule cells express frequency-dependent mechanisms in their dendrites and how does this influence the integration time window?
- How is synchronous and clustered input integrated in granule cell dendrites and do the dendrites show active properties similar to the ones described, e.g. for CA1 pyramidal neurons?

- Are simple computational models of place field generation in granule cells compatible with the integration and transfer of synaptic input in the dendritic tree?

2. Materials and Methods

2.1. Animals and preparation

All experiments were performed on horizontal hippocampal slices of 21–41 days old Wistar rats. For the preparation the animals were deeply anesthetized with ketamine (100 $^{mg}/_{kg}$, Pfizer) and xylazine (15 $^{mg}/_{kg}$, Bayer) and then decapitated. The brain was quickly removed and put in ice-cold sucrose artificial cerebrospinal fluid (sucrose ACSF, see appendix A.1). Horizontal 300 µm thick slices were cut with a vibratome (HM 650 V, Microm) in ice-cold sucrose ACSF. Slices were then incubated and gradually rewarmed to 35 °C for 30 minutes. Afterwards, slices were held in normal ACSF (see appendix A.1) for up to 6 hours. The temperature in the submerged recording chamber was 33 °C in all experiments, unless otherwise noted. All animal experiments were conducted in accordance with the guidelines of the Animal Care and Use Committee of the University of Bonn.

2.2. Somatic and dendritic patch-clamp

Hippocampal dentate granule cells were visually identified using oblique illumination contrast with a custom built condenser diaphragm and a 60x water immersion objective (LUMPLFLN, Olympus or Plan Apo, Nikon) on an upright microscope. The whole-cell patch-clamp configuration was then established with a potassium-gluconate based intracellular solution (see appendix A.2) which additionally contained 50–200 µM Alexa 488 or Alexa 594 hydrazide sodium salt (Invitrogen) for the visualization of the cell morphology. Patch pipettes were made from borosilicate glass capillaries (GB150F-8P, Science Products) with a horizontal puller (P-97, Sutter). Electrode resistance of the somatic patch pipettes was 2–6 MΩ and the resulting series resistance was 8–20 MΩ. The average resting membrane potential of granule cells was -70.9±0.5 mV (n=186 cells). Current-clamp recordings were performed with

a Multiclamp 700B (Molecular Devices) or a BVC-700 amplifier (Dagan). Voltage-clamp recordings were performed with an Axopatch 200B amplifier (Molecular Devices). Voltage or current signals were digitized with a Digidata 1320 or 1440 (Molecular Devices) at 50 kHz and recorded using Clampex 9 or 10.2 (Molecular Devices) on a PC running Windows XP. Voltages were not corrected for the calculated liquid-junction potential of +14 mV.

After obtaining whole-cell access, the cells were visualized in most experiments with a two-photon fluorescence microscope (Ultima, Prairie Technologies) using an ultrafast pulsed infrared titan-sapphire laser (Chameleon Ultra, Coherent) tuned to 840–920 nm. Laser intensity was controlled with a Pockels cell (350-80 LA, Conoptics). Laser power at the slice surface was usually lower than 20 mW to prevent photodamage or electrical breakdown. A pixel dwell time of 2.4–4.0 µs and fly-back laser blanking were used. Fluorescence light was collected with the objective, reflected by a dichroic mirror (660 dcxxr, Chroma), separated by a filter cube (525/70, 575 dcxr, 607/45, Prairie), and detected by a photomultiplier (R3896 multialkali, Hamamatsu). The photomultiplier voltage was set to ~800 V, the preamplifier gain was 1, and the 1.25 MHz filter bank of the preamplifier was enabled. mirror (660 dcxxr, Chroma), separated by a filter cube (525/70, 575 dcxr, 607/45, Prairie), and detected by a photomultiplier (R3896 multialkali, Hamamatsu). The photomultiplier voltage was set to ~800 V, the preamplifier gain was 1, and the 1.25 MHz filter bank of the preamplifier was enabled.

For dual somato-dendritic patch-clamp recordings the whole-cell patch-clamp configuration of the cell soma was established first, as described above. In addition to the two-photon fluorescence, the transmitted infrared laser light was collected with the substage condenser (1.4 NA oil, U-AAC, Olympus), spatially filtered by a custom-made sector pass condenser diaphragm, and subsequently reflected onto a substage photomultiplier. This allowed online overlay of fluorescence and oblique contrast images (infrared scanning gradient contrast, IR-SGC) of the dendrite and the dendritic patch pipette (Nevian et al., 2007). The zooming capability of the two-photon microscope allowed a precise approach of the dendritic membrane with the small dendritic patch pipette. These dendritic patch pipettes were made from thick walled borosilicate glass (GB200F-8P, Science Products) with a horizontal puller (P-97, Sutter) and used without further modifications. Pipette resistance was 20–30 MΩ and the resulting series resistance was 94±17 MΩ. The dendritic series resistance was not correlated to the distance of the recording site to the soma

(Pearson's r=-0.52, p=0.57). The input resistance at the dendritic site was correlated to the distance of the recording site (Pearson's r=0.74, p=0.024). Only the pipette capacitance compensation circuit of the Dagan BVC-700 amplifier was found to faithfully compensate the capacitance of the high-resistance pipettes needed for patching small caliber dendrites (Thomas Nevian, personal communication, and fig. 3.1f, g). Since the capacitance is inversely proportional to the logarithm of the pipette wall thickness and proportional to its length, it is beneficial to have just a short pipette segment with thin walls to achieve a low pipette capacitance. Thus, great care was taken to obtain a stubby pipette shape with a short shank. Additionally, the liquid level in the slice chamber was kept low to immerse on a small part of the pipette. To be able to compensate the high series resistances arising from the small pipettes the N=0.01 headstage of the BVC-700 amplifier was used.

2.2.1. Problems with accessing small caliber dendrites

The direct patch-clamp recordings from small caliber dendrites are not without difficulties. Problems arise from the small caliber pipettes, which have a high resistance and a large stray capacitance resulting in a high series resistance and a strong filtering effect, if these are not meticulously compensated. When the series resistance is not compensated correctly, the current flowing through the pipette creates a voltage drop over the combined pipette and access resistances, in addition to the voltage over the cell membrane. Thus, all voltages measured in the current-clamp bridge mode of the amplifier are offset to the real ones. The compensation of the pipette capacitance, on the other hand, is necessary to faithfully measure fast voltage signals which would otherwise be affected by the filter of the pipette RC circuit. The cutoff frequency of a RC filter is $f_c = \frac{1}{2\pi R \times C}$; an estimated residual capacitance of 1.3 pF after compensation (Brette et al., 2008) and in parallel a pipette resistance of 25 MΩ lead to a cutoff frequency of 4.9 kHz. Thus, with optimal compensation, fast voltage transients like action potentials can accurately be measured. Overcompensation is only stable in a very small range and will result in boosting of high frequency components, i.e. mainly increased noise. Additionally, exact capacitance correction is necessary for a correct compensation of the series resistance (Wilson and Park, 1989).

2.2.2. Control experiments for dendritic patch-clamp recordings

To show experimentally that fast voltage transients can faithfully be recorded with high-resistance pipettes dual somatic patch-clamp recordings with a low resistance and a high resistance pipette (pipette resistances 4.1±0.1 MΩ and 22.5±3.8 MΩ, respectively) were performed as described above. Pipette capacitance and series resistance were carefully compensated (series resistances 15.3±2.4 MΩ and 52.8±5.2 MΩ, respectively). Single action potentials were triggered by short current injections (3 ms) through either the low- or high-resistance pipettes. Action potential amplitudes were not significantly different in the recordings from both electrodes (average action potential amplitude in the high-resistance pipette recording was 98±0.2% of the low resistance pipette, p=0.25, n=3), did not depend on the pipette through which the current was injected, and had the same shape in both recordings (fig. 2.1a–b). Voltage transients of injected mock EPSCs (see below) also had the same amplitude and time course in the recordings from both pipettes (fig. 2.1c).

However, studies assessing the properties of small caliber dendrites with different methods came to seemingly incompatible results. For example, the voltage imaging studies of Zhou et al. (2008) and Antic (2003) and the patch-clamp study of Nevian et al. (2007) (see also Kampa and Stuart, 2006) of thin basal dendrites of cortical layer V neurons disagree about the amount of dendritic backpropagation of action potentials. While Zhou et al. (2008) appear to see a nearly undisturbed backpropagation (as judged from the action potential half width), Nevian et al. (2007) see a strong distance-dependent attenuation of backpropagating action potentials. When looking closely at the figures in both publications, one can see that their measurements of the action potential latency nevertheless agree. The measurements of the action potential half widths are probably also compatible: Nevian et al. (2007) see an increase from 0.5 ms at the soma to 1.5 ms at 150 µm distance from the soma. Zhou et al. (2008) see a constant dendritic half width of 1.2 ms, but their somatic action potential already has a half-width of 1 ms. That the dendritic half width is constant and bigger than the somatic one could be explained by a temporal undersampling in the voltage imaging experiments (sampling interval 0.37 ms). Compare also our fig. 3.2c, f where a large amplitude decrease is observed even for dendritic locations near the soma, but the action potential half-width is nearly identical to the half-width measured at the soma. Taken together, action potential shape is probably not a good parameter to assess attenuation of backpropagating action potentials but is used regularly in

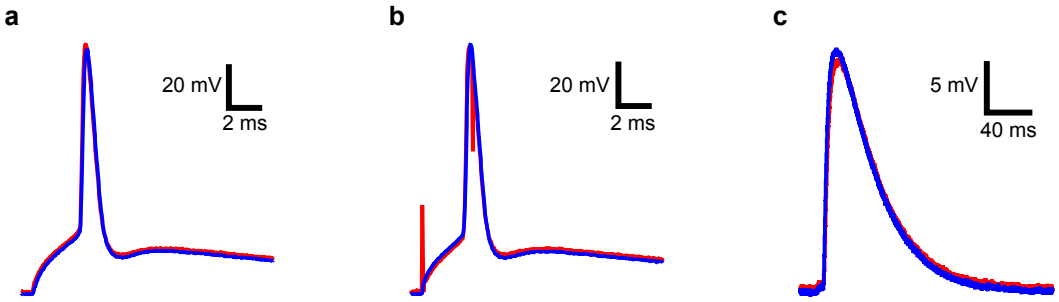

Figure 2.1.: Dendritic patch-clamp control experiments. **a**, Example traces of dual somatic whole-cell patch-clamp recording with pipettes of 4.1 MΩ (blue trace) and 30 MΩ (red trace) resistance. Action potential was evoked by a 3 ms current injection through the low resistance pipette. On average action potential amplitude in the high resistance pipette recording was 98±0.2% of the low resistance pipette recording (n=3 cells). **b**, Same recording as in a but action potential was evoked by current injection through the high resistance pipette. **c**, Example voltage traces of EPSC waveform injection through the high resistance pipette.

voltage imaging studies (but see Palmer and Stuart, 2009).

2.2.3. Further protocols

In experiments using sucrose stimulated synaptic release a patch pipette was filled with normal ACSF that additionally contained sucrose (300 mM) and tetrodotoxin (TTX, 1 µM). This pipette was then placed adjacent to the dendrite of interest (~20 µm) and pressure was applied to the pipette via a syringe to eject the high osmolarity solution.

For the experiments determining the NMDA to AMPA ratio, near unitary EPSCs were evoked by a stimulation pipette made from theta glass pulled into patch pipette form and filled with normal ACSF (see fig. 2.2). This bipolar stimulation pipette was connected to a stimulus isolator (AM-Systems, Model 2100) and constant current voltage was applied (100 µs pulse, average stimulation voltage 32.9±6.4 V) every 2 seconds. Cesium based intracellular solution for those experiments (see appendix A.2) additionally contained the sodium channel blocker QX314 (chloride salt, 5 mM) and the extracellular solution contained no magnesium and the γ-aminobutyric acid type A ($GABA_A$) receptor blocker bicuculline methiodid (10 µM). The dentate gyrus was isolated from the CA3 region and the entorhinal cortex by two cuts to avoid a spread of epileptiform activity into the dentate.

Sinusoidal current injections with increasing frequency (ZAP protocol) were

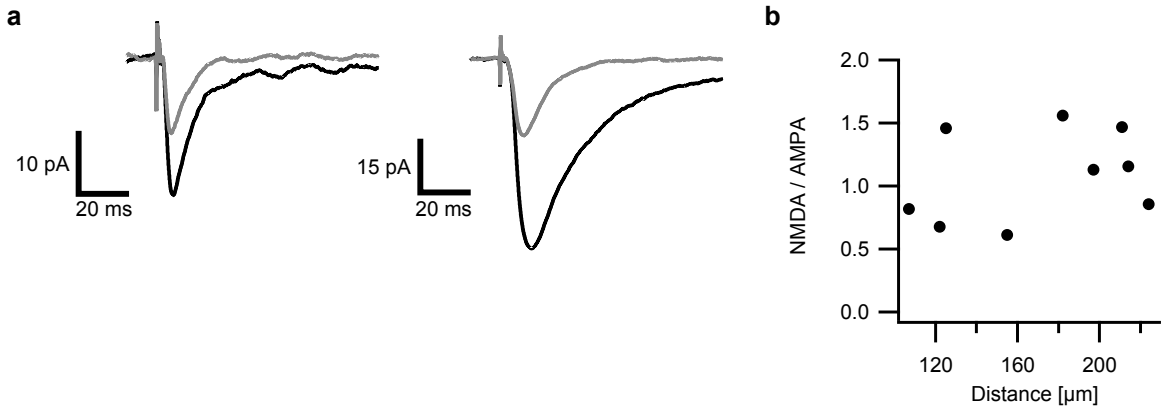

Figure 2.2.: NMDA/AMPA ratio of perforant path synapses. **a**, Example traces of perforant path stimulation EPSCs. Left panel shows a stimulation in the medial perforant path (stimulation distance from the soma ~107 µm), right panel shows a stimulation in the lateral perforant path (stimulation distance ~211 µm). Black traces correspond to the average EPSCs under control conditions (average of 90 stimulations) and gray traces correspond to average EPSCs after wash in of D-APV (50 µM, average of 90 stimulations). ACSF did not contain Mg^{2+} and cells were voltage-clamped at -75 mV with a cesium based intracellular solution. **b**, NMDA/AMPA ratio of minimal stimulated EPSPs versus distance of stimulation site from soma (n=9). The ratio does not correlate with distance (Pearson's r=0.311, p=0.43), with an average ratio of 1.08±0.12. In the termination area of the MPP (85 µm><166 µm) the AMPA/NMDA was as 0.89±0.19 (n=4), in the termination area of the LPP (>166 µm) the ratio was 1.23±0.13 (n=5).

generated in Igor Pro by the expression

$$I_{ZAP}(t = 0 \ldots 30\,\mathrm{s}) = \sin\left(2.7 \cdot t^2\right), \tag{2.1}$$

which resulted in a maximum frequency of ~25 Hz.

Single mock EPSCs were modeled in Igor Pro by the function

$$I_{EPSC}(t) = -e^{\frac{t}{1.3\,\mathrm{ms}}} + e^{\frac{t}{8.3\,\mathrm{ms}}} \tag{2.2}$$

and compound mock EPSCs were subsequently constructed by addition of the single mock EPSCs with a certain time interval.

All chemicals were obtained from Sigma-Aldrich unless otherwise noted. D-(-)-2-amino-5-phosphonopentanoic acid (D-APV), QX314, and tetrodotoxin (TTX) were obtained from Tocris/Biozol, 4-aminopyridine (4-AP) from Acros Organics, and tetraethylammonium chloride hydrate (TEA) from Merck.

2.3. Two-photon uncaging

Patch-clamp recordings from granule cells were performed in whole-cell mode and the cell morphology was visualized with a two-photon microscope as described above. Additionally a patch pipette with a large aperture or a broken patch pipette, filled with normal ACSF and 10–15 mM MNI-caged-glutamate (Tocris), was placed adjacent to the dendrite of interest and slight overpressure was applied (4–30 mbar depending on the pipette diameter). A picture of the dendritic segment of interest was made with high zoom to allow the identification of single spines. Single uncaging spots were placed near the heads of 7–14 spines and at the same time the laser wavelength was changed to 725 nm and the Pockels cell zero-point was adjusted accordingly. After this, a pointing protocol was started on the two-photon microscope which illuminated all the spines sequentially with an inter-spine interval of 500 ms and an uncaging duration of 0.2–1 ms. Then, in the same protocol, increasing numbers of spines were illuminated nearly simultaneously with the same uncaging duration, a galvanometric mirror move time between each spot of 0.1–0.5 ms and an interval of 1 s between each group of illuminated spines. The somatic voltage transients and the Pockels cell signals, that indicate the exact times of the uncaging, were recorded in Clampex.

2.3.1. Control experiments

Because of their inertia, the galvanometric mirrors do not immediately settle to their new position when moving from one spot to another. The position, as monitored on the feed-back output of the galvanometric mirror driver, oscillates sinusoidally with nearly exponentially decreasing amplitude around the final position. When the two positions are on opposite sides of the field of view the settling time constant is in the range of 0.2 ms. Since interposition intervals for single spine and synchronous spine uncaging are different, this contributes to an error in the comparison between the measured and the calculated sum EPSPs. This error is most serious for very short uncaging durations and interposition times (e.g. 0.2 ms and 0.1 ms) but in our experiments the distances between consecutive spines were usually only a small fraction of the field of view. It was also confirmed that both 0.2 ms and 1 ms uncaging pulses evoke a similar ensemble of synaptic and presumably perisynaptic glutamate receptors. Therefore granule cells were patch-clamped in whole cell mode with a cesium based intracellular solution (see appendix A.2) and held in voltage-clamp mode. Uncaging with 0.2 ms and 1 ms pulse length was performed on the same spines at -90 mV and +40 mV holding potentials. At a holding potential of -90 mV only AMPA receptors are activated, whereas at +40 mV both AMPA and NMDA receptors, which are then fully unblocked, are activated. The ratios of the peak current amplitudes at +40 mV and -90 mV were calculated and did not significantly differ for 0.2 ms and 1 ms uncaging duration (fig. 2.3).

2.4. Two-photon calcium imaging

The whole-cell patch-clamp configuration was established at soma of dentate granule neurons and cell morphology was visualized with a two-photon microscope as described above. The potassium gluconate based intracellular solution (see appendix A.2) was slightly modified: ethylene glycol tetraacetic acid (EGTA) was replaced by 500 µM Oregon Green BAPTA 1 (OGB-1), a high affinity calcium dye (K_d=170 nM). The calcium chelator EGTA is usually included to compensate the washout of physiological intracellular calcium buffers, but together with the additional calcium dye/buffer OGB-1 calcium transients are undetectable (data not shown). Cells were filled with dye for 10–15 min prior to the recording. Linescans along or transverse to dendritic segments were performed with a laser wavelength

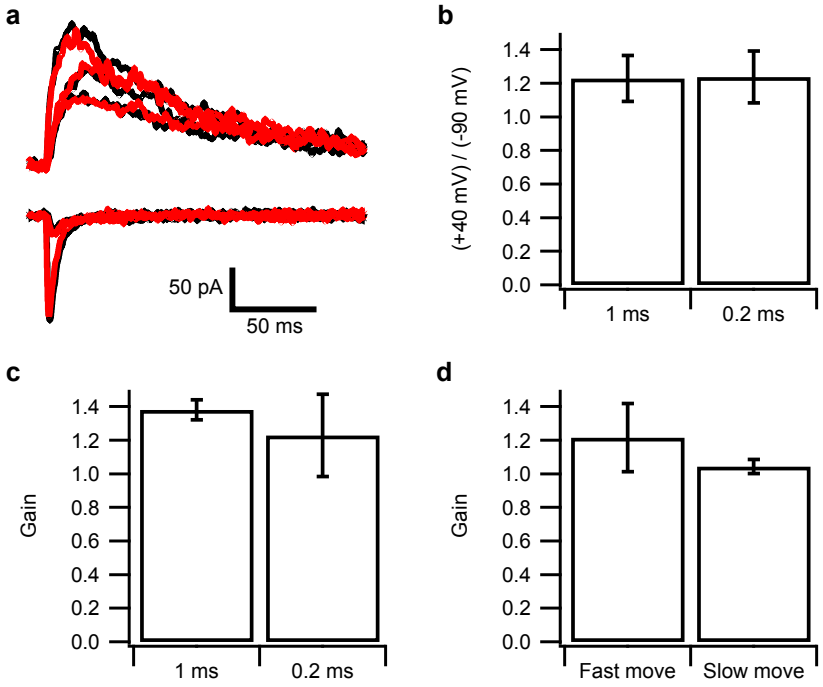

Figure 2.3.: Control experiments for two-photon uncaging of glutamate. **a**, Example current traces for three different single spine uncaging-evoked EPSCs (gluEPSCs) with a holding potential of either -90 mV (bottom traces) or +40 mV (top traces) for uncaging pulses of 1 ms (black) or 0.2 ms duration (red). **b**, Quantification of the current amplitude ratios for the 1 ms and 0.2 ms uncaging pulses. No significant difference was observed (Wilcoxon-signed-rank test, p=0.38, n=59 spines). **c**, Comparison of the observed gains (calculated as the linear fit to the measured versus the arithmetic sum of uncaging-induced EPSPs) for 1 ms and 0.2 ms uncaging pulses. No significant difference was observed (Wilcoxon-rank test, p=0.32, n=47 and n=5). **d**, Comparison of the observed gains for fast (0.1 ms) and slow (0.5 ms) galvanometric mirror moving times. No significant difference was observed (Wilcoxon-signed-rank test, p=0.81, n=5).

Table 2.1.: Conductance densities (in $^{S}/_{cm^2}$) in different compartments.

	Axon	Axon initial segment	Soma	Dendrites
Na_T	0.096	0.5	0.025	-
K_A	0.01	0.01	0.01	-
K_DR	0.003	0.003	0.003	-
$Leak$	0.001	0.001	0.0001	-

of 830 nm and a line frequency of 425–750 Hz. Time locked to the linescan, short somatic current injections (3 ms) were performed to evoke single action potentials. OGB-1 signals were spatially averaged over the whole extent of the linescan that contained the center of the dendrite of interest. OGB-1 fluorescence signals are quantified as peak intensity after the onset of the somatic current injection minus the average baseline intensity before (usually 100 ms), divided by the average baseline intensity $\Delta F/F$.

2.5. Modeling with NEURON

The NEURON simulation environment allows the simulation of detailed electrical cable models of neuronal morphologies and advanced channel kinetics (Carnevale and Hines, 2006). Reconstructed morphologies from Schmidt-Hieber et al. (2007) were imported from ModelDB (accession number 95960). A specific membrane capacitance of $C_m = 1\,^{\mu F}/_{cm^2}$ was used in all compartments and corrected for temperature and spine membrane area (Koch, 1999). The specific membrane resistance R_m and the specific axial resistance R_a that were derived by Schmidt-Hieber et al. (2007) were used and corrected for temperature and spine membrane area. Example values for the somatic compartment of one model cell (cell number 7) were $C_m = 0.96538\,^{\mu F}/_{cm^2}$, $R_m = 19694\,\Omega \cdot cm^2$, and $R_a = 133.043\,\Omega \cdot cm$. A temperature of 33 °C was assumed in all simulations. The granule cells were endowed with different conductances (see table 2.1) and the following properties:

The transient sodium current model of Migliore et al. (1999) was obtained from ModelDB (accession number 2796, Hines et al., 2004) and implemented as follows:

$$i_{Na_T} = \overline{g}_{Na} \cdot m^3 \cdot h \cdot s \cdot (E - E_{Na}) \tag{2.3}$$

with m, h, and s corresponding to the gating parameters for fast activation and fast inactivation. The equations describing activation were as follows

$$\alpha_m = \frac{0.4\,\mathrm{ms}^{-1} \cdot (E + 30\,\mathrm{mV})}{1 - e^{-(E+30\,\mathrm{mV})/7.2\,\mathrm{mV}}} \tag{2.4}$$

$$\beta_m = \frac{-0.124\,\mathrm{ms}^{-1} \cdot (E + 30\,\mathrm{mV})}{1 - e^{(E+30\,\mathrm{mV})/7.2\,\mathrm{mV}}} \tag{2.5}$$

$$\tau_m = \frac{1}{Q(T) \cdot (\alpha_m + \beta_m)} \tag{2.6}$$

$$m_\infty = \frac{\alpha_m}{\alpha_m + \beta_m}. \tag{2.7}$$

The equations describing inactivation were

$$\alpha_h = \frac{0.03\,\mathrm{ms}^{-1} \cdot (E + 45\,\mathrm{mV})}{1 - e^{-(E+45\,\mathrm{mV})/1.5\,\mathrm{mV}}} \tag{2.8}$$

$$\beta_h = \frac{-0.01\,\mathrm{ms}^{-1} \cdot (E + 45\,\mathrm{mV})}{1 - e^{(E+45\,\mathrm{mV})/1.5\,\mathrm{mV}}} \tag{2.9}$$

$$\tau_h = \frac{1}{Q(T) \cdot (\alpha_h + \beta_h)} \tag{2.10}$$

$$h_\infty = \frac{1}{1 + \exp\left((E + 50\,\mathrm{mV})\,/4\,\mathrm{mV}\right)}. \tag{2.11}$$

The Q_{10} value of 2 was adopted from Migliore et al. (1999). The sodium equilibrium potential E_{Na} was set to +60 mV.

An A-type potassium current model which was modeled after Beck et al. (1992), was obtained from ModelDB (accession number 3344) and implemented as follows:

$$i_{K_A} = \overline{g}_{K_A} \cdot n \cdot l \cdot (E - E_K)\,, \tag{2.12}$$

with n and l corresponding to the gating parameters for activation and inactivation The equations describing the activation and inactivation were

$$\alpha_n = \exp\left(\frac{-0.0015 \cdot (E + 73.1\,\mathrm{mV}) \cdot 9.648 \cdot 10^4}{8.315 \cdot (273.16 + T)}\right) \tag{2.13}$$

$$\beta_n = \exp\left(\frac{-0.0015 \cdot 0.7 \cdot (E + 73.1\,\mathrm{mV}) \cdot 9.648 \cdot 10^4}{8.315 \cdot (273.16 + T)}\right) \tag{2.14}$$

$$\tau_n = \frac{\beta_n}{Q(T) \cdot 0.3\,\mathrm{ms}^{-1} \cdot (1 + \alpha_n)} \tag{2.15}$$

$$\alpha_l = \exp\left(\frac{0.002 \cdot (E + 73.1\,\mathrm{mV}) \cdot 9.648 \cdot 10^4}{8.315 \cdot (273.16 + T)}\right) \tag{2.16}$$

$$\beta_l = \exp\left(\frac{0.002 \cdot 0.65 \cdot (E + 73.1\,\mathrm{mV}) \cdot 9.648 \cdot 10^4}{8.315 \cdot (273.16 + T)}\right) \tag{2.17}$$

$$\tau_l = \frac{\beta_l}{Q(T) \cdot 0.02\,\mathrm{ms}^{-1} \cdot (1 + \alpha_l)}. \tag{2.18}$$

The Q_{10} value was set to 3.
A delayed rectifier potassium current was modeled after Carnevale and Hines (2006) with values from Schmidt-Hieber et al. (2008) as

$$i_{K_{DR}} = \overline{g}_{K_{DR}} \cdot n^4 \cdot (E - E_K)\,, \tag{2.19}$$

with the following activation dynamics:

$$\alpha_n = \frac{0.01 \cdot (E + 55\,\mathrm{mV})}{1 - e^{-0.1 \cdot (E + 55\,\mathrm{mV})}} \tag{2.20}$$

$$\beta_n = 0.125 \cdot e^{-(E + 60\,\mathrm{mV})/80\,\mathrm{mV}}. \tag{2.21}$$

The potassium equilibrium potential E_K was set to -90 mV.

Synapses were modeled with bi-exponential functions. The equations for the AMPA type portion were as follows:

$$i_{AMPA} = \overline{g}_{max} \cdot \left(e^{\frac{t}{\tau_{decay}}} - e^{\frac{-t}{\tau_{rise}}}\right) \cdot (E - 0\,\mathrm{mV})\,, \tag{2.22}$$

with $\tau_{rise} = 0.05\,\mathrm{ms}$ and $\tau_{decay} = 2\,\mathrm{ms}$. The equations for the NMDA type portion of the synapses were as follows:

$$i_{NMDA} = \overline{g}_{max} \cdot \left(e^{\frac{-t}{\tau_{decay}}} - e^{\frac{-t}{\tau_{rise}}}\right) \cdot B(E) \cdot (E - 0\,\mathrm{mV}) \tag{2.23}$$

$$B(E) = \left(1 + \eta \cdot \left[Mg^{2+}\right] \cdot e^{(-\gamma \cdot E)}\right)^{-1}, \tag{2.24}$$

with $\tau_{rise} = 0.33\,\mathrm{ms}$, $\tau_{decay} = 50\,\mathrm{ms}$, $\eta = 0.05\,\mathrm{mM}^{-1}$, and $\gamma = 0.06\,\mathrm{mV}^{-1}$. The low value of η was needed to account for the partly NMDA receptor unblock observed at resting membrane potentials in granule cells (Keller et al., 1991). The magnesium concentration $\left[Mg^{2+}\right] = 2\,\mathrm{mM}$ was set to the value used in the experimental part of the thesis.

The number of segments in each section of the neuronal morphologies was computed by the d_lambda rule, as described in Carnevale and Hines (2006):

$$n_{seg} = \left\lfloor \frac{\frac{L}{d_\lambda \cdot \lambda_f(f)} + 0.9}{2} \right\rfloor \cdot 2 + 1. \tag{2.25}$$

2.5.1. Network model

The network model simulated the firing of entorhinal cortex grid cells dependent on the position of a virtual animal traversing a rectangular 1 m x 1 m environment. The animal ran on a fine zig-zag course through the environment with a speed of 0.5 m/s (Diba and Buzsáki, 2008). For each point $\vec{r}$ on the animals trajectory the firing probability $p(\vec{r})$ was computed as in Solstad et al. (2006) as

$$\begin{aligned} k_1(\vec{r}) &= \frac{4\pi}{g\sqrt{6}} \left(\cos\left(\varphi + \frac{\pi}{12}\right) + \sin\left(\varphi + \frac{\pi}{12}\right)\right)(r_x - d_x) \\ &\quad + \left(\cos\left(\varphi + \frac{\pi}{12}\right) - \sin\left(\varphi + \frac{\pi}{12}\right)\right)(r_y - d_y) \qquad (2.26) \\ k_2(\vec{r}) &= \frac{4\pi}{g\sqrt{6}} \left(\cos\left(\varphi + 5\frac{\pi}{12}\right) + \sin\left(\varphi + 5\frac{\pi}{12}\right)\right)(r_x - d_x) \\ &\quad + \left(\cos\left(\varphi + 5\frac{\pi}{12}\right) - \sin\left(\varphi + 5\frac{\pi}{12}\right)\right)(r_y - d_y) \qquad (2.27) \\ k_3(\vec{r}) &= \frac{4\pi}{g\sqrt{6}} \left(\cos\left(\varphi + 3\frac{\pi}{4}\right) + \sin\left(\varphi + 3\frac{\pi}{4}\right)\right)(r_x - d_x) \\ &\quad + \left(\cos\left(\varphi + 3\frac{\pi}{4}\right) - \sin\left(\varphi + 3\frac{\pi}{4}\right)\right)(r_y - d_y) \qquad (2.28) \\ p(\vec{r}) &= f_{max} \cdot \frac{2}{3}\left(\cos(k_1(\vec{r})) + \cos(k_2(\vec{r})) + \cos(k_3(\vec{r}))\right) + \frac{1}{6}, \qquad (2.29) \end{aligned}$$

with the rotation/phase of the grid map φ, the spatial offset (d_x, d_y), the actual position $\vec{r} = (r_x, r_y)$ of the simulated animal, the maximal firing frequency in the center of a grid corner f_{max}, and the grid size/spacing g. Before the simulation was started the spike times for the grid cells were determined based on the calculated trajectory and firing probabilities. For each grid cell a `VecStim` object, containing the calculated spike times, was then connected with NEURON's `NetCon` mechanism to the AMPA and NMDA parts of synapses. These synapses were placed at random locations in the dendritic tree in a certain distance range from the soma. The placing algorithm was modified from Li and Ascoli (2006). The simulation was then started and the somatic voltage was recorded continuously and written

to disc after the simulation ended. Network simulation time was usually 1000 s with a time step of 100 µs. To speed up simulations the NEURON source code was compiled on a 64 bit system (Intel i5 running Ubuntu Linux) with custom optimizations (`-march=core2 -O2`). The computation time for one simulation run was approximately 5½ hours. For a discussion of inhibition in the model see appendix A.4.

2.6. Data analysis

All data analysis was performed using custom routines in Igor Pro 6 (Wavemetrics). Image preparation and montage was done with ImageJ (NIH) and Fiji (http://pacific.mpi-cbg.de/wiki/index.php/Fiji). All values given are arithmetic mean plus minus standard error of the mean , unless otherwise noted. Mostly nonparametrical statistical tests were used, since they do not depend on the (often unsatisfied) condition of the normal distribution of data.

3. Results

3.1. Attenuation of voltage signals in granule cell dendrites

3.1.1. Strong and uniform attenuation of EPSPs

Combined two-photon excitation fluorescence and infrared-scanning gradient contrast was used to obtain dual somato-dendritic recordings from granule cells (fig. 3.1a, see materials and methods, section 2.2). This method of patch-clamping fine dendritic processes was only recently established to gain access to fine dendrites of cortical layer V pyramidal neurons (Nevian et al., 2007; Larkum et al., 2009). Using this approach, we studied the voltage transfer properties of dentate gyrus granule cell dendrites. Injection of mock EPSCs at the dendritic recording electrode yielded a strong voltage attenuation from the dendritic to the somatic electrodes (somatic EPSP amplitude divided by dendritic EPSP amplitude, S/D, fig. 3.1d, red: dendritic recording, blue: somatic recording, n=7). In a subset of these recordings, EPSPs were also evoked by local application of high osmolar solution (eEPSPs, fig. 3.1b, average eEPSP in c), and displayed a similar attenuation from the dendritic to the somatic recording electrode (Wilcoxon signed rank test p=0.25, n=3). Plotting the EPSP attenuation for dual somato-dendritic recordings revealed that the voltage attenuation was remarkably similar for dendritic sites ranging 50–250 µm from the granule cell somata (fig. 3.1e). We showed in a series of control experiments that voltage transients in fine dendrites can be accurately measured with high-resistance electrodes by dual somatic whole-cell patch-clamp recordings (see materials and methods sections 2.2.1 and 2.2.2 and fig. 2.1).

3.1.2. Strong attenuation of backpropagating action potentials

We observed a strong attenuation also for action potentials evoked by somatic current injections and backpropagating into granule cell dendrites (bAPs, fig. 3.2a, b, see

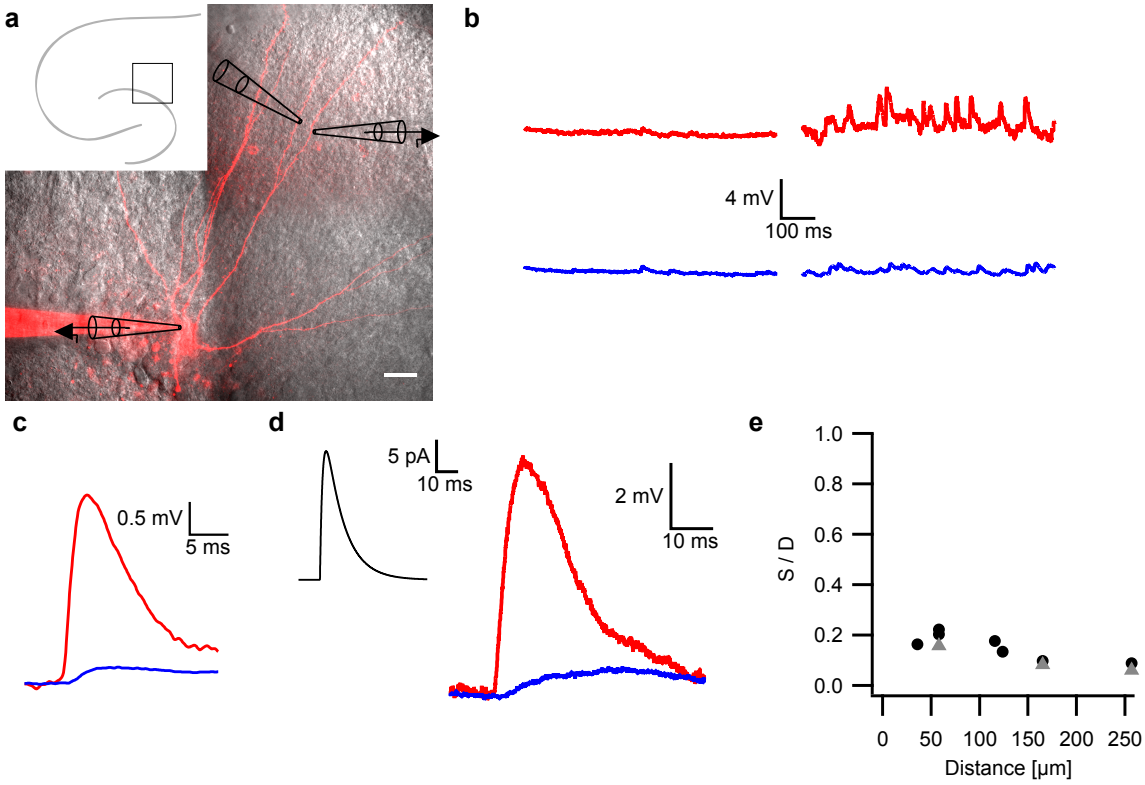

Figure 3.1.: Dendritic attenuation of EPSPs. **a**, Overlay of two-photon fluorescence and IR-SCG images of a granule cell. The locations of the somatic and dendritic patch pipettes and dendritic sucrose puff pipette are indicated (scalebar 20 µm). **b**, Spontaneous (left) and sucrose-evoked (right) EPSPs in the dendritic (red) and somatic recordings (blue). **c**, Average sucrose-evoked EPSP in dendritic (red) and somatic recording (blue). **d**, Attenuation of EPSPs elicited by dendritic current injection (red: dendritic recording, distance 165 µm from the soma, blue: somatic recording, black: current injection). **e**, Amplitude attenuation of dendritically injected (black circles) or sucrose evoked EPSPs (gray triangles) versus distance from the soma quantified as somatic EPSP amplitude divided by dendritic EPSP amplitude (S/D).

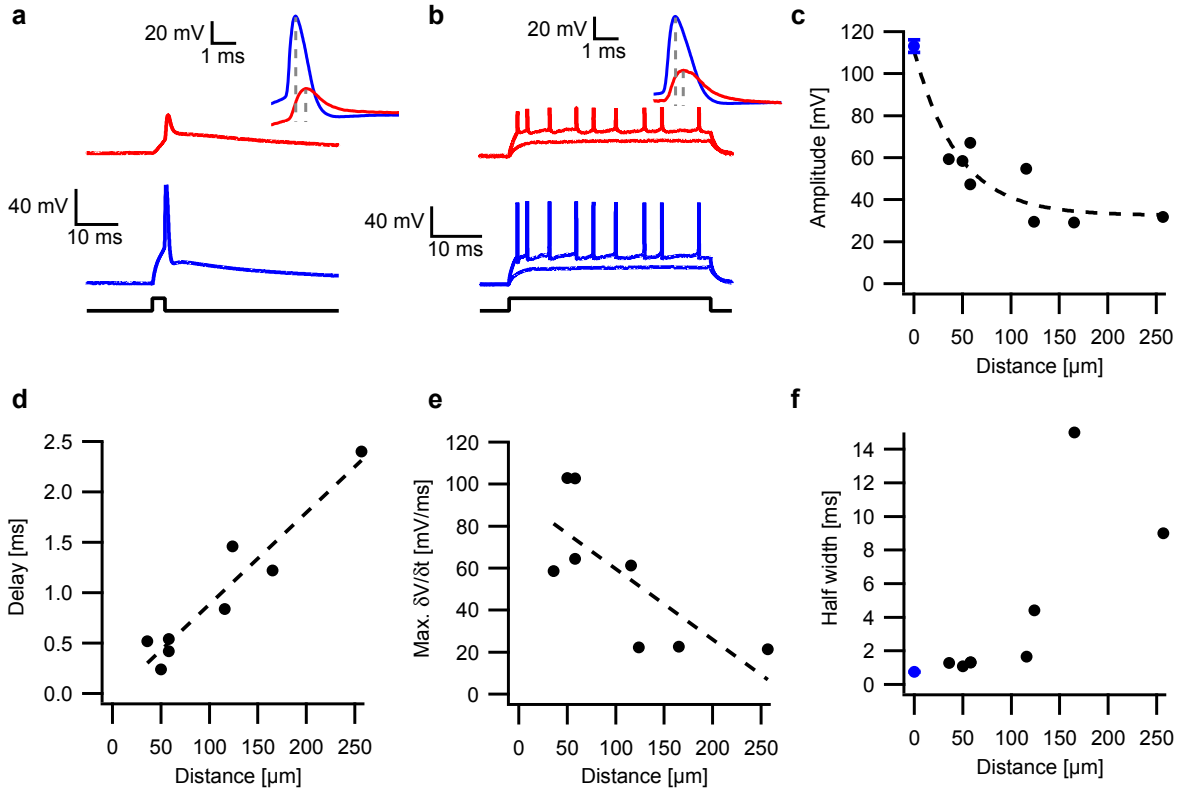

Figure 3.2.: Dendritic attenuation of backpropagating action potentials. **a**, **b**, Single action potential (**a**) or train of action potentials (**b**) evoked by somatic current injection (black), recorded at the soma (blue) and at the dendrite (red, 58 µm from the soma). Inset: higher magnification with peak delay marked by dashed lines. **c**, Action potential amplitudes from baseline in somatic (blue) and dendritic recordings (black) versus distance from soma (n=8). Dashed line: exponential fit with τ=45.4 µm. **d**, Action potential peak delay versus distance from soma. Dashed line: linear fit with slope=0.91±0.12 ms/100 µm. **e**, Peak of the first derivate of the action potential waveform versus distance of the dendritic recording site from the soma. Linear fit is shown as dashed line with slope=-34±12 mV/(ms·100 µm). **f**, Action potential half-width versus distance of dendritic recording site from soma. Somatic half width is shown in blue for comparison. As the action potential peak blends into the action potential afterdepolarization the half width increases drastically at great distances.

insets for magnifications, n=8). The bAP amplitudes decreased strongly towards more distal dendritic recording sites (fig. 3.2c), while the delay, the peak of the first derivative, and the half-width of the action potentials increased (bAP peak delay in fig. 3.2d, changes in bAP $\delta V/\delta t$ and half-width in e and f, respectively). In agreement with the marked decrement of bAP amplitudes, the Ca^{2+} transients associated with bAPs also decreased substantially (fig. 3.3a–c). Intriguingly, the amplitudes of bAPs in a train of action potentials evoked by long somatic current injections stayed constant (example in fig. 3.2b). This observation is in marked contrast to pyramidal neurons, where slow recovery from inactivation of dendritic voltage-gated sodium channels reduces bAP amplitudes in a train (Spruston et al., 1995; Stuart et al., 1997). To assess the possible role of dendritic potassium and sodium conductances, we imaged Ca^{2+} transients associated with bAPs before and after puff application of either the A-type potassium channel blocker 4-AP or the sodium channel blocker TTX to the dendrite between the soma and the imaging site (fig. 3.3d, e). Although the data show a trend towards increased Ca^{2+} transients after A-type potassium channel blockade and towards decreased transients after sodium channel blockage, these changes are not significant (fig. 3.3f). In contrast to our findings in granule cells, distal bAP associated Ca^{2+} transients dramatically increase after application of high concentrations of 4-AP in layer V pyramidal neuron basal dendrites (Kampa and Stuart, 2006). In addition, in these neurons proximal Ca^{2+} transients decrease significantly after puff application of TTX.

3.1.3. Passive dendritic model reproduces strong bidirectional attenuation

We constructed a realistic computational model of granule cell dendritic integration using three different morphologies derived from Schmidt-Hieber et al. (2007) (see materials and methods, section 2.5). In implementations of these morphologies lacking dendritic voltage-gated conductances, we observed a similar attenuation of EPSPs as in the experiments (fig. 3.4a). In particular, the model also exhibited a very limited variance of EPSP attenuation at dendritic distances of 100–250 µm between stimulation site and soma. This phenomenon appeared to be due to a steep increase in the high frequency transfer impedances (see introduction, section 1.1.1) at proximal locations (less than 100 µm from the soma, fig. 3.4c, steady-state transfer impedances in d). Action potential backpropagation was also well replicated in this

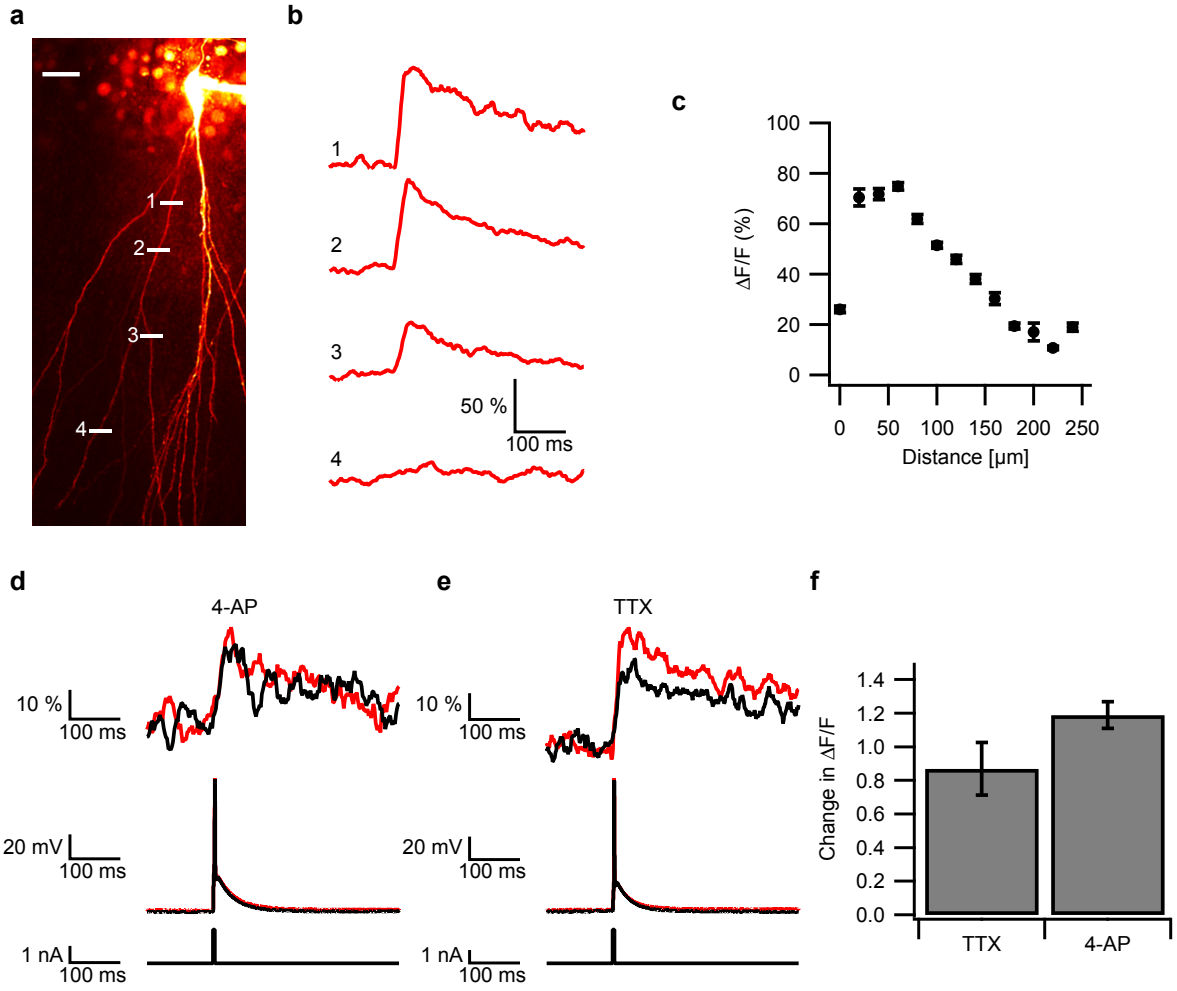

Figure 3.3.: Calcium transients associated with backpropagating action potentials. **a**, Two-photon image montage of a granule cell (scalebar 20 µm). **b**, OGB-1 fluorescence traces of bAP induced Ca^{2+} transients from the linescans marked by white lines in a. **c**, Peak fluorescence of bAP induced Ca^{2+} transients versus distance (binned every 20 µm, n=14 cells and 120 linescans). **d**, **e**, Example OGB-1 fluorescence traces of bAP induced Ca^{2+} transients before (black) and after (red) dendritic puff application of either 4-AP (**d**, 5 mM, average distance from soma 190 µm (131–308 µm), left) or TTX (**e**, 1 µM, average distance from soma 108 µm (86–128 µm), right). **f**, Quantification of the change in peak fluorescence after application of 4-AP (n=11) or TTX (n=4). Differences are not significant (Wilcoxon signed rank test of peak fluorescence before and after drug application, p=0.08 and p=0.25, respectively).

computational model with passive dendrites (fig. 3.4b, attenuation as function of distance from the soma for four different granule cell morphologies).

In addition, the influence of transient sodium currents and A-type potassium currents was studied in the computational model (fig. 3.5). Increasing dendritic sodium conductance to $5\,\mathrm{mS/cm^2}$ or more yielded an active action potential backpropagation which was incompatible with the experimental results (fig. 3.5a, Kolmogorov-Smirnov test, experimental attenuation versus fit to attenuation in the model with passive dendrites, p=0.23; versus the model with $1\,\mathrm{mS/cm^2}$ sodium conductance density, p=0.058; versus the model with $5\,\mathrm{mS/cm^2}$, $p<1 \cdot 10^{-6}$; versus the model with $10\,\mathrm{mS/cm^2}$, $p<1 \cdot 10^{-6}$). A combination of sodium ($10\,\mathrm{mS/cm^2}$) and potassium conductances ($60\,\mathrm{mS/cm^2}$) also leads to a better action potential backpropagation than is observed in the experiments (fig. 3.5b, p=0.00002). Incorporating only A-type potassium channels in the dendrites increased attenuation of bAPs only slightly compared to the purely passive case (fig. 3.5b, $30\,\mathrm{mS/cm^2}$, p=0.09, $60\,\mathrm{mS/cm^2}$, p=0.07).

These combined experimental and modeling results indicate that granule cell dendrites mediate strong and uniform attenuation of EPSPs arising throughout the termination zone of the perforant path. In addition, the attenuation of EPSPs and the attenuation of backpropagating action potentials can be explained with passive dendrites alone.

3.1.4. Attenuation is highly frequency-dependent

While action potentials and EPSPs attenuate strongly, the steady-state voltage attenuation measured by injection of prolonged current steps through either the dendritic or somatic recording electrode was much less pronounced (attenuation from the dendritic site to the soma: range 94% for the most distal recording site to 52% near the soma, fig. 3.6, n=9), indicating that attenuation is considerably stronger for fast voltage signals as is expected from theoretical considerations (see introduction, section 1.1.1, equation 1.7, and fig. 3.4c, d). We corroborated this with a more rigorous analysis of the frequency-dependent dendritic properties using ZAP functions (see materials and methods, section 2.2.3 and equation 2.1) that were injected through either the dendritic or somatic electrodes (see fig. 3.7a). We then estimated the voltage transfer by calculating the ratio of the Fourier transforms of the somatic and dendritic voltage traces (fig. 3.7b). These data confirm a strong frequency-dependence of voltage attenuation, with a significantly stronger

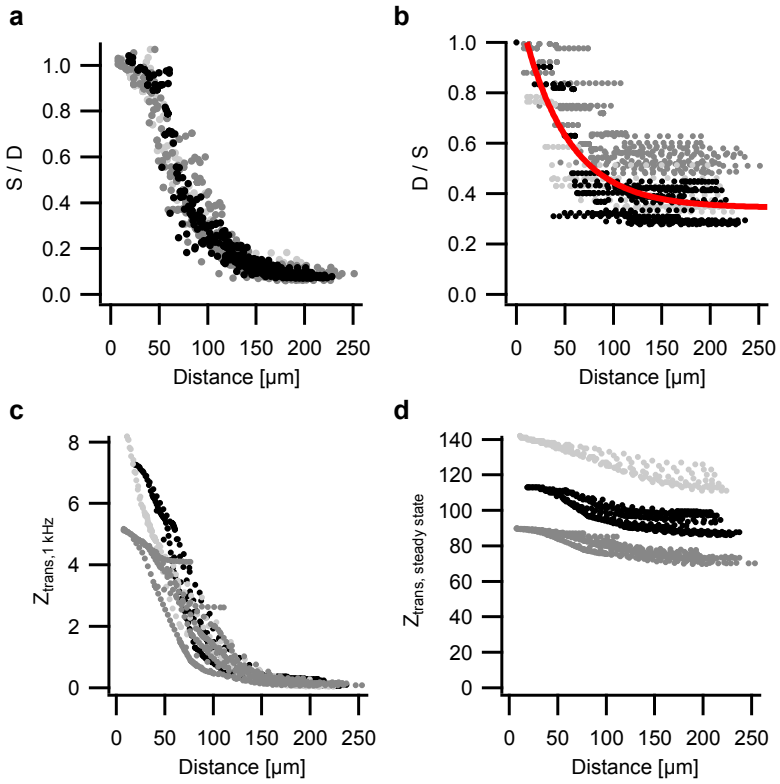

Figure 3.4.: Dendritic propagation of signals in a computational model. **a**, EPSP amplitude attenuation in a computational model of three granule cell morphologies versus distance from the soma. Different cells are represented by different gray shades. Every point represents one measurement in a dendritic subsegment. Attenuation is quantified as somatic EPSP amplitude divided by dendritic EPSP amplitude (S/D). **b**, bAP amplitude attenuation in the same model. Attenuation is quantified as dendritic AP amplitude divided by somatic AP amplitude (D/S). Red line is an exponential fit to the data (compare fig. 3.5) **c**, Transfer impedance at 1 kHz for three different granule cell morphologies (shown in different gray shades). **d**, Transfer impedance at 0 Hz (steady state) for the same granule cell morphologies as in c. The transfer impedance for 1 kHz shows a sharp decrease in the first 100 µm, in contrast to the steady-state transfer impedance.

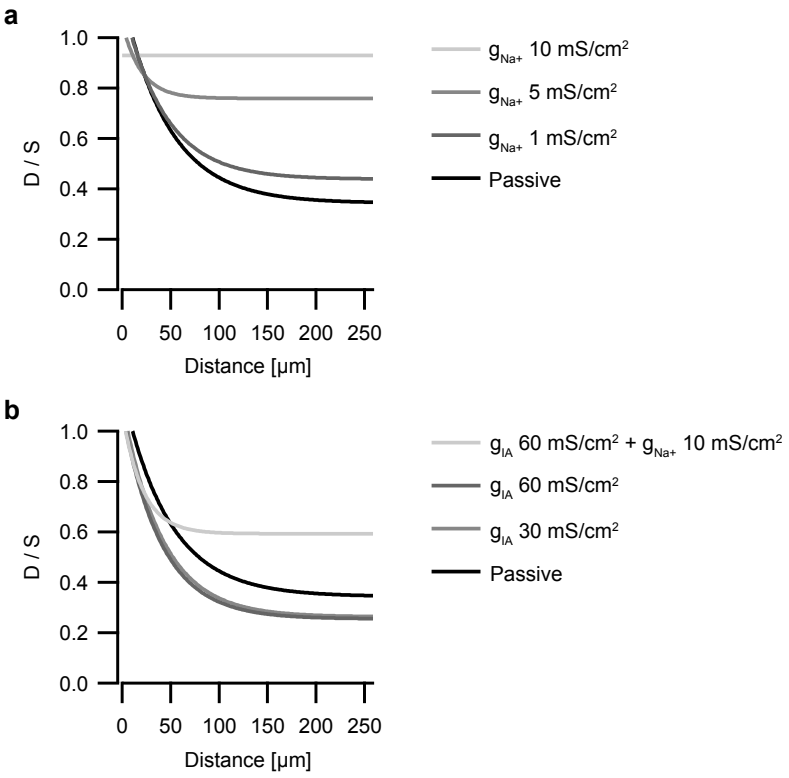

Figure 3.5.: Backpropagating action potentials in a computational model with different dendritic current densities. **a**, **b**, Action potential amplitude ratios versus distance from the soma in a model of granule cells with either a passive dendritic tree or different homogeneous densities of Na^+ channels (**a**) or A-type K^+ channels (**b**) as indicated. Attenuation is quantified as dendritic AP amplitude divided by somatic AP amplitude (D/S). Lines are exponential fits to datapoints of three model granule cells as shown in fig. 3.4b

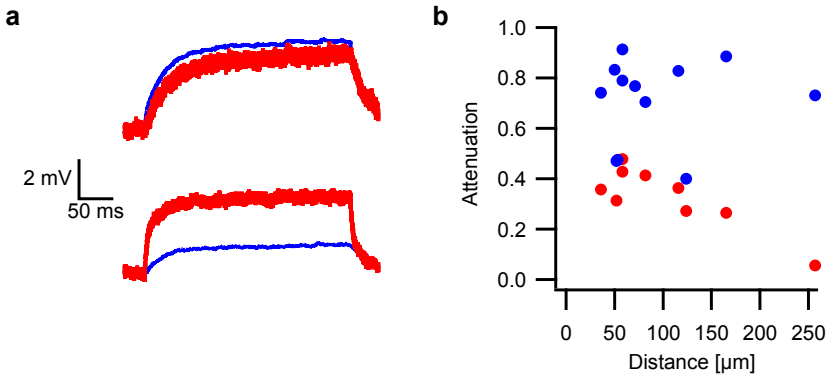

Figure 3.6.: Steady-state voltage attenuation in granule cell dendrites. **a**, Example traces of voltage deflections upon long current injections into the soma (upper traces) or into the dendrite (lower traces). Blue: somatic recording, red: dendritic recording (distance from soma 116 µm). **b**, Steady-state attenuation versus distance of dendritic recording site. Blue: attenuation from soma to dendrite (n=11), red: attenuation from dendrite to soma (n=9).

attenuation at higher frequencies (paired t-test of steady-state attenuation versus attenuation at 25 Hz, towards the soma, p=0.002, towards the dendrite, p=0.013). The frequency-dependent voltage transfer properties assessed with ZAP functions were well replicated in the computational model (fig. 3.7c). We did not observe resonance behavior in either somatic or dendritic compartments, in contrast to CA1 pyramidal neurons, where both somatic and dendritic compartments show active resonance mechanisms (Narayanan and Johnston, 2008; Hu et al., 2002).

3.1.5. Enlarged integration time window due to passive properties

The frequency-dependent attenuation seen in granule cell dendrites suggested that the voltage transfer to the soma is also dependent on the temporal features of the input. We therefore injected dendritic compound mock EPSCs consisting of 5 individual EPSCs separated by a variable time interval Δt ranging from 0.1 ms to 100 ms (see material and methods section 2.2, fig. 3.8a, b). All compound EPSPs were strongly attenuated. However, calculating the voltage attenuation (S/D) for the different degrees of synchrony revealed a nonlinear relationship, with the least attenuation observed at $\Delta t \approx 10$ ms (fig. 3.8c, n=8). When the peak voltages attained during compound EPSPs (normalized to the most synchronous $\Delta t = 0.1$ ms compound EPSP) at the dendritic and somatic recording sites were plotted against Δt, both declined with increasing Δt. Nevertheless, the normalized somatic EPSP

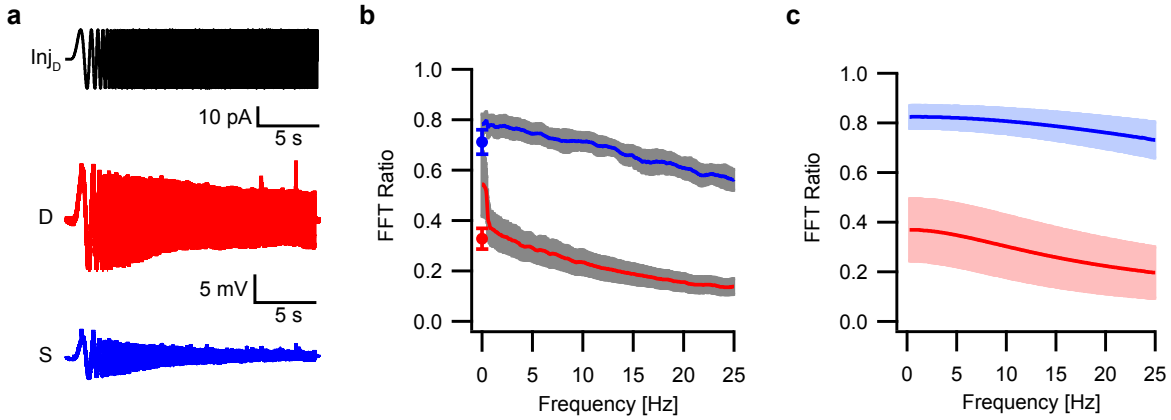

Figure 3.7.: Frequency-dependent voltage attenuation in granule cell dendrites. **a**, Example traces of voltage responses at the dendritic (red, distance from soma 58 µm) and somatic (blue) recording site to a dendritic sinusoidal current injection with increasing frequency (black, ZAP protocol). **b**, Ratio of the Fourier transforms of the somatic and dendritic voltage traces for somatic (blue) and dendritic current injections (red) versus frequency (n=8, standard deviation indicated in gray). Average steady-state attenuations determined by long dendritic current injections (n=9) are shown as filled circles at 0 Hz (blue: towards the dendrite, red: towards the soma). **c**, Ratio of the Fourier transforms of the somatic and dendritic voltage traces for somatic (blue) and dendritic current injections (red) versus frequency in a computational model (average of 34 injections into different sections of one model cell, more distal than 85 µm from the soma, standard deviation is indicated in lighter colors).

is stable over a larger range of Δt, indicating that the propagation of EPSPs from the dendritic sites to the soma increases the integration time window for EPSP summation (fig. 3.8d). We observed very similar properties in the computational model with application of identical compound mock EPSCs (virtual recording sites indicated in fig. 3.9a, example traces in fig. 3.9b, analysis of the three model granule cells in fig. 3.9c, d). This property of granule cell dendrites arises because the fast rising phases of either compound EPSPs with a high degree of synchrony ($\Delta t \approx 0\,\text{ms}$) or those of individual EPSPs with very low synchrony ($\Delta t > 50\,\text{ms}$) are particularly strongly filtered during propagation to the soma. In contrast, the overall rising phases of compound EPSPs with intermediate synchrony are slower, and are therefore attenuated less.

These results establish that the frequency-dependent properties of thin granule cell dendrites render EPSP summation less sensitive to input synchrony by increasing the somatic time window for temporal integration of synaptic input.

3.2. Integration of synchronous input in dentate granule cells

3.2.1. Clustered input is integrated linearly with a gain

Whereas the results so far shed light on the voltage transfer properties of granule cell dendrites, they do not allow insights into the processing of spatiotemporal input patterns mediated by the release of glutamate. We therefore used multisite two-photon uncaging of MNI-caged-glutamate to explore how granule cell dendrites integrate synchronous synaptic inputs. We measured the summation of uncaging-evoked excitatory postsynaptic potentials (gluEPSPs, amplitudes and rise times of gluEPSPs are independent of distance of the uncaging sites, fig. 3.10) evoked by stimulation of up to 13 spines on individual dendritic branches (fig. 3.11). Stimulating increasing numbers of inputs with a high degree of synchrony resulted in a monotonic increase in the magnitude of the resulting gluEPSPs (fig. 3.11b, c). We examined this summation of individual gluEPSPs further by comparing the measured gluEPSPs to the expected magnitude of EPSPs derived as the arithmetic sum of the individual single spine gluEPSPs (fig. 3.11c). Dendritic branches in granule cells exhibited a linear summation of gluEPSPs with gain in most branches (individual example in

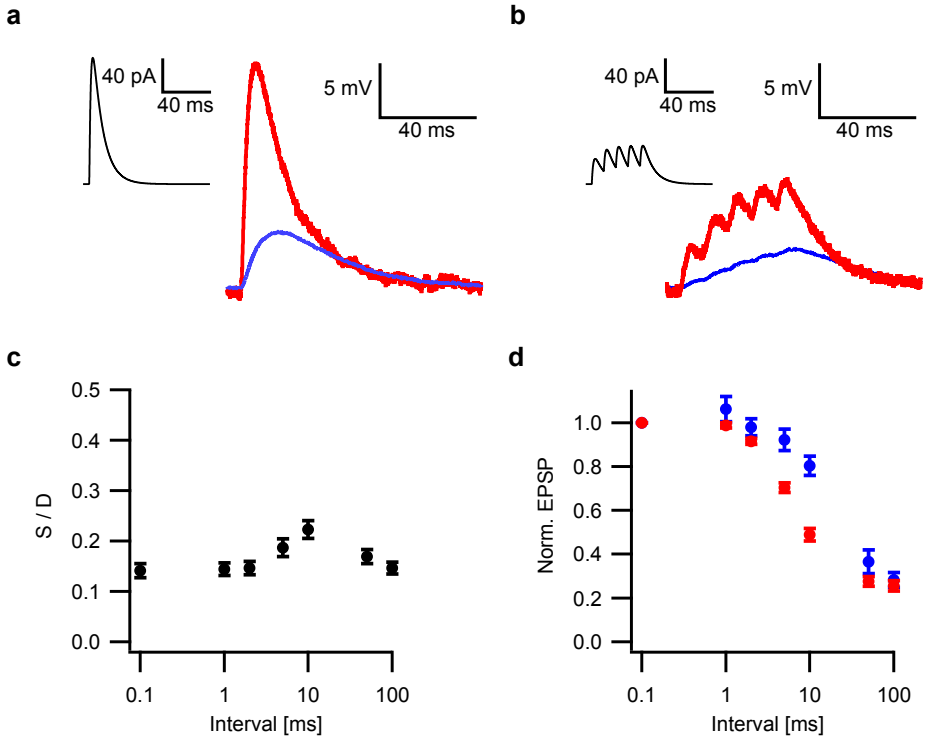

Figure 3.8.: Somatic and dendritic integration time windows. **a**, **b**, Dendritic current injection waveforms of five mock EPSCs with intervals of 0.1 ms (**a**, inset, black trace) and 10 ms (**b**, inset, black trace). Red: dendritic voltage responses, blue: somatic voltage responses to the mock EPSC injections. **c**, Average attenuation of the compound EPSP versus the intervals between the five injected mock EPSCs. **d**, Compound EPSP peak voltages normalized to the peak voltage of the compound EPSP with highest synchrony (0.1 ms interval) versus the mock EPSC intervals. Red: dendritic recordings, blue: somatic recordings.

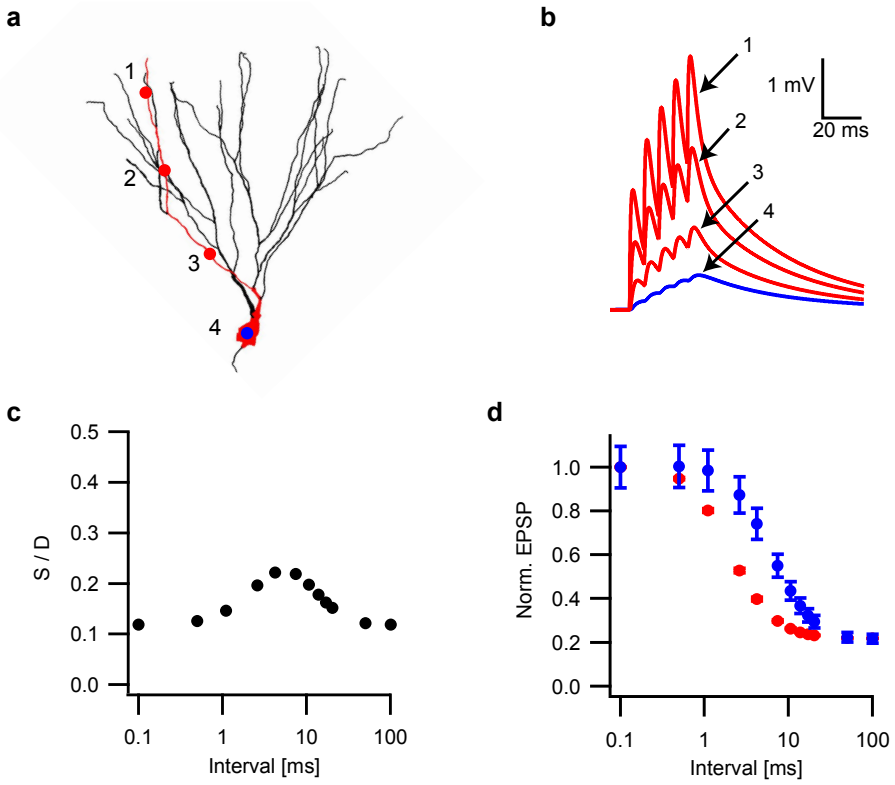

Figure 3.9.: Integration time window in a computation model. **a**, Schematic diagram of a model granule cell with dendritic (red) and somatic (blue) recording sites. **b**, Voltage traces for 5 synaptic current injections with an interval of 7.4 ms measured at the sites shown in a. **c**, Attenuation of the compound EPSP in the model versus the intervals of synaptic activation. **d**, Compound EPSP peak voltages obtained in the model, normalized to the peak voltage of the compound EPSP with highest synchrony (0.1 ms) versus the interval of synaptic activation. Red: recording at site of the synapses, blue: somatic recording.

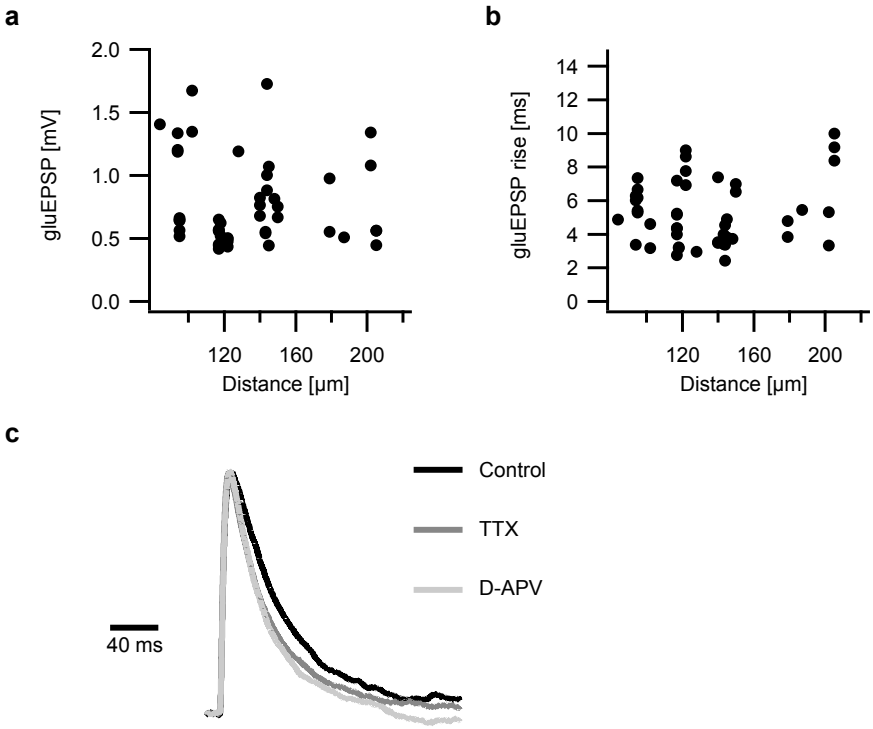

Figure 3.10.: Properties of uncaging-evoked EPSPs. **a**, Average single spine gluEPSP amplitudes versus distance of uncaging site from soma (n=55). No correlation with distance (Pearson's r=-0.13, p=0.33). **b**, Average gluEPSP rise times versus distance. No correlation with distance (Pearson's r=0.07, p=0.61). **c**, Average normalized single spine gluEPSPs under control conditions (τ_{decay}=40.8 ms, n=592 synapses, black), TTX (1 µM, τ_{decay}=33.7 ms, n=299 synapses, dark gray), D-APV (50 µM, τ_{decay}=34.3 ms, n=170 synapses, light gray. The decay time constants show significant differences (Kruskal-Wallis test, p=0.049), with the decay time constant under control conditions different from all other groups (TTX and D-APV, modified Dunn-Hollander-Wolfe test).

fig. 3.11d). The average gain obtained by linear fitting under control conditions was 1.38±0.06 (n=47 branches, fig. 3.11e, red line). That the relationship of measured versus expected gluEPSPs was linear over a wide range of input strengths was surprising, since it was expected that the loss of local driving force at the dendritic stimulation site would lead to a saturation of the local EPSP size with increasing stimulation strength (for estimation of the magnitude of this effect see appendix A.3). Hence, these data suggested the presence of voltage-dependent boosting mechanisms that compensate the loss of driving force and additionally causes a linear gain. Because synaptically elicited perforant path EPSCs had a substantial NMDA receptor mediated component (fig. 2.2, NMDA/AMPA peak current ratio 1.08±0.12, n=9, see also Keller et al., 1991), we explored how these receptors impact processing of synchronous input. In the presence of the NMDA receptor blocker D-APV (50 µM), the ratio of measured versus expected gluEPSPs declined when the number of synchronously stimulated spines was increased (fig. 3.11e, black squares, n=14 branches, see fig. 3.12a, b for representative experiment). This became apparent when plotting the deviation of the measured gluEPSPs from the line fitted to the control dataset in fig. 3.11e (Δ from control) for 2 to 13 synchronously stimulated spines (fig. 3.11f). The deviation from control for 13 synchronously stimulated spines was significant in the TTX (1 µM, see fig. 3.12c, d for representative experiment) and D-APV conditions (Dunnett test, Control versus D-APV: $p=7.6 \cdot 10^{-7}$, Control versus TTX: $p=5.4 \cdot 10^{-6}$, § in fig. 3.11g). TTX also significantly decreased the decay time constant of individual spine gluEPSPs (see fig. 3.10c), which could indicate a location of sodium channels on dendritic spines (Araya et al., 2007). Taken together, these data indicate that under normal conditions granule cell dendrites sum input linearly with gain, independently of the number of synchronously stimulated spines, due to NMDA receptor- and Na^+ channel-dependent boosting.

3.2.2. Gain is due to NMDA receptors, sodium channels, and propagation working together

We then explored this effect in the computational model. Up to 13 colocalized synapses on the dendritic tree of a model granule cell were stimulated, with synapses exhibiting the experimentally determined NMDA/AMPA ratio of 1.08, while recording the membrane potentials at the dendritic stimulation site and the soma. First, an individual synapse was stimulated alone (•, fig. 3.13a, upper trace), then 12

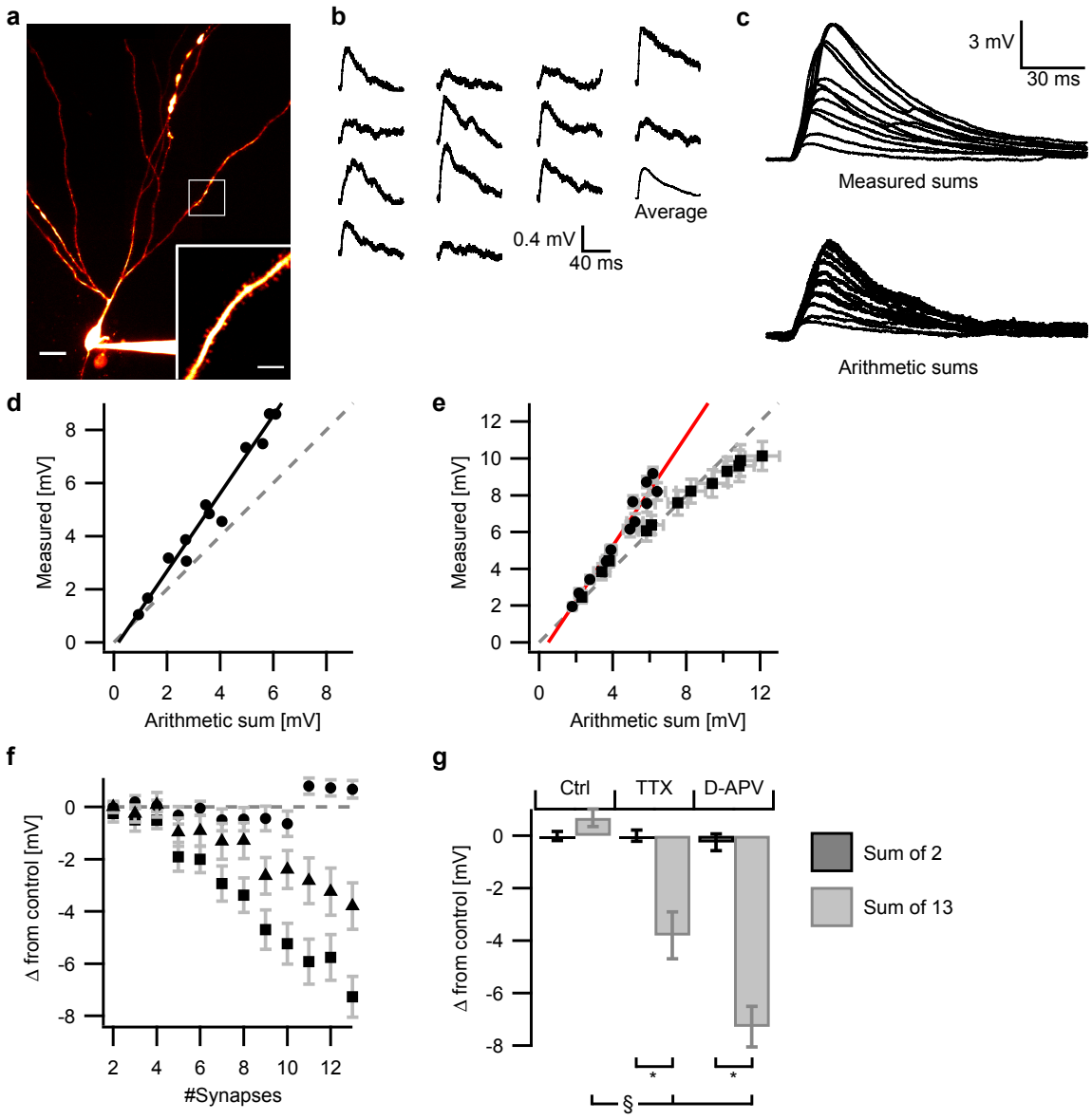
a
b
c
3 mV
30 ms
Measured sums
Average
0.4 mV
40 ms
Arithmetic sums
d
e
Measured [mV]
Arithmetic sum [mV]
f
g
Δ from control [mV]
#Synapses
Ctrl
TTX
D-APV
Sum of 2
Sum of 13
*
§

Figure 3.11.

Figure 3.11.: Integration of synchronous input probed by two-photon glutamate uncaging. **a**, Two-photon image of a granule cell (scalebar 20 µm). Inset shows a higher magnification, uncaging spots are marked (scalebar 5 µm). **b**, Uncaging-evoked EPSPs from 13 single synapses and the average gluEPSP (lower right). **c**, Top: gluEPSPs evoked by uncaging synchronously at increasing numbers of spines (2–13). Bottom: EPSPs calculated as arithmetic sums of an increasing number of single spine gluEPSPs from b. **d**, Plot of the magnitude of measured gluEPSPs (example data from c) versus the equivalent arithmetic sum of gluEPSPs. Red line is a linear fit to the data (slope 1.44). A slope of 1 is indicated by the dashed gray line. **e**, Population data of measured sum gluEPSP peaks versus peaks of calculated arithmetic sum EPSPs (binned for each number of activated synapses, control: circles, n=47, D-APV: squares, n=14). Red line is a fit to the population data (average slope 1.38±0.06). The dashed gray line indicates a slope of 1. **f**, Deviation of the measured sum gluEPSP from the fit to the control population data (control: circles, n=47, TTX: triangles, n=23, D-APV: squares, n=14). **g**, Deviation of the measured sum gluEPSPs of 2 and 13 synapses from the fit to the control population data (Wilcoxon-signed-rank test, 2 versus 13 synapses: TTX, $p<0.0001$, D-APV, $p=0.002$; Dunnett test, TTX and D-APV versus control for 13 synapses, $p<0.0001$).

further synapses ($\Sigma\circ$), and finally all thirteen synapses ($\Sigma \circ +\bullet$, fig. 3.13a, middle traces) in a comparable manner as during the uncaging experiments. We isolated the contribution of a single synapse to the sum EPSP ($EPSP_{\Delta\bullet}$, fig. 3.13a, lower traces) by subtracting the EPSPs caused by stimulation of 12 synapses ($EPSP_{\Sigma\circ}$) from that of 13 synapses ($EPSP_{\Sigma\circ+\bullet}$). If local boosting at the dendritic site compensates the loss of driving force completely, then $EPSP_{\Delta\bullet}$ must be equal in magnitude to $EPSP_{\bullet}$. This was the case for control conditions with synapses incorporating both AMPA and NMDA receptors (fig. 3.13a, lower traces), but not for synapses containing only AMPA receptors ($EPSP_{\Delta\bullet}$ smaller than $EPSP_{\bullet}$, fig. 3.13b). These modeling data are consistent with the physiological data in fig. 3.11e, and indicate that the loss of local driving force in granule cell dendrites can be compensated by voltage-dependent boosting. Fig. 3.13c, d depicts the corresponding voltage recordings from the model cell soma. At the soma, $EPSP_{\Delta\bullet}$ was considerably larger than the $EPSP_{\bullet}$ (fig. 3.13c), consistent with the gain we had seen in physiological (fig. 3.11d, e) and modeling (not shown) experiments. Since the stimulation of sum EPSPs is slightly asynchronous in this model (Δt of 1.1 ms between every individual stimulation, consistent with the experimental paradigm, leading to a total stimulus duration of 14.2 ms), propagation of these voltage transients benefits from the frequency-dependent transfer properties of granule cell dendrites described above (section 3.1.5, fig. 3.8).

In summary, the total linear gain seen in the somatic compartment is caused firstly

by a local, NMDA receptor-dependent boosting and a subsequent propagation effect that favors slightly asynchronous sum EPSPs over single spine EPSPs (fig. 3.13e). These properties cause granule cell integration to be relatively independent of input synchrony. This behavior is qualitatively different from CA1 pyramidal neurons, in which input synchrony profoundly influences dendritic integration (Losonczy and Magee, 2006). In particular, dendritic spikes can occur upon synchronous stimulation of >5 spines (see also introduction, section 1.1.2). Dendritic spikes consist of an initial fast, followed by a slower component, as described previously (Losonczy and Magee, 2006; Remy et al., 2009). We could never elicit dendritic spikes by synchronous uncaging in dentate granule cells (n=47 dendrites under control conditions), and only in a single case by strong direct dendritic current injections (1 of 8 recordings).

3.3. Integration of spatially distributed input

3.3.1. Input from daughter branches is summed linearly

In pyramidal neurons, individual dendritic branches can exhibit specific forms of integration that differ markedly between adjacent branches (Losonczy et al., 2008; Remy et al., 2009). To study how inputs on different dendritic subbranches interact in dentate granule cells, we selected four sets of 7 spines on two daughter branches emanating from the same parent dendrite (fig. 3.14a). Then, we stimulated sets of 7 spines to obtain the corresponding gluEPSPs (fig. 3.14b). We subsequently stimulated various combinations of 7-spine sets (A_1+B_1, A_2+B_2, B_1+A_2 and B_2+A_1, black traces in fig. 3.14b). We compared these measured compound gluEPSPs with the EPSPs calculated by arithmetic summation of the gluEPSPs derived from stimulation of the 7-spine sets (gray traces in fig. 3.14b). Determining the ratio of measured and calculated compound gluEPSPs to stimulation of 14 spines situated either on one or two different branches revealed that the spatial distribution of inputs does not affect integration in granule cells (fig. 3.14e, GC, n.s., Wilcoxon rank test).

Performing analogous experiments on CA1 dendrites (fig. 3.14c, d), dendritic spikes could be elicited by stimulation of a single 7-spine set on one individual branch (data not shown). In those cases in which all four 7-spine sets were subthreshold for a dendritic spike (examples in fig. 3.14d, upper traces), some combinations of 7-spine sets, nevertheless, triggered dendritic spikes (B_1+A_2 in fig. 3.14d), while

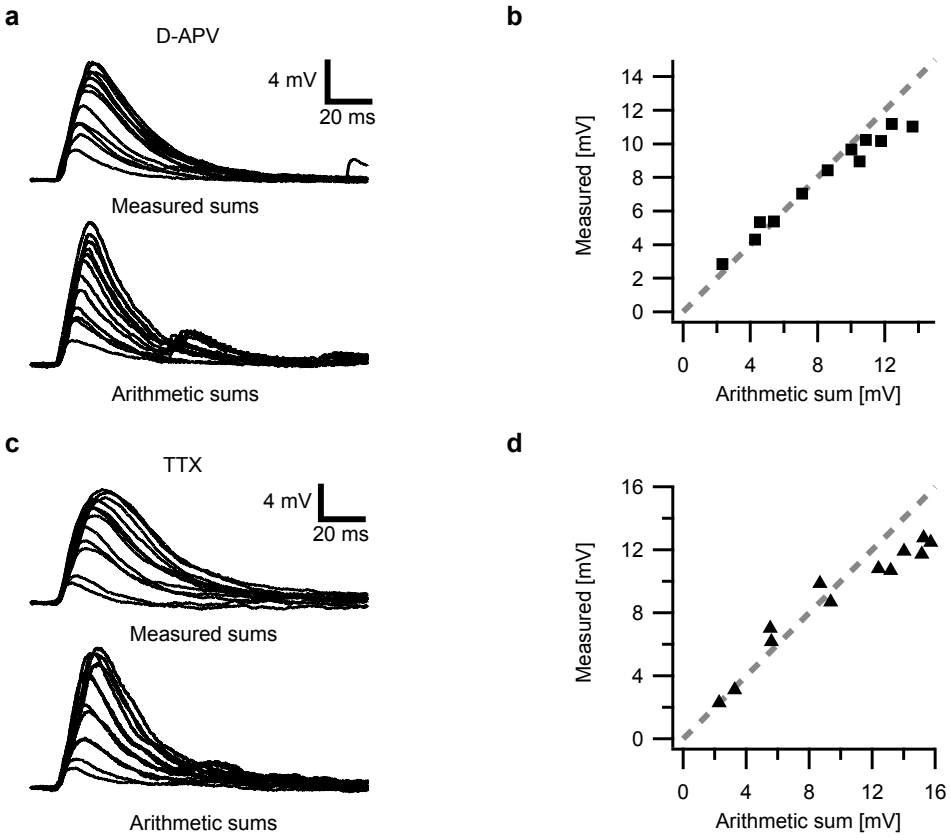

Figure 3.12.: Contribution of NMDA receptors and sodium channels to the integration of synchronous input. **a**, **b**, Representative example of synchronous stimulation of increasing numbers of input sites in the presence of D-APV (**a**, upper traces) and the corresponding arithmetic sum of the single spine EPSPs (lower traces). Comparison of measured versus expected sum EPSPs is shown in **b**. **c**, **d**, Equivalent experiment in the presence of TTX. Note that with D-APV the decay of the measured and calculated sum EPSPs is fast. With TTX, however, decay of calculated sums is fast (because single spine gluEPSP decay is fast, see fig. 3.10c), but decay of measured sums is slower due to unblock of NMDA receptors.

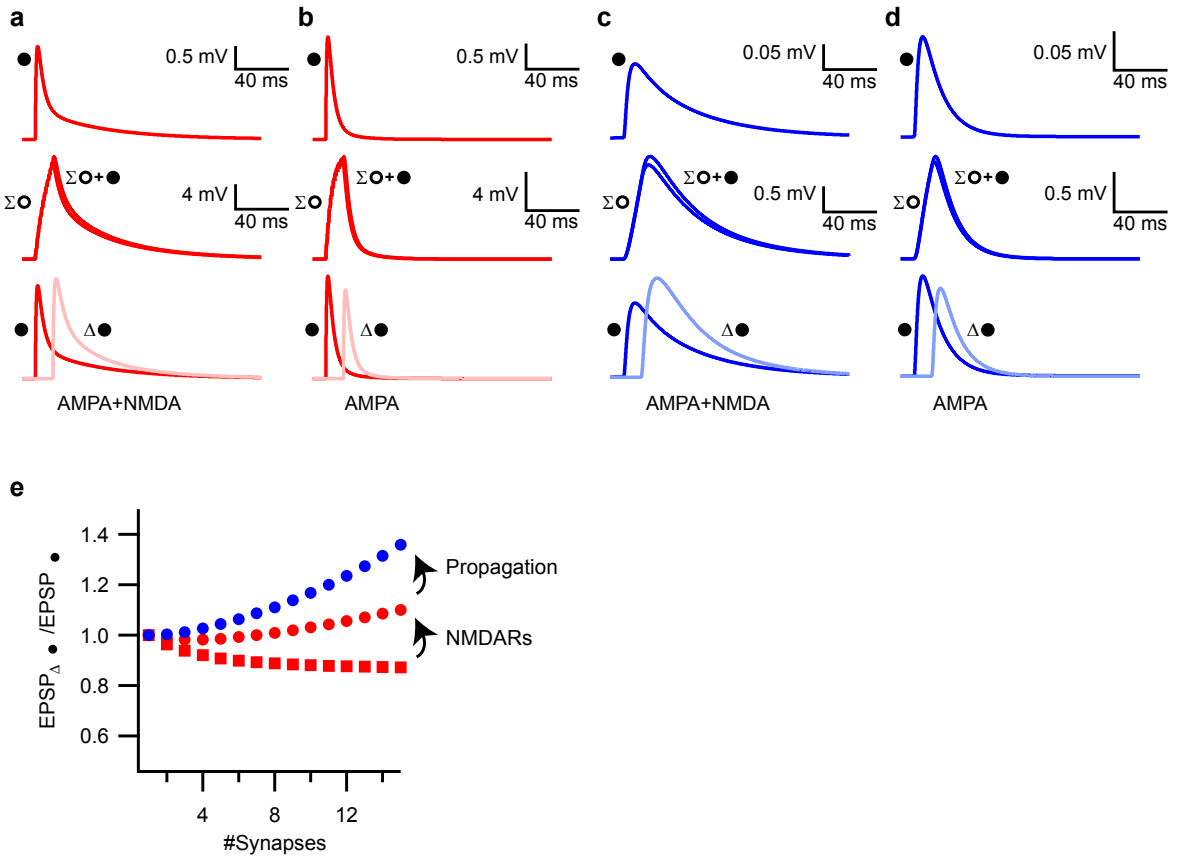

Figure 3.13.: Dendritic integration in a computation model of a granule cell. **a**, Top: example dendritic EPSP for activation of one synapse (●) in a computational model. Middle: dendritic sum EPSPs for 12 (Σ○) and 13 (Σ ○ +●) synapses activated with a 1.1 ms interval between each synapse. Bottom: dendritic single synapse EPSP calculated by subtraction of the sum EPSPs (Δ●) and the single synapse EPSP (●). **b**, Same as in a but with synapses incorporating just AMPA receptors. **c**, Same as in a but measured at the somatic compartment. **d**, Same as in a but measured at the somatic compartment and with synapses incorporating just AMPA receptors. **e**, Ratio (EPSP$_{●}$/EPSP$_{Δ●}$) of the amplitudes of a single synapse EPSP activated either alone or together with an increasing number of synapses. Red squares: dendritic EPSPs for synapses with just AMPA receptors. Red circles: dendritic EPSPs for synapses with AMPA and NMDA receptors. Blue: somatic EPSPs for synapses with AMPA and NMDA receptors.

other combinations did not. An explanation for this curious behavior could be that simultaneous uncaging on both daughter branches reduces the mutual current sink. Thus more current reaches the parent branch and can trigger a dendritic spike there. These data show that—in addition to the description of integration behavior for input sites on a single branch (Losonczy and Magee, 2006; Remy et al., 2009)—summation of input from two different branches in CA1 neurons can be either linear or supralinear by virtue of dendritic spikes (fig. 3.14e, PCs, dark gray versus light gray bars, d-spike branch weights significantly different from all non-spike groups, ANOVA and Newman-Keuls test).

Thus, CA1 neurons may be considered efficient synchrony detectors, as previously hypothesized (Ariav et al., 2003; Polsky et al., 2004), with local heterogeneities in the properties of dendritic branches contributing to the computational complexity of these neurons (Poirazi et al., 2003). In marked contrast, granule neurons exhibit a fundamentally different type of integration which is aimed at weighing the somatic impact of individual synapses independently of location or input synchrony.

3.3.2. Input from medial and lateral perforant path is summed linearly and independent of timing

The integration of inputs from two daughter branches was linear, but there could be interactions between more distant inputs from the two major afferent pathways to the dentate granule cells as proposed in a computational model of contextual gating (Hayman and Jeffery, 2008). We stimulated both medial and lateral perforant path inputs with different time intervals and compared the measured sums to the calculated sums derived from stimulation of each pathway alone. Again, we observed linear summation for all time intervals between the stimulations (fig. 3.15), ruling out an interaction between medial and lateral inputs to granule cell dendrites.

In summary, dentate gyrus granule cells perform a linear summation of inputs, on the level of individual branches, daughter branches, and on the level of the two major input pathways.

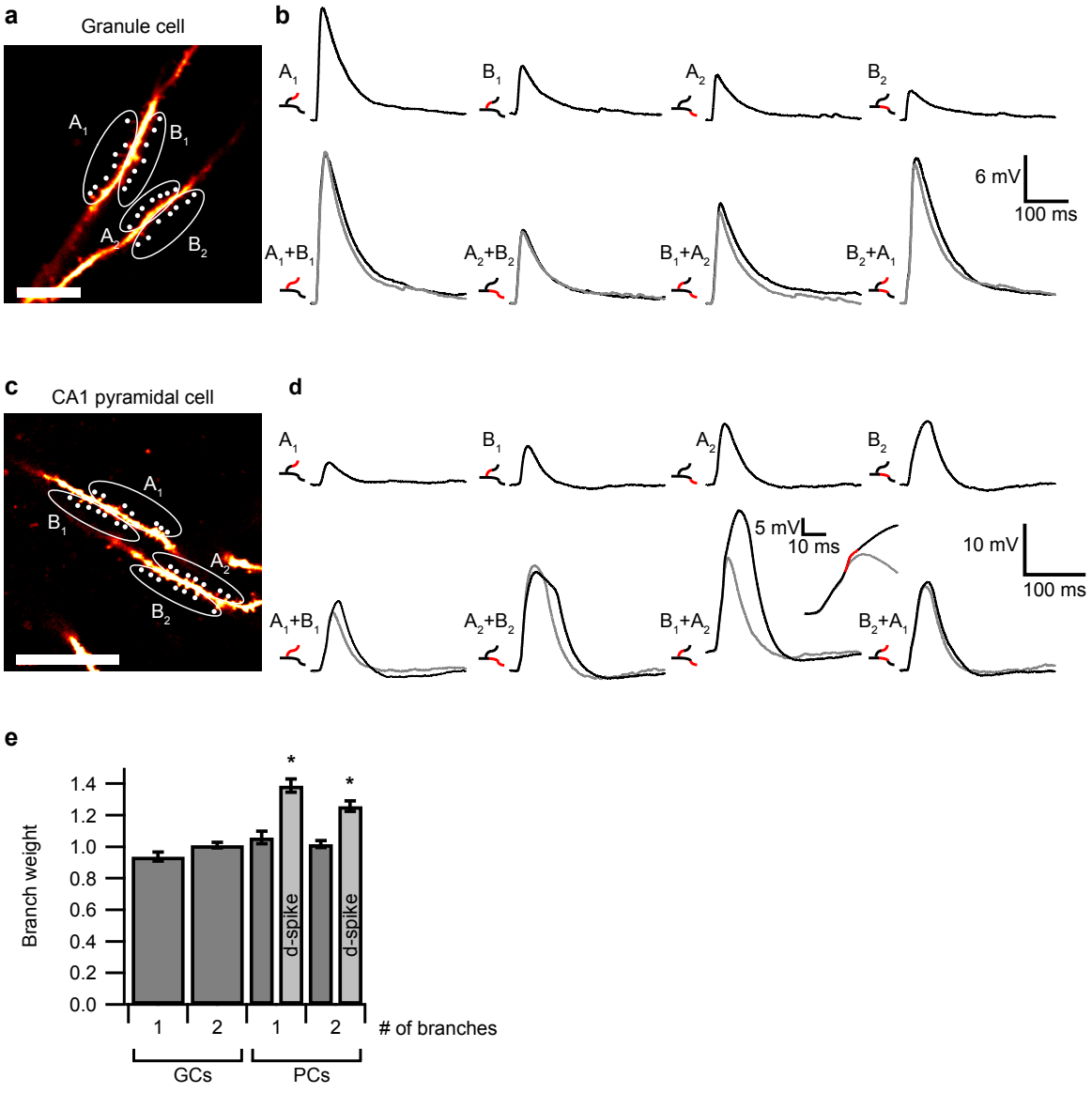
a
Granule cell
A1
B1
A2
B2
b
A1
B1
A2
B2
A1+B1
A2+B2
B1+A2
B2+A1
6 mV
100 ms
c
CA1 pyramidal cell
A1
B1
A2
B2
d
A1
B1
A2
B2
A1+B1
A2+B2
B1+A2
B2+A1
5 mV
10 ms
10 mV
100 ms
e
Branch weight
1.4
1.2
1.0
0.8
0.6
0.4
0.2
0.0
d-spike
d-spike
1
2
1
2
# of branches
GCs
PCs

Figure 3.14.

Figure 3.14.: Integration of input on two daughter branches. **a**, Two-photon image of two representative dentate granule cell daughter-branches originating from the same parent branch. Groups of seven uncaging spots are embraced by white ellipses and labeled A_1 and B_1 for one daughter branch and A_2 and B_2 for the other (scalebar 10 µm). **b**, Example traces of uncaging-evoked sum EPSPs of the four groups of seven spines, as indicated (A_1,B_1 and A_2,B_2, upper row). The lower row depicts traces obtained by synchronous uncaging at two groups of seven spines distributed on either a single or two different branches as indicated in red. Black: measured traces, gray: responses calculated by arithmetic summation of the responses from individual 7-spine sets. **c**, Two-photon image of a CA1 parent basal dendrite with two daughter dendrites (scalebar 20 µm). **d**, Identical experimental protocol for the CA1 pyramidal neuron as in b. Dendritic spikes occurred in CA1 neurons (larger magnification in the inset) but were never observed in granule cells. **e**, Summary data of the ratio of measured and calculated gluEPSPs (branch weight) on one (1) or two (2) branches in dentate granule cells (GC) and CA1 pyramidal cell basal dendrites (PC). In pyramidal cells, gluEPSPs featuring a dendritic spike are grouped separately (light gray). Branch weights of groups with spikes are significantly different from all non-spike groups (ANOVA and Newman-Keuls test, n=23 (GC), PC: n=40 (one branch), n=5 (one branch, spike), n=35 (two branches), n=7 (two branches, spike)).

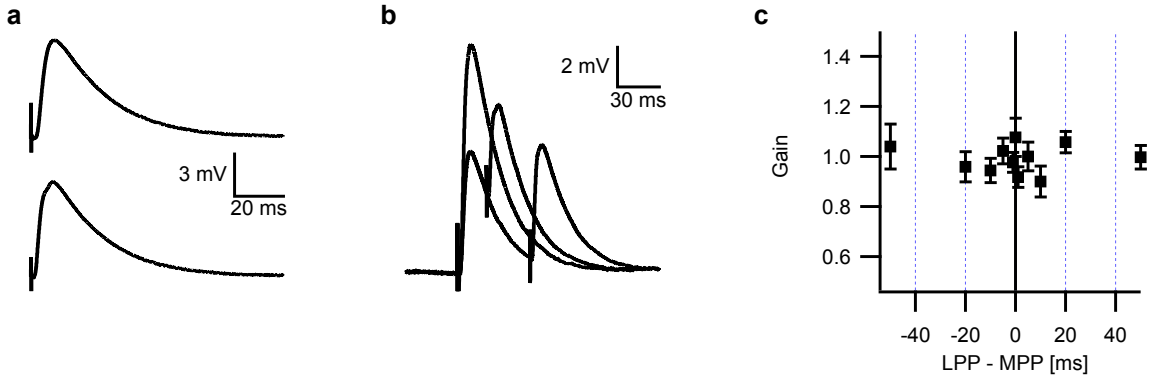

Figure 3.15.: Integration of simultaneous medial and lateral perforant path stimulation. **a**, Example EPSPs from stimulation in the outer (top) and medial molecular layer (bottom). **b**, Example sum EPSPs for stimulations in the outer and medial molecular layer with different time intervals (1 ms, 20 ms, and 50 ms). **c**, Summary diagram of the observed gain (ratio of measured sum EPSPs and arithmetic sum of single pathway EPSPs) versus the time interval between stimulations of both pathways.

3.4. Place field generation

3.4.1. Place fields can be generated by granule cells with passive dendrites

To assess how the integrative properties of granule cell dendrites might impact the function of granule cells in the processing of spatial information, we connected a granule cell in our model to afferent ensembles of grid cells (see e.g. Solstad et al., 2006 and materials and methods, section 2.5.1). Grid cell firing was simulated for an 'animal' on a zig-zag course through a 1 m x 1 m environment. Grid cells had properties as described (maximum firing rates of 15–25 Hz and grid sizes of 0.28–0.73 m, see Moser and Moser, 2008, representative firing maps of three grid cells in fig. 3.16a, leftmost side). Grid cells were synaptically connected to the dendrites of a granule cell (synapses indicated in fig. 3.16a, rightmost side). During the course of the simulation, granule cell somatic and dendritic membrane potentials were recorded (fig. 3.16b, blue and red indicate somatic and dendritic recordings, respectively), and the action potential firing converted to a firing map (fig. 3.16c, locations at which the cell fired indicated by red crosses).

To assess the impact of dendritic voltage attenuation on the processing of grid cell input, we placed afferent synapses at varying points along the dendritic tree with proximal locations (little attenuation), intermediate and distal locations (stronger attenuation, see red, black and green symbols in fig. 3.16d), and then systematically increased the number of grid cells (fig. 3.16e, examples of firing maps for 7, 15, and 35 presynaptic grid cells with differing input locations). The robustness of place field representations of the granule cells in this case is constrained on the one hand by the minimum number of grid cells that is required to cause granule cell firing. On the other hand, arbitrary increases in the size of the afferent grid cell ensemble will cause a prolonged granule cell depolarization with Na^+ channel inactivation and failure of action potential generation at the place field location.

3.4.2. Synaptic distance determines place field quality

Do granule cells in this model appropriately encode place information over the whole range in which they display firing behavior? To address this question, we estimated the quality of the firing map as the average in-place field firing rate

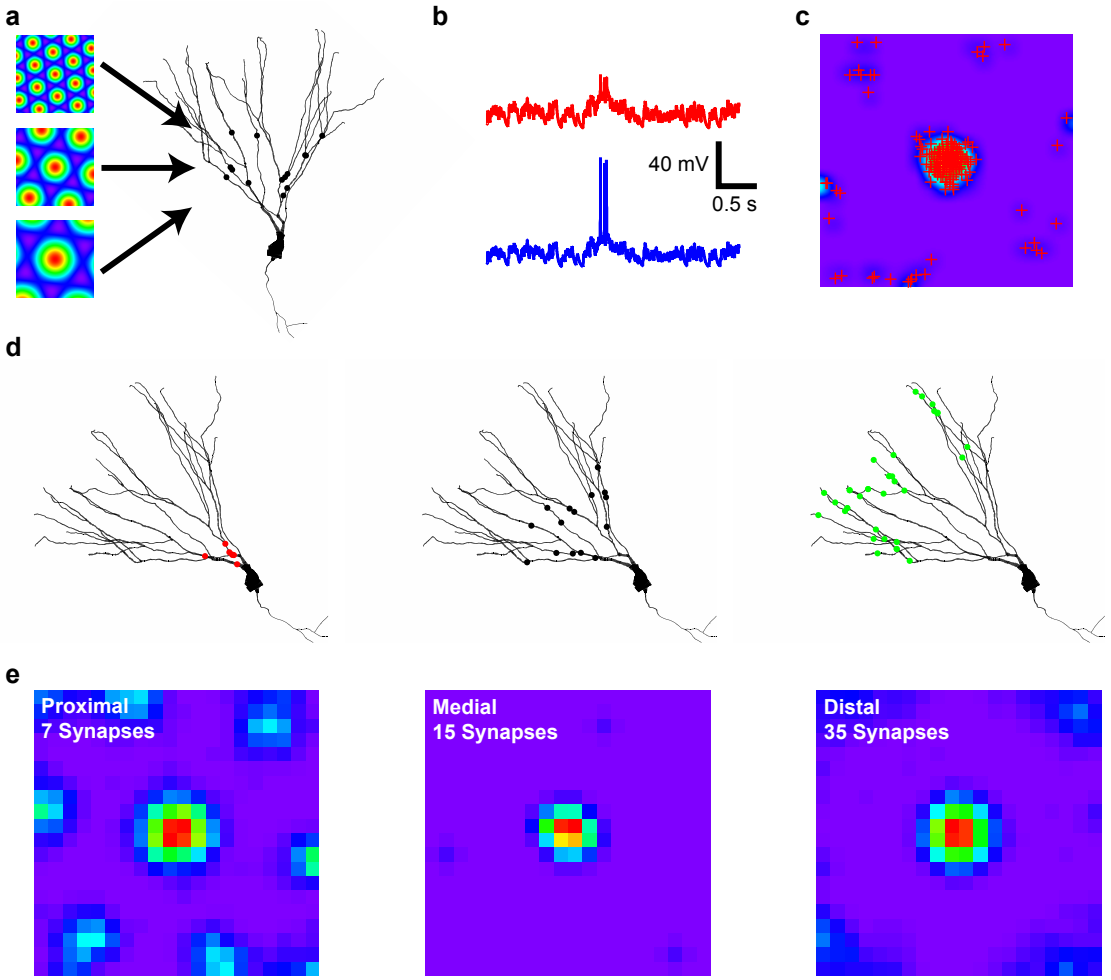

Figure 3.16.: Example place fields in a computational model. **a**, Schematic representation of the network model. A number of grid cells (representative firing maps of three grid cells on the left) are synaptically connected to the dendrites of a granule cell (synapses are marked with black dots). Somatic (blue pipette) and dendritic (red pipette) voltages were recorded during the course of the simulation. **b**, Representative section of somatic (blue, bottom) and dendritic (red, top) voltage during a simulation. **c**, Calculated firing map of the simulated granule cell with spike locations shown as red crosses. **d**, Examples of synapse distributions for three different kinds of simulations (proximal: red, medial: black, distal: green). **e**, Examples of firing maps for different numbers of presynaptic grid cells and distances.

divided by the average out-of-place field firing rate (contrast, fig. 3.17a). Place fields with a high contrast were obtained only over a relatively small range of presynaptic grid cell ensemble sizes, and only for medial and distal inputs (black and green in fig. 3.17b). This range is very close above the granule cells firing threshold (compare peak rate curves indicated by dashed lines in fig. 3.17b). In the firing range observed in-vivo within granule cell place fields (11.54±8.16 Hz, Leutgeb and Moser, 2007), the place field contrast was highest for the more distal inputs, whereas adequate place field generation was not obtained for proximal inputs (fig. 3.17c). These data indicate that attenuation is an important factor in sculpting the generation of place fields. In addition, there is an 'optimum attenuation' that gives rise to place fields with a quality that is robust over a range of grid cell ensemble sizes.

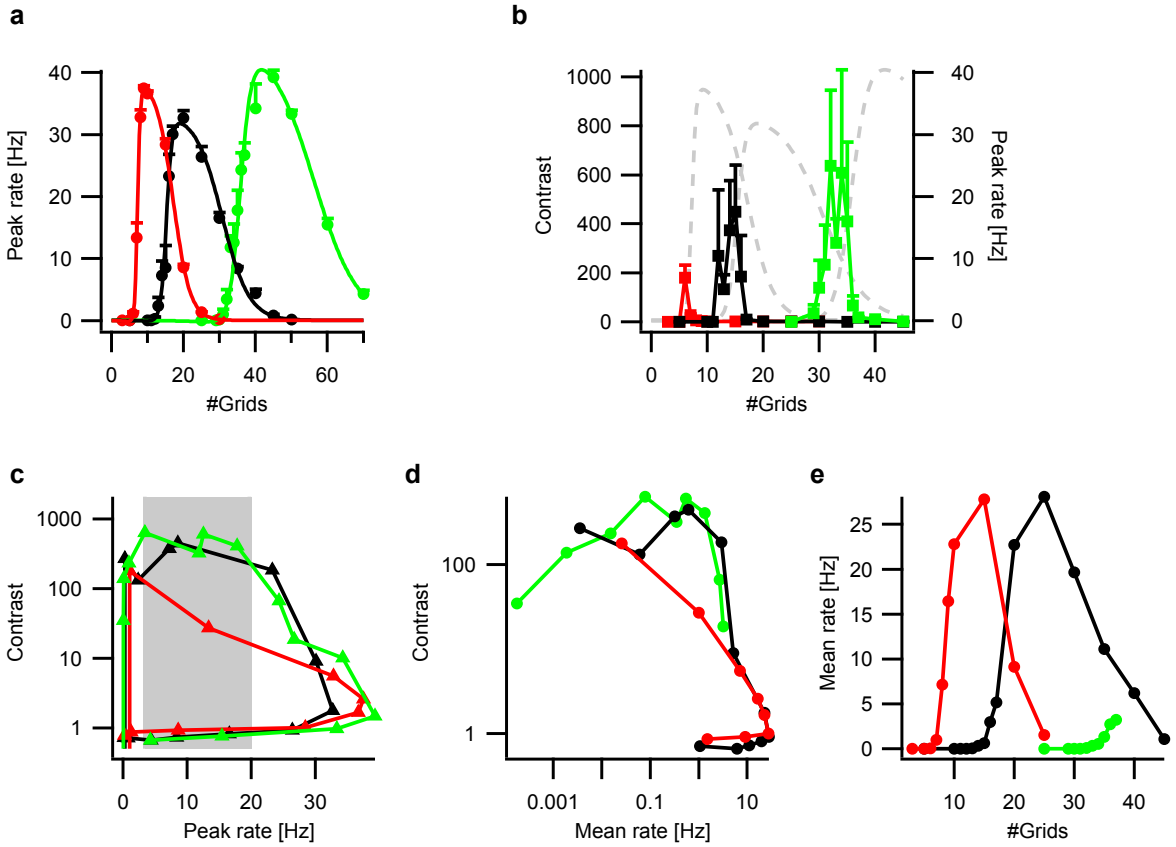

Figure 3.17.: Analysis of place fields in a computational network model. **a**, The peak firing rate in the place field versus the number of presynaptic grid cells for three different distance configurations (proximal: red, medial: black, distal: green). Colored lines are bi-sigmoidal fits to the data. Grid numbers for half maximal peak rate are 7.2±0.2 (proximal), 15.2±0.5 (medial), and 35.8±0.6 grids (distal). **b**, Firing map contrast (defined as average in place field firing rate divided by the average out of place field firing rate) versus the number of presynaptic grid cells for three different distance distributions of synapses. Shown in light gray are the peak firing rate curves from a. **c**, Contrast versus peak in field firing rate for the three different distance configurations. Range of firing rate during exploratory behavior seen in-vivo (11.54±8.16 Hz) is indicated as gray box. **d**, Contrast versus mean firing rate in the whole environment for synapses placed in three different distance ranges (red: 0–85 µm from the soma, black: 85–150 µm, green: >150 µm). **e**, Mean firing rate versus number of afferent grid cells for the same synaptic distance ranges as in d.

4. Discussion

The dentate gyrus granule cells are a critical station for the relay of spatial information from the entorhinal cortex to the hippocampus proper. We examined how input that arrives in the termination zone of the perforant path projection is integrated in the very small caliber dendrites of the granule cells with a combination of advanced optical and electrophysiological methods. We then analyzed, using a modeling approach, how input integration can influence the generation of place fields in dentate gyrus granule cells.

4.1. Major findings

The key questions that were raised at the end of the introduction could be answered in this thesis.

- Attenuation of both EPSPs propagating towards the soma and action potentials propagating back into the dendrites, was strong. In particular, all EPSPs originating distally were attenuated by virtually the same amount, indicating that attenuation is uniform for most of the granule cells inputs. The most parsimonious explanation for the observed propagation of action potentials and EPSPs is a low functional expression of voltage-gated ion channels in the dendrites of granule cells.

- The attenuation of slow voltage deflections and sum EPSPs with intermediate synchrony is less pronounced. Compared to the dendritic integration time window the somatic time window for integration is enlarged. As a result granule cells are less sensitive to jitter in the timing of inputs and favor continuously arriving or tonic input.

- The integration of EPSPs on one dendritic segment is linearized by activation of NMDA receptors and sodium channels and by the enhanced propagation

of slow compound EPSPs. These mechanisms compensate for the local loss of driving force and enable granule cells to integrate large amounts of input in a linear fashion. Integration of EPSPs from daughter branches and from different pathways is also linear. Together with the uniform attenuation of inputs this renders integration less dependent on the position of inputs along the dendritic tree.

- Granule cells equipped with these active and passive linearization mechanisms can generate place field firing from grid cell inputs. For a high place field contrast synapses need to be electrotonically distant from the granule cell soma.

In summary, granule cell dendrites behave as linear integrators, are capable of summing large amounts of inputs, tolerating temporal jitter and favor continuously arriving or tonic inputs—making them particularly suitable to generate place field output from linear summation of grid cell input.

4.2. Granule cells as strong, uniform, and frequency-dependent attenuators

We demonstrated that input resistance, steady-state transfer resistance, and the frequency-dependent transfer impedance that were measured by simultaneous dendritic and somatic patch-clamp recordings are well replicated by a computational model incorporating only passive membrane properties. These basic membrane properties used in our model were derived in other studies from the analysis of voltage decay transients (Spruston and Johnston, 1992; Schmidt-Hieber et al., 2007) and seem to match the observed dendritic properties. In particular, the high dendritic input resistance which increased with distance from the soma, was expected from the computational analysis. In the experiments, the steady-state voltage transfer showed a marked directionality. Voltage transfer from the soma to the dendrite was much more effective than vice versa and was nearly independent of the distance of the dendritic site from the soma (fig. 3.6, p. 42). This was expected from basic cable theory, since the soma has a lower input resistance than the dendrites.

Dendritic integration and resonance behavior are influenced by hyperpolarization activated currents (I_h) that are expressed in the soma and dendrites of many pyra-

midal neurons. The resonance observed in e.g. CA1 pyramidal neurons is tuned to the hippocampal theta frequency and probably plays an important role in the theta phase-locking of these neurons (Magee, 2001). Granule cell somata express only very small h-currents (Stabel et al., 1992) and do not show resonance (this thesis). Here, we additionally demonstrated that neither the soma nor the dendritic compartments of granule cells show theta resonance at resting membrane potential (fig. 3.7, p. 43), which would be caused by h-currents (Hu et al., 2002). Also no prominent sag was observed upon long dendritic current injections. We did not test, however, if resonance occurs at depolarized holding potentials. In CA1 pyramidal cells this is the case and is caused by an interplay between a persistent sodium current and an M-current. The persistent sodium current in granule cell dendrites (see below) could work together with an M-current to create dendritic resonance at depolarized membrane potentials (Hu et al., 2002).

Taken together, the data in this thesis indicate that there is neither dendritic resonance nor an interplay of dendritic and somatic resonance that could strengthen a theta phase lock in dentate granule cells. Since granule cells do fire phase locked to the hippocampal theta rhythm in-vivo (Skaggs et al., 1996), other mechanisms must underly this phenomenon. Conceivably, the theta phase relationship is inherited from the entorhinal cortex, since the presynaptic grid cells in layer II show theta phase modulation (Hafting et al., 2008).

4.2.1. Action potential backpropagation

Backpropagating action potentials are an important electrical signal in dendrites, crucial for e.g. spike-timing-dependent plasticity (Caporale and Dan, 2008). In dentate gyrus granule cells action potentials do backpropagate into the dendritic tree (fig. 3.2, p. 36). The initiation sites for action potentials are the somatic or axonal compartments, as is evident from the delayed action potential peak at dendritic sites relative to the soma. The amplitude attenuation that was observed at the dendritic sites is quite drastic. Further analysis in the computational model showed that this attenuation is only consistent with a low functional expression of sodium channels ($1\,\mathrm{mS/cm^2}$) in the dendrites (fig. 3.5, p. 41). Higher available sodium channels densities, e.g. $6\,\mathrm{mS/cm^2}$ as found in CA1 pyramidal neuron dendrites (Magee and Johnston, 1995a), lead to an active backpropagation of action potentials in the computational model, which is not consistent with the experimental results. More

evidence pointing towards a low sodium channel density is the constant amplitude of trains of action potentials evoked by long current injections into the soma (fig. 3.2b, p. 36). In all other neuronal dendrites studied so far the amplitudes of successive backpropagating action potentials in a train decrease. It was shown that the recovery from inactivation is very slow for dendritically expressed sodium channels and thus successive backpropagating action potentials have a decreasing density of available channels (Jung et al., 1997). This is clearly not the case in granule cell dendrites. The most straightforward explanation is that action potentials do not backpropagate actively into granule cell dendrites consistent with a low density of sodium channels.

4.2.2. EPSP attenuation and input coupling

What happens to dendritic EPSPs on their way to the soma? Local dendritic EPSPs experience strong attenuation and slowing of their rise and decay phases on their way to the soma (see introduction, section 1.1.1). The experimental data suggest a strong and nearly uniform attenuation of distal EPSPs (fig. 3.1, p. 35). Analysis in the computational model showed, that the strongest attenuation actually takes place in the last 80–100 µm before the soma (fig. 3.4, p. 40). This is most probably caused by the impedance mismatch at branchpoints (Goldstein and Rall, 1974), which are mainly located near the soma and contribute strongly to the overall attenuation; thus all EPSPs originating more distally are attenuated by nearly the same amount.

What are the consequences of this observed EPSP attenuation? Every neuron with long dendrites faces the problem that depolarization in electrotonically distant dendritic compartments can only have a limited influence on the somatic depolarization (equation 1.5, p. 2). It may even be impossible for excitatory input on one dendritic segment to bring the somatic membrane potential to threshold and trigger an action potential. This problem is also apparent in granule cell dendrites, where distal dendritic EPSPs are heavily attenuated. Only very proximal input can achieve efficient somatic depolarization. This leads to the conclusion that, if granule cell firing is dominated by perforant path inputs, the dendrites need large amounts of distal inputs to reach firing threshold. Additionally, large amounts of very synchronous input are not the most efficient way to depolarize the granule cell soma, because of the strong filtering of fast inputs. Slightly asynchronous inputs, leading to a kind of plateau depolarization in the dendrite, are transmitted more efficiently to the soma (see below).

Neurons have evolved mechanisms to overcome the large electrotonic distance between distal input sites and the soma.

- As was introduced above (see introduction, sections 1.1.2 and 1.1.3), pyramidal neurons use different forms of active spiking mechanisms to increase the coupling of apical dendrites to the soma (Larkum et al., 1999, 2009; Golding and Spruston, 1998; Golding et al., 1999). After these regenerative events are triggered at a distal dendritic site they can often propagate in an active fashion to the soma, much more efficient than the input alone that triggered them. An extreme example are the apical tuft dendrites of cortical layer V pyramidal neurons that would have virtually no influence on the somatic membrane potential, without specialized active mechanisms (Larkum et al., 2009). For a discussion of dendritic spikes in granule cells see below.

- For intermediate electrotonic distances a scaling of the number of AMPA receptors incorporated into synapses was observed in CA1 pyramidal neurons (Magee and Cook, 2000; Andrasfalvy and Magee, 2001; Smith et al., 2003). More distal synapses generate a bigger local EPSP than more proximal ones, in a way that the EPSPs observed at the soma have the same size. This mechanisms could be less effective in-vivo under conditions of high synaptic background activity (London and Segev, 2001).

- A third and very simple mechanisms to increase the somatic impact of electrotonically distant synapse is passive normalization (Jaffe and Carnevale, 1999). This means that the transfer impedance is less affected by dendritic location than voltage transfers. Thus equally sized synapses, while creating different local EPSPs because of the location dependent input resistance, give rise to nearly equal somatic EPSPs (equation 1.10, p. 4). This passive normalization was demonstrated in a computational model in neurons that lack long primary dendrites, as CA3 pyramidal neurons or dentate gyrus granule cells. The presence of a long primary dendrite in e.g. CA1 or layer V pyramidal neurons, on the other hand, favors a substantial location-dependent variability of the somatic EPSP size.

As we could show in this thesis, dentate gyrus granule cells do not implement dendritic spikes to overcome the strong dendritic attenuation. If synapses of granule cells are scaled according to the attenuation of their EPSPs remains an open question.

The passive normalization, which was described theoretically, is clearly present in granule cell dendrites.

4.3. Enhanced time window for dendritic integration

The integration time window observed in dentate gyrus granule cells can be explained by the passive membrane properties alone. They determine both local summation and propagation of inputs. Obviously, the maximal local depolarization is reached by synchronous synaptic input, and summation of inputs with a lower degree of synchrony leads to a smaller local depolarization (the smaller the bigger the interval). The somatic peak depolarization, however, is additionally determined by the propagation from the dendritic location towards the soma. It was found that in granule cells propagation favors slightly asynchronous input, in part compensating the non-optimal local summation. Thus, both synchronous and slightly asynchronous input can lead to the same somatic peak depolarization (fig. 3.8, p. 45). The enlarged somatic integration time window could make the granule cell output less sensitive to input timing fluctuations and contributes to their integrator function, since exact input synchronization is less significant for the somatic integration. An exact synchronization of inputs could nevertheless be important for local interactions in the dendrites. Action potential output of the presynaptic grid cells in the entorhinal cortex shows considerable jitter (see fig. 1 in Hafting et al., 2008) which could be compensated by the integration time window of granule cells.

Enlarged integration time windows in the somatic versus dendritic compartments can also be observed in other neurons (see fig. 1 in Migliore and Shepherd, 2002), but they are often additionally modified by many dendritic voltage-gated conductances (e.g. I_H, Magee, 1999, I_A, Kim et al., 2007, and $I_{Na,P}$, Schwindt and Crill, 1995, see introduction, section 1.1.2). These voltage-gated mechanisms are then the determining factors for the local integration and subsequent propagation to the soma.

4.3.1. Properties of other small caliber dendrites

Most of the knowledge about dendritic integration is derived from direct patch-clamp recordings of dendrites. Until recently, this technique was limited to the thick stem dendrites of hippocampal and cortical pyramidal neurons and cerebellar

Purkinje neurons (Davie et al., 2006). Fine dendrites, although the major targets of excitatory inputs (Megias et al., 2001), are rarely studied because of the technical difficulties linked to recordings of their electrical properties. Nevertheless, with different optical methods several groups have succeeded in imaging even small voltage transients in thin neuronal processes. This is due to improvements in two-photon microscope technology (Sacconi et al., 2008) and recent advances in single-photon voltage imaging with small band laser excitation (Holthoff et al., 2010; Foust et al., 2010; Canepari et al., 2010; Palmer and Stuart, 2009). Also the development of new voltage sensitive dyes with high sensitivity could improve the feasibility of optical methods (Li, 2007; Sjulson and Miesenböck, 2008; Baker et al., 2008; Kee et al., 2009). Another recent study used a Förster resonance energy transfer-based voltage imaging technique with an intracellular dye and an extracellular quencher whose membrane partitioning was voltage-sensitive (Bradley et al., 2009). However, the extracellular quencher adds capacitative load to the cell membranes that could disturb dendritic signaling. A caveat in the application of most voltage imaging methods with synthetic dyes is the probable modulation of $GABA_A$ receptor function (Mennerick et al., 2010, but see Canepari et al., 2010).

The feasibility of direct electrophysiological recordings from fine dendrites was shown in the pioneering study by Nevian et al. (2007), who recorded from basal dendrites of cortical layer V pyramidal neurons. They used a combination of two-photon fluorescence imaging and infrared scanning gradient contrast (similar to the method used in this thesis) to gain access to the otherwise invisible thin dendrites with very small, high resistance patch electrodes. The groups of Thomas Nevian and Matthew Larkum further developed this technique to study other small caliber dendrites, such as layer V neuron apical tuft dendrites (Larkum et al., 2009) and layer II/III neuron apical dendrites (Bathellier et al., 2009).

It should be noted that the study of dendritic function is currently expanded to in-vivo experiments (Kitamura et al., 2008; Jia et al., 2010). This approach will certainly fertilize the field of dendritic research and give new insights into how dendrites compute and how they influence action potential output in behaving animals.

4.4. Granule cells as linear integrators

We showed in this thesis that the integration of colocalized inputs is linear in dentate gyrus granule cells. A linear gain of around 40% was observed in addition (fig. 3.11, p. 49). Although often readily assumed in theoretical models, e.g. in Hopfield and Tank (1986); Solstad et al. (2006), linear integration over a wide range of input strengths is—contrary to intuition—not a simple task for a neuron. Inherent to synaptic activity, two nonlinear effects cause summation of colocalized inputs to be sublinear and ultimately saturating, without further compensatory mechanisms. Both, local loss of driving force and mutual shunting decrease the impact of colocalized synapses (see introduction, section 1.1.1). The observed linear integration of colocalized inputs indicates the presence of other, compensatory nonlinear mechanisms.

Indeed, integration was sublinear in the presence of either sodium channel blocker TTX or NMDA receptor blocker D-APV. Both, voltage-gated sodium channels and NMDA receptors open upon depolarization[1] and can thus add to the depolarization from the activation of synaptic AMPA receptors alone (see introduction, sections 1.1.2 and 1.1.3).

Arguably, the boosting conveyed by both sodium channels and NMDA receptors cannot linearize the summation of colocalized inputs for all input strengths. For very strong local depolarizations the loss of driving force outweighs the boosting effect, integration is necessarily sublinear, and the local membrane potential saturates. However, the input strength for which sublinear integration and saturation occur is considerably larger with active boosting mechanisms.

We could demonstrate that the dendritic integration saturates by evoking very large sum EPSPs and additionally depolarizing the cell in the presence of D-APV. In this case the sum EPSPs display sublinear summation and eventually saturate, due to the local dendritic depolarization approaching the synaptic equilibrium potential[2]. This observation clearly shows that the local loss of driving force is an important factor for local summation of input. Additionally, maximal depolarization in a single distal dendritic compartment is unable to bring the granule cell soma to action potential threshold.

[1] NMDA receptors additionally need glutamate, either released synaptically or by uncaging.

[2] Assuming a local depolarization of 70 mV and comparing with the somatic plateau depolarization at saturation one can derive a steady-state attenuation of 0.23. This is near the expected value of 0.18 derived from the dual somato-dendritic patch-clamp recordings.

4.4.1. Linearization by sodium channels

The mechanism underlying the observed TTX sensitivity of boosting is probably the activation of a persistent sodium current located in the dendrites, similar to findings in other neurons types (Deisz et al., 1991; Schwindt and Crill, 1995; Crill, 1996). In the uncaging experiments, application of TTX affected both integration and the single gluEPSP waveform. A dendritic persistent sodium current could be activated by both single EPSPs (see e.g. fig. 7 in Vervaeke et al., 2006) and even more by sum EPSPs that reach higher depolarizations locally (see e.g. fig. 9 in Deisz et al., 1991) in the range of maximal persistent sodium current (at around -40 mV, Crill, 1996; French et al., 1990). A more recent study showed that in neocortical layer V pyramidal neurons the sodium current-dependent EPSP boosting is mediated by sodium channels on spines rather than on the dendritic shaft (Araya et al., 2007). The presence of sodium channels in single spines and their contribution to spine calcium transients was also demonstrated in CA1 pyramidal neurons (Bloodgood and Sabatini, 2007). In contrast, Palmer and Stuart (2009) did not find evidence for the contribution of voltage-gated ion channels to the amplitude of single EPSPs in basal dendrites of layer V pyramidal neurons. However, under their conditions they estimate the depolarization reached in the spine to be on average 13 mV, probably not enough to activate voltage-gated sodium channels (Palmer and Stuart, 2009). Nevertheless, when several spines are stimulated simultaneously, as in this thesis, the local depolarization could be high enough to activate sodium channels, which then amplify the sum EPSP.

Unfortunately, the electrophysiological current-clamp experiments in this thesis cannot determine the sodium current density in the dendrites, so that the evidence for the low available sodium channel density and the persistent nature of the dendritic sodium current remain indirect.

4.4.2. Linearization by NMDA receptors

Probably all neurons express NMDA type glutamate receptors besides AMPA type glutamate receptors. The ratio of the maximal synaptic AMPA and NMDA receptor mediated currents, however, varies between different neuronal cell types, between different synapses in a single neuron, and during development (Huntley et al., 1994; Nusser, 2000; Andrasfalvy and Magee, 2001; Kerchner and Nicoll, 2008). Dentate

gyrus granule cells have a relatively high NMDA to AMPA ratio of approximately 1 (see Ye et al., 2005 and fig. 2.2, p. 25). In comparison, e.g. Schaffer collateral synapses of CA1 pyramidal neurons exhibit a much lower ratio of only 0.5 (McDermott et al., 2006) or 0.2 (as mentioned in Losonczy and Magee, 2006). The NMDA receptors of granule cell synapses additionally show a prominent contribution to the EPSP size even at resting membrane potentials (Keller et al., 1991; Dalby and Mody, 2003), also under in-vivo conditions (Blanpied and Berger, 1992). Regarding the different modes of NMDA receptor mediated activity in the dendrites, which were introduced earlier (fig. 1.1) granule cells are clearly operating in a boosting mode that is already active near the resting membrane potential.

4.4.3. Granule cells lack regenerative events

Dendritic nonlinear events, as seen in many other neuron types (see introduction, sections 1.1.2 and 1.1.3), were never observed in granule cells, except in one single experiment where a brief dendritic current injection triggered an event resembling a dendritic sodium spike in CA1 pyramidal neurons. Why could fast sodium spikes not be generally elicited, although there seem to be sodium channels in the dendrites? The most straightforward explanation is an insufficient channel density to support dendritic spiking. Additionally, fast inactivation of the dendritic sodium channels reduces the density of available channels even further. However, it cannot be excluded that with more synchronous stimulation or faster current injection regenerative sodium channel-dependent events could be generated in dentate granule cells. Also, NMDA receptor driven spikes (Schiller et al., 2000) could not be observed, although there is a substantial NMDA receptor activation even at resting membrane potentials (see above). Regarding the scheme (fig. 1.1) of NMDA receptor activation phenomena introduced earlier, the maximally available NMDA receptor component in granule cell dendrites is probably not enough to support generation of a regenerative event and the activation of NMDA receptors only leads to EPSP boosting as described above.

4.4.4. Linearization in other neuron types

For disparate inputs, linear integration was described in many neurons. Several studies showed a regime of linear integration in CA1 pyramidal neurons (Cash

and Yuste, 1999; Gasparini and Magee, 2006) and scattered or asynchronous inputs in medium spiny neurons of the striatum, cortical layer 2/3 pyramidal cells, and GABAergic interneurons are also integrated linearly (Tamás et al., 2002). Since disparate inputs do not locally interact a linear summation is expected (equation 1.12, p. 5). However, all pyramidal neurons also implement a regime of strong nonlinear integration of synchronous and colocalized inputs by generation of dendritic spikes (Schiller et al., 2000; Larkum et al., 1999; Losonczy and Magee, 2006).

4.4.5. Linear integration of branches and pathways

Driving force loss and shunting are local effects, i.e. they only influence synapses that are electrotonically nearby. Summation of inputs from different branches is expected to be integrated in a linear fashion, given passive dendrites. This is indeed the case in dentate granule cells (fig. 3.14, p. 55). Synaptic input from two daughter branches can nevertheless trigger supralinear integration in CA1 pyramidal neurons as we showed (fig. 3.14, p. 55). Stimulation of two different input pathways, e.g. Schaffer collaterals and temporoammonic pathway, can lead to the generation of dendritic calcium spikes in CA1 pyramidal neurons (Takahashi and Magee, 2009). In dentate gyrus granule cells no interaction between the two major input pathways (medial and lateral perforant path) was observed (fig. 3.15, p. 56).

Taken together, granule cells maintain a linear integration for all distributions of inputs, both colocalized (fig. 3.11, p. 49) and disparate (figs. 3.14, p. 55 , and 3.15, p. 56).

4.4.6. Assessing dendritic function with neurotransmitter uncaging

The study of dendritic integration was enhanced by the use of two-photon uncaging of caged neurotransmitters, in particular caged glutamate. Uncaging and iontophoresis techniques allow the activation of one specific receptor type in contrast to electrical stimulation were virtually always both excitatory and inhibitory fibers are activated, which leads to a combined EPSP-IPSP sequence. In contrast to neurotransmitter iontophoresis and single-photon uncaging, the spatially much more restricted release of glutamate with two-photon uncaging allows realistic EPSP timecourses. However, the focal volume in two-photon uncaging is diffraction limited to around 1 fl and thus is still bigger than the active zone. Additionally,

only spines and not active zones can be visualized in the uncaging experiments. Together, this leads to an excessive photorelease of glutamate that directly or by diffusion can activate glutamate receptors located perisynaptically or even on the dendritic shaft. Although these problems are reduced drastically in comparison to iontophoresis, it is necessary to ensure that the uncaging-evoked EPSPs achieved resemble synaptically stimulated EPSPs. An important parameter is the amount of NMDA receptor activation, as this is directly related to the amount of boosting observed in the experiments. Especially compromising would be a higher NMDA portion of uncaging evoked EPSP in comparison to EPSP evoked by presynaptic activity. Instead of a direct comparison of uncaging evoked EPSPs (gluEPSPs) and stimulated EPSPs, gluEPSPs with different uncaging times were compared. If there is contamination by activation of additional dendritic shaft NMDA receptors, longer uncaging times should result in a higher NMDA component of single gluEPSPs and in a different gain of summed gluEPSPs. Both was clearly not the case (fig. 2.3, p. 28).

4.5. Place field generation by linear input integration

4.5.1. Optimization to granule cell function

Why is linear summation of inputs important for place field generation in granule cells? Many theoretical models of place field generation propose an arithmetic summation of selected grid cell inputs. Grid cells with the same spatial offset all overlap at one and only one point in the environment, despite their potentially different orientation and spacing. Thus, a linear summation generates a defined place field at this region of maximal overlap[3]. This model is relatively straightforward in that it does not rely on complex computational properties of granule cells and their dendrites. A bimodality of dendritic integration, as observed in e.g. CA1 pyramidal neurons, is not necessary to perform the place field computation. The granule cells, however, seem to be optimized to integrate large amounts of inputs linearly. In addition, this linear integration is performed for all kinds of inputs, synchronous

[3]The model equation being

$$f(x,y) = \left[\sum_{n=1}^{N} A_w^n g_w^n (x,y) - C_{inh} \right]_+ \tag{4.1}$$

and asynchronous, as well as clustered and disparate. Thus dentate granule cells are particularly suited to convert grid cell input into place field output according to equation 4.1.

The quality of the place field representation in granule cells is related to the size of presynaptic grid cell ensemble. If the number of grid cells is too small, a single smooth place field cannot be generated by the postsynaptic granule cell (fig. 3.16, p. 58).

Granule cells, however, are tuned in a way that they need large numbers of grid cell inputs to fire action potentials at all: the attenuation of EPSPs that originate in the termination zone of the perforant path projection from the entorhinal grid cells is strong and uniform. In addition, the difference between the resting membrane potential and action potential threshold is high compared to other neuron types.

The large amount of dendritic input results in a very strong dendritic depolarization and the NMDA receptor- and sodium channel-dependent boosting may be a way to facilitate action potential firing under these conditions. Furthermore, the boosting leads to a steep tuning curve of the granule cells, i.e. place field center firing rate versus number of grid inputs (fig. 3.17, p. 60).

However, having too much input is again ineffective for two reasons. Firstly, if the dendrites are already depolarized the synaptic equilibrium potential, activating further synapses does not lead to further depolarization. Secondly, massive amounts of inputs, which depolarize the granule cell soma tonically, can cause inactivation of somatic sodium channels, particularly in the place field center, where the most input impinges on the cell. Thus, increased input would lead to saturation or inactivation inside the place field and to suprathreshold depolarization outside the place field, effectively inverting the cell's firing pattern.

Taken together, small numbers of active presynaptic grid cells, resulting in low place field contrast, do not bring granule cells to action potential threshold, and too large numbers of active grid cells would also cause low place field contrast. The range of active presynaptic grid cells that leads to the generation of a high contrast place field is small, due to the steep tuning curve of granule cells (fig. 3.17, p. 60). In-vivo, granule cell firing is most probably stabilized by a strong recruitment of feed-back inhibition. A rapid recruitment of feed-back inhibition, facilitated by the steep granule cell tuning curve, is also beneficial for a 'winner-takes-it-all' mechanism of population activity in the dentate gyrus. This is one possible explanation for the sparse activity—only around 2–5% of all granule cells are active in any given

environment (Chawla et al., 2005)—of the dentate granule cell population. This sparse activity is a prerequisite for the pattern separation that is thought to take place in the dentate gyrus (Gilbert et al., 2001; Leutgeb et al., 2007a; Bakker et al., 2008). To generate non-overlapping output patterns for similar and overlapping input patterns the connection divergence from the small entorhinal grid cell population to the very large granule cell population, a sparse activity there, and a convergence onto the CA3 pyramidal cells is necessary (Rolls and Kesner, 2006).

In vivo studies of granule cell function were limited to tetrode recordings of firing activity in the dentate until recently. First whole-cell patch-clamp recordings from dentate gyrus granule cells from awake rats revealed that the basic electrophysiological properties are similar to what is known from experiments in brain slices. During wakefulness, granule cells receive massive amounts of subthreshold input that is coupled to gamma oscillations of the local field potential (Pernia-Andrade and Jonas, 2009). The frequency preference of dendritic transmission that we found (fig. 3.8, p. 45) may facilitate this phenomenon.

4.5.2. Linear integration in other systems

Is linear integration in dentate gyrus granule cells a unique computational feature? Few other examples of linear integration that is underlying a specific brain function have been found. In a prominent study Jagadeesh et al. (1993) recorded from simple cells in the visual cortex of anesthetized cats. These cells fire selective to a preferred direction of motion in visual stimuli. If these cells sum synaptic input linearly to produce direction selectivity, as was proposed in many models, the preference of the cell for one direction of motion should be predictable as a linear sum of the responses to stationary flashing stimuli. Indeed, Jagadeesh et al. (1993) found that the membrane potential oscillations in those neurons in response to moving gratings could exactly be predicted from a linear summation of responses to stationary grating patterns. However, this linear integration is then converted, as in most neurons, into firing output by a nonlinear mechanism, the action potential threshold.

4.5.3. NMDA receptors of the dentate gyrus in the hippocampal memory system

Despite their function in the linearization of input integration in granule cells, NMDA receptors subserve many memory functions expressed in the dentate gyrus and other hippocampal areas (Lynch, 2004). NMDA receptors are not necessary to maintain place field activity in the dentate gyrus in rooms familiar to an animal (Leutgeb et al., 2007b). But, importantly, all spatial selectivity in granule cells is lost when blocking NMDA receptors in novel environments, which raises the possibility that the spatial selectivity in granule cells is established by an NMDA receptor-dependent mechanisms that competitively selects active inputs (Leutgeb et al., 2007b). NMDA receptors also contribute to the pattern separation function of the dentate gyrus: McHugh et al. (2007) could show that mice lacking NMDA receptors specifically in dentate gyrus granule cell also lacked perforant path long-term potentiation (Bliss and Lømo, 1973) and were impaired in the ability to distinguish two similar contexts. Interestingly, downstream of the dentate gyrus, the context-specific modulation of firing rate in CA3 was reduced in the NMDA receptor knock-out mice. This suggests that the impaired pattern separation capability of the dentate gyrus was relayed to the CA3 region and reduced the capability of the CA3 ensemble to detect and amplify small differences in activity generated in similar contexts.

4.6. Outlook

Three major points for future research should be highlighted here.

- First, we examined only excitatory input in granule cell dendrites in this thesis. It is nevertheless clear that strong inhibition, in particular perisomatic feed-back inhibition, plays a major role in establishing a sparse activity pattern in the dentate granule cell population, as discussed above. How is this feed-back inhibition recruited by the activity of only a few granule cells and does it interact in a specific manner with excitatory dendritic input? What role plays the inhibitory input that terminates directly on granule cell dendrites or even on individual spine heads—how does it interact with excitatory input arriving at the same time on the same segment of the dendritic tree? A promising study elucidating interactions of excitation and feed-back inhibition in the dendrites

of CA1 pyramidal neurons is currently being performed (Müller et al., 2010). Unfortunately, a similar approach to the dentate gyrus remains elusive until forms of cell type specific stimulation have matured (e.g. optogenetic labeling and stimulation of all presynaptic neurons of one single granule cell).

- Second, we only studied granule cells separate from other components of the dentate gyrus network in this thesis, but network interactions in the dentate gyrus are manifold. Besides the recruitment of inhibition a recent study (Larimer and Strowbridge, 2009) introduced another excitatory cell type, the semilunar granule cells, which can trigger long-lasting up-states in the dentate network. To really understand the principles underlying the functional role of the dentate gyrus, it is essential to study the interaction of neurons in-vivo during wakeful behavior. Recent technological advances have been made in this direction, but have not yet been applied to the dentate gyrus.

- Third, the experiments performed in this thesis are of short duration and we did not look at changes in synaptic weight[4]. As for many other neuron types, the exact synaptic learning rules in granule cell dendrites are unknown. Undoubtedly, these learning rules are highly important for the development of stable place field representations.

[4]We performed, however, some preliminary experiments, indicating that a weak stimulation protocol without the generation of somatic action potentials may be sufficient to cause long-term potentiation (or more exact medium-term potentiation) of perforant path synapses.

A. Appendix

A.1. Artificial cerebrospinal fluids

Normal ACSF consists of (in mM): sodium chloride 125, potassium chloride 3.5, sodium phosphate dibasic 1.25, sodium carbonate 26, calcium chloride 2, magnesium chloride 2, D-glucose 15.
Sucrose ACSF consists of (in mM): sodium chloride 60, sucrose 100, potassium chloride 2.5, sodium phosphate dibasic 1.25, sodium carbonate 26, calcium chloride 1, magnesium chloride 5, D-glucose 20.
By saturating the solutions with carbogen (95% O_2 and 5% CO_2) the desired pH of 7.4 is reached.

A.2. Intracellular solutions

Potassium gluconate based current-clamp intracellular solution contains (in mM): potassium gluconate 130, potassium chloride 20, 4-(2-hydroxyethyl)-1-piperazine-ethanesulfonic acid 10, ethylene glycol tetraacetic acid 0.16, magnesium adenosine-5′-triphosphate 2, disodium adenosine-5′-triphosphate 2. A pH of 7.25 is set with potassium hydroxide and the osmolality is adjusted with sucrose to 295 mOsm.
Cesium based voltage-clamp intracellular solution consists of (in mM): cesium methanesulfonate 100, tetraethylammonium chloride hydrate 20, calcium chloride 0.05, magnesium adenosine-5′-triphosphate 2, disodium adenosine-5′-triphosphate 1, 4-(2-hydroxyethyl)-1-piperazineethanesulfonic acid 10, ethylene glycol tetraacetic acid 0.5. A pH of 7.25 is set with cesium hyroxide and the osmolality is adjusted with sucrose to 295 mOsm.

A.3. Estimation of the expected sum EPSP when correcting for loss of driving force incurred during large synchronous EPSPs

The arithmetic sum of all the 13 somatic gluEPSPs shown in fig. 3.11b is 6.1 mV (see fig. 3.11d, p. 49). Assuming the dendritic membrane potential to be -86 mV (-72 mV measured at the soma and corrected for the liquid-junction potential of +14 mV) this would correspond to a dendritic peak depolarization to -35 mV, assuming an attenuation factor of 0.12 (see fig. 3.1e, p. 35). The depolarization by the average single gluEPSP of 0.48 mV at the soma corresponds to a dendritic depolarization to -82 mV. Assuming a synaptic reversal potential of 0 mV the loss of driving force is around 60%. Thus, the expected linear sum gluEPSP at the soma corrected for driving force loss is just 2.6 mV.

A.4. Inhibition in the computational model

Synaptic inhibition was not incorporated into our computational model of place field generation. We reason that an inhibitory parameter modeling feed-forward inhibition would correspond to a downscaling of individual synaptic weights. Regarding feed-back inhibition, two scenarios are possible. The modeled granule cell is the 'winner' cell that generates a spike output and concurrently inhibits surrounding granule cells. Alternatively, the modeled granule cell could be inhibited based on a general feedback paradigm derived from its own firing rate. In this case, increasing inhibition would occur for increased granule cell firing, ultimately limiting the maximally achievable firing rates. The onset of the peak rate/grid relationship (see fig. 3.17a, p. 60), however, would be unchanged, as would the quality of the place field contrast in this region (see fig. 3.17b, p. 60).

B. Bibliography

Acsády, L. and Káli, S. (2007). Models, structure, function: the transformation of cortical signals in the dentate gyrus. *Prog Brain Res*, 163:577–599.

Agmon-Snir, H., Carr, C. E., and Rinzel, J. (1998). The role of dendrites in auditory coincidence detection. *Nature*, 393(6682):268–272.

Alme, C. B., Buzzetti, R. A., Marrone, D. F., Leutgeb, J. K., Chawla, M. K., Schaner, M. J., Bohanick, J. D., Khoboko, T., Leutgeb, S., Moser, E. I., Moser, M.-B., McNaughton, B. L., and Barnes, C. A. (2010). Hippocampal granule cells opt for early retirement. *Hippocampus*.

de Almeida, L., Idiart, M., and Lisman, J. E. (2009). The input-output transformation of the hippocampal granule cells: from grid cells to place fields. *J Neurosci*, 29(23):7504–7512.

Amaral, D. G., Scharfman, H. E., and Lavenex, P. (2007). The dentate gyrus: fundamental neuroanatomical organization (dentate gyrus for dummies). *Prog Brain Res*, 163:3–22.

Amaral, D. G. and Witter, M. P. (1989). The three-dimensional organization of the hippocampal formation: a review of anatomical data. *Neuroscience*, 31(3):571–591.

Amitai, Y., Friedman, A., Connors, B. W., and Gutnick, M. J. (1993). Regenerative activity in apical dendrites of pyramidal cells in neocortex. *Cereb Cortex*, 3(1):26–38.

Andersen, P., Holmqvist, B., and Voorhoeve, P. E. (1966). Entorhinal activation of dentate granule cells. *Acta Physiol Scand*, 66(4):448–460.

Andrasfalvy, B. K. and Magee, J. C. (2001). Distance-dependent increase in AMPA receptor number in the dendrites of adult hippocampal CA1 pyramidal neurons. *J Neurosci*, 21(23):9151–9159.

Andreasen, M. and Lambert, J. D. (1995). Regenerative properties of pyramidal cell dendrites in area CA1 of the rat hippocampus. *J Physiol*, 483:421–441.

Antic, S. D. (2003). Action potentials in basal and oblique dendrites of rat neocortical pyramidal neurons. *J Physiol*, 550:35–50.

Aradi, I. and Holmes, W. R. (1999). Role of multiple calcium and calcium-dependent conductances in regulation of hippocampal dentate granule cell excitability. *J Comput Neurosci*, 6(3):215–235.

Aranzi, G. C. (1587). *Iulii Caesaris Arantii medicinae atque Anatomes Pub. professoris De humano foetu liber: Tertio editus, ac recognitus. Eiusdem Anatomicarum observationum liber ac De tumoribus secundum locos affectos liber. Nunc primum editi.* Apud Jacobum Brechtanum, Venetiis.

Araya, R., Eisenthal, K. B., and Yuste, R. (2006). Dendritic spines linearize the summation of excitatory potentials. *Proc Natl Acad Sci USA*, 103(49):18799–18804.

Araya, R., Nikolenko, V., Eisenthal, K. B., and Yuste, R. (2007). Sodium channels amplify spine potentials. *Proc Natl Acad Sci USA*, 104(30):12347–12352.

Ariav, G., Polsky, A., and Schiller, J. (2003). Submillisecond precision of the input-output transformation function mediated by fast sodium dendritic spikes in basal dendrites of CA1 pyramidal neurons. *J Neurosci*, 23(21):7750–7758.

Baer, S., Hummel, G., and Goller, H. (1985). Feinstruktur des Ammonshornes von Rind, Schaf und Ziege. *Anat Histol Embryol*, 14(3):242–261.

Baker, B., Mutoh, H., Dimitrov, D., Akemann, W., Perron, A., Iwamoto, Y., Jin, L., Cohen, L., Isacoff, E., Pieribone, V., Hughes, T., and Knöpfel, T. (2008). Genetically encoded fluorescent sensors of membrane potential. *Brain Cell Biol*, 36:53–67.

Bakker, A., Kirwan, C. B., Miller, M., and Stark, C. E. L. (2008). Pattern separation in the human hippocampal CA3 and dentate gyrus. *Science*, 319(5870):1640–1642.

Barrett, J. N. and Crill, W. E. (1974). Influence of dendritic location and membrane properties on the effectiveness of synapses on cat motoneurones. *J Physiol*, 239(2):325–345.

Bathellier, B., Margrie, T. W., and Larkum, M. E. (2009). Properties of piriform cortex pyramidal cell dendrites: implications for olfactory circuit design. *J Neurosci*, 29(40):12641–12652.

Beck, H., Clusmann, H., Kral, T., Schramm, J., Heinemann, U., and Elger, C. E. (1997). Potassium currents in acutely isolated human hippocampal dentate granule cells. *J Physiol*, 498:73–85.

Beck, H., Ficker, E., and Heinemann, U. (1992). Properties of two voltage-activated potassium currents in acutely isolated juvenile rat dentate gyrus granule cells. *J Neurophysiol*, 68(6):2086–2099.

Benardo, L. S., Masukawa, L. M., and Prince, D. A. (1982). Electrophysiology of isolated hippocampal pyramidal dendrites. *J Neurosci*, 2(11):1614–1622.

Bernander, O., Douglas, R. J., Martin, K. A., and Koch, C. (1991). Synaptic background activity influences spatiotemporal integration in single pyramidal cells. *Proc Natl Acad Sci USA*, 88(24):11569–11573.

Biscoe, T. J. and Duchen, M. R. (1985). An intracellular study of dentate, CA1 and CA3 neurones in the mouse hippocampal slice. *Q J Exp Physiol*, 70(2):189–202.

Blackstad, T. W. (1958). On the termination of some afferents to the hippocampus and fascia dentata; an experimental study in the rat. *Acta Anat (Basel)*, 35(3):202–214.

Blanpied, T. A. and Berger, T. W. (1992). Characterization in vivo of the NMDA receptor-mediated component of dentate granule cell population synaptic responses to perforant path input. *Hippocampus*, 2(4):373–388.

Blaxter, T. J., Carlen, P. L., and Niesen, C. (1989). Pharmacological and anatomical separation of calcium currents in rat dentate granule neurones in vitro. *J Physiol*, 412:93–112.

Bliss, T. V. and Lømo, T. L. (1973). Long-lasting potentiation of synaptic transmission in the dentate area of the anaesthetized rabbit following stimulation of the perforant path. *J Physiol*, 232(2):331–356.

Bloodgood, B. L. and Sabatini, B. L. (2007). Nonlinear regulation of unitary synaptic signals by $CaV_{2.3}$ voltage-sensitive calcium channels located in dendritic spines. *Neuron*, 53(2):249–260.

Bradley, J., Luo, R., Otis, T. S., and DiGregorio, D. A. (2009). Submillisecond optical reporting of membrane potential in situ using a neuronal tracer dye. *J Neurosci*, 29(29):9197–9209.

Brette, R., Piwkowska, Z., Monier, C., Rudolph-Lilith, M., Fournier, J., Levy, M., Frégnac, Y., Bal, T., and Destexhe, A. (2008). High-resolution intracellular recordings using a real-time computational model of the electrode. *Neuron*, 59(3):379–391.

Brown, T. H., Fricke, R. A., and Perkel, D. H. (1981). Passive electrical constants in three classes of hippocampal neurons. *J Neurophysiol*, 46(4):812–827.

Butz, E. G. and Cowan, J. D. (1974). Transient potentials in dendritic systems of arbitrary geometry. *Biophys J*, 14(9):661–689.

Buzsáki, G. (1986). Hippocampal sharp waves: their origin and significance. *Brain Res*, 398(2):242–252.

Canepari, M., Willadt, S., Zecevic, D., and Vogt, K. E. (2010). Imaging inhibitory synaptic potentials using voltage sensitive dyes. *Biophys J*, 98(9):2032–2040.

Cao, B. J. and Abbott, L. F. (1993). A new computational method for cable theory problems. *Biophys J*, 64(2):303–313.

Caporale, N. and Dan, Y. (2008). Spike timing-dependent plasticity: a hebbian learning rule. *Annu Rev Neurosci*, 31:25–46.

Carnevale, N. T. and Hines, M. L. (2006). *The NEURON Book*. Cambridge University Press.

Carnevale, N. T., Tsai, K. Y., Claiborne, B. J., and Brown, T. H. (1997). Comparative electrotonic analysis of three classes of rat hippocampal neurons. *J Neurophysiol*, 78(2):703–720.

Carter, A. G., Soler-Llavina, G. J., and Sabatini, B. L. (2007). Timing and location of synaptic inputs determine modes of subthreshold integration in striatal medium spiny neurons. *J Neurosci*, 27(33):8967–8977.

Cash, S. and Yuste, R. (1998). Input summation by cultured pyramidal neurons is linear and position-independent. *J Neurosci*, 18(1):10–15.

Cash, S. and Yuste, R. (1999). Linear summation of excitatory inputs by CA1 pyramidal neurons. *Neuron*, 22(2):383–394.

Chawla, M. K., Guzowski, J. F., Ramirez-Amaya, V., Lipa, P., Hoffman, K. L., Marriott, L. K., Worley, P. F., McNaughton, B. L., and Barnes, C. A. (2005). Sparse, environmentally selective expression of Arc RNA in the upper blade of the rodent fascia dentata by brief spatial experience. *Hippocampus*, 15(5):579–586.

Chklovskii, D. B. (2004). Synaptic connectivity and neuronal morphology: two sides of the same coin. *Neuron*, 43(5):609–617.

Claiborne, B. J., Amaral, D. G., and Cowan, W. M. (1990). Quantitative, three-dimensional analysis of granule cell dendrites in the rat dentate gyrus. *J Comp Neurol*, 302(2):206–219.

Clelland, C. D., Choi, M., Romberg, C., Clemenson, G. D., Fragniere, A., Tyers, P., Jessberger, S., Saksida, L. M., Barker, R. A., Gage, F. H., and Bussey, T. J. (2009). A functional role for adult hippocampal neurogenesis in spatial pattern separation. *Science*, 325(5937):210–213.

Crill, W. E. (1996). Persistent sodium current in mammalian central neurons. *Annu Rev Physiol*, 58:349–362.

Dalby, N. O. and Mody, I. (2003). Activation of NMDA receptors in rat dentate gyrus granule cells by spontaneous and evoked transmitter release. *J Neurophysiol*, 90(2):786–797.

Davie, J. T., Kole, M. H. P., Letzkus, J. J., Rancz, E. A., Spruston, N., Stuart, G. J., and Häusser, M. (2006). Dendritic patch-clamp recording. *Nat Protoc*, 1(3):1235–1247.

Deisz, R. A., Fortin, G., and Zieglgänsberger, W. (1991). Voltage dependence of excitatory postsynaptic potentials of rat neocortical neurons. *J Neurophysiol*, 65(2):371–382.

Deller, T. (1998). The anatomical organization of the rat fascia dentata: new aspects of laminar organization as revealed by anterograde tracing with Phaseolus vulgaris-Leucoagglutinin (PHA-L). *Anat Embryol (Berlin)*, 197(2):89–103.

Desmond, N. L. and Levy, W. B. (1982). A quantitative anatomical study of the granule cell dendritic fields of the rat dentate gyrus using a novel probabilistic method. *J Comp Neurol*, 212(2):131–145.

Desmond, N. L. and Levy, W. B. (1985). Granule cell dendritic spine density in the rat hippocampus varies with spine shape and location. *Neurosci Lett*, 54:219–224.

Diba, K. and Buzsáki, G. (2008). Hippocampal network dynamics constrain the time lag between pyramidal cells across modified environments. *J Neurosci*, 28(50):13448–13456.

Dietrich, D., Clusmann, H., Kral, T., Steinhäuser, C., Blümcke, I., Heinemann, U., and Schramm, J. (1999). Two electrophysiologically distinct types of granule cells in epileptic human hippocampus. *Neuroscience*, 90(4):1197–1206.

Dingledine, R., Borges, K., Bowie, D., and Traynelis, S. F. (1999). The glutamate receptor ion channels. *Pharmacol Rev*, 51(1):7–61.

Doinikow, B. (1908). Beitrag zur vergleichenden Histologie des Ammonshorns. *J Psychol Neurol*, 13:166–202.

Dudek, F. E., Deadwyler, S. A., Cotman, C. W., and Lynch, G. (1976). Intracellular responses from granule cell layer in slices of rat hippocampus: perforant path synapse. *J Neurophysiol*, 39(2):384–393.

Durand, D., Carlen, P. L., Gurevich, N., Ho, A., and Kunov, H. (1983). Electrotonic parameters of rat dentate granule cells measured using short current pulses and HRP staining. *J Neurophysiol*, 50(5):1080–1097.

Ekstrom, A. D., Kahana, M. J., Caplan, J. B., Fields, T. A., Isham, E. A., Newman, E. L., and Fried, I. (2003). Cellular networks underlying human spatial navigation. *Nature*, 425(6954):184–188.

Eliot, L. S. and Johnston, D. (1994). Multiple components of calcium current in acutely dissociated dentate gyrus granule neurons. *J Neurophysiol*, 72(2):762–777.

Engel, D. and Jonas, P. (2005). Presynaptic action potential amplification by voltage-gated Na^+ channels in hippocampal mossy fiber boutons. *Neuron*, 45(3):405–417.

Fisher, R. E., Gray, R., and Johnston, D. (1990). Properties and distribution of single voltage-gated calcium channels in adult hippocampal neurons. *J Neurophysiol*, 64(1):91–104.

Foust, A., Popovic, M., Zecevic, D., and McCormick, D. A. (2010). Action potentials initiate in the axon initial segment and propagate through axon collaterals reliably in cerebellar purkinje neurons. *J Neurosci*, 30(20):6891–6902.

Franzius, M., Vollgraf, R., and Wiskott, L. (2007). From grids to places. *J Comput Neurosci*, 22(3):297–299.

French, C. R., Sah, P., Buckett, K. J., and Gage, P. W. (1990). A voltage-dependent persistent sodium current in mammalian hippocampal neurons. *J Gen Physiol*, 95(6):1139–1157.

Freund, T. F. and Buzsáki, G. (1996). Interneurons of the hippocampus. *Hippocampus*, 6(4):347–470.

Fricke, R. A. and Prince, D. A. (1984). Electrophysiology of dentate gyrus granule cells. *J Neurophysiol*, 51(2):195–209.

Fyhn, M., Molden, S., Witter, M. P., Moser, E. I., and Moser, M.-B. (2004). Spatial representation in the entorhinal cortex. *Science*, 305(5688):1258–1264.

Gasparini, S. and Magee, J. C. (2006). State-dependent dendritic computation in hippocampal CA1 pyramidal neurons. *J Neurosci*, 26(7):2088–2100.

Gilbert, P. E., Kesner, R. P., and Lee, I. (2001). Dissociating hippocampal subregions: double dissociation between dentate gyrus and CA1. *Hippocampus*, 11(6):626–636.

Gillessen, T. and Alzheimer, C. (1997). Amplification of EPSPs by low Ni^{2+}- and amiloride-sensitive Ca^{2+} channels in apical dendrites of rat CA1 pyramidal neurons. *J Neurophysiol*, 77(3):1639–1643.

Golding, N. L., Jung, H. Y., Mickus, T., and Spruston, N. (1999). Dendritic calcium spike initiation and repolarization are controlled by distinct potassium channel subtypes in CA1 pyramidal neurons. *J Neurosci*, 19(20):8789–8798.

Golding, N. L. and Spruston, N. (1998). Dendritic sodium spikes are variable triggers of axonal action potentials in hippocampal CA1 pyramidal neurons. *Neuron*, 21(5):1189–1200.

Golding, N. L., Staff, N. P., and Spruston, N. (2002). Dendritic spikes as a mechanism for cooperative long-term potentiation. *Nature*, 418(6895):326–331.

Goldstein, S. S. and Rall, W. (1974). Changes of action potential shape and velocity for changing core conductor geometry. *Biophys J*, 14(10):731–757.

Golgi, C. (1886). *Sulla fina anatomica degli organi centrali del sistema nervoso*. Hoepli, Milan.

Gulledge, A. T., Kampa, B. M., and Stuart, G. J. (2005). Synaptic integration in dendritic trees. *J Neurobiol*, 64(1):75–90.

Hafting, T., Fyhn, M., Bonnevie, T., Moser, M.-B., and Moser, E. I. (2008). Hippocampus-independent phase precession in entorhinal grid cells. *Nature*, 453(7199):1248–1252.

Hafting, T., Fyhn, M., Molden, S., Moser, M.-B., and Moser, E. I. (2005). Microstructure of a spatial map in the entorhinal cortex. *Nature*, 436(7052):801–806.

Hama, K., Arii, T., and Kosaka, T. (1989). Three-dimensional morphometrical study of dendritic spines of the granule cell in the rat dentate gyrus with HVEM stereo images. *J Electron Microsc Tech*, 12(2):80–87.

Häusser, M. and Mel, B. (2003). Dendrites: bug or feature? *Curr Opin Neurobiol*, 13(3):372–383.

Häusser, M., Spruston, N., and Stuart, G. J. (2000). Diversity and dynamics of dendritic signaling. *Science*, 290(5492):739–744.

Hayman, R. M. and Jeffery, K. J. (2008). How heterogeneous place cell responding arises from homogeneous grids—a contextual gating hypothesis. *Hippocampus*, 18(12):1301–1313.

Henze, D. A., Wittner, L., and Buzsáki, G. (2002). Single granule cells reliably discharge targets in the hippocampal CA3 network in vivo. *Nat Neurosci*, 5(8):790–795.

Hines, M. L., Morse, T., Migliore, M., Carnevale, N. T., and Shepherd, G. M. (2004). ModelDB: a database to support computational neuroscience. *J Comput Neurosci*, 17(1):7–11.

Hjorth-Simonsen, A. (1972). Projection of the lateral part of the entorhinal area to the hippocampus and fascia dentata. *J Comp Neurol*, 146(2):219–232.

Hjorth-Simonsen, A. and Jeune, B. (1972). Origin and termination of the hippocampal perforant path in the rat studied by silver impregnation. *J Comp Neurol*, 144(2):215–232.

Hoffman, D. A., Magee, J. C., Colbert, C. M., and Johnston, D. (1997). K^+ channel regulation of signal propagation in dendrites of hippocampal pyramidal neurons. *Nature*, 387(6636):869–875.

Hollmann, M., Hartley, M., and Heinemann, S. (1991). Ca^{2+} permeability of KA-AMPA–gated glutamate receptor channels depends on subunit composition. *Science*, 252(5007):851–853.

Holthoff, K., Zecevic, D., and Konnerth, A. (2010). Rapid time course of action potentials in spines and remote dendrites of mouse visual cortex neurons. *J Physiol*, 588:1085–1096.

Hopfield, J. J. and Tank, D. W. (1986). Computing with neural circuits: a model. *Science*, 233(4764):625–633.

Hu, H., Vervaeke, K., and Storm, J. F. (2002). Two forms of electrical resonance at theta frequencies, generated by M-current, h-current and persistent Na^{+} current in rat hippocampal pyramidal cells. *J Physiol*, 545:783–805.

Huntley, G. W., Vickers, J. C., and Morrison, J. H. (1994). Cellular and synaptic localization of NMDA and non-NMDA receptor subunits in neocortex: organizational features related to cortical circuitry, function and disease. *Trends Neurosci*, 17(12):536–543.

Isokawa, M., Avanzini, G., Finch, D. M., Babb, T. L., and Levesque, M. F. (1991). Physiologic properties of human dentate granule cells in slices prepared from epileptic patients. *Epilepsy Res*, 9(3):242–250.

Jaffe, D. B. and Carnevale, N. T. (1999). Passive normalization of synaptic integration influenced by dendritic architecture. *J Neurophysiol*, 82(6):3268–3285.

Jagadeesh, B., Wheat, H. S., and Ferster, D. (1993). Linearity of summation of synaptic potentials underlying direction selectivity in simple cells of the cat visual cortex. *Science*, 262(5141):1901–1904.

Jefferys, J. G. (1979). Initiation and spread of action potentials in granule cells maintained in vitro in slices of guinea-pig hippocampus. *J Physiol*, 289:375–388.

Jensen, O. and Lisman, J. E. (2000). Position reconstruction from an ensemble of hippocampal place cells: contribution of theta phase coding. *J Neurophysiol*, 83(5):2602–2609.

Jia, H., Rochefort, N. L., Chen, X., and Konnerth, A. (2010). Dendritic organization of sensory input to cortical neurons in vivo. *Nature*, 464(7293):1307–1312.

John, J. L. S., Rosene, D. L., and Luebke, J. I. (1997). Morphology and electrophysiology of dentate granule cells in the rhesus monkey: comparison with the rat. *J Comp Neurol*, 387(1):136–147.

Jung, H. Y., Mickus, T., and Spruston, N. (1997). Prolonged sodium channel inactivation contributes to dendritic action potential attenuation in hippocampal pyramidal neurons. *J Neurosci*, 17(17):6639–6646.

Jung, M. W. and McNaughton, B. L. (1993). Spatial selectivity of unit activity in the hippocampal granular layer. *Hippocampus*, 3(2):165–182.

Kamondi, A., Acsády, L., and Buzsáki, G. (1998). Dendritic spikes are enhanced by cooperative network activity in the intact hippocampus. *J Neurosci*, 18(10):3919–3928.

Kampa, B. M. and Stuart, G. J. (2006). Calcium spikes in basal dendrites of layer 5 pyramidal neurons during action potential bursts. *J Neurosci*, 26(28):7424–7432.

Kee, M., Wuskell, J., Loew, L., Augustine, G., and Sekino, Y. (2009). Imaging activity of neuronal populations with new long-wavelength voltage-sensitive dyes. *Brain Cell Biol*, 36(5-6):157–172.

Keller, B. U., Konnerth, A., and Yaari, Y. (1991). Patch clamp analysis of excitatory synaptic currents in granule cells of rat hippocampus. *J Physiol*, 435:275–293.

Kerchner, G. A. and Nicoll, R. A. (2008). Silent synapses and the emergence of a postsynaptic mechanism for LTP. *Nat Rev Neurosci*, 9(11):813–825.

Ketelaars, S. O., Gorter, J. A., van Vliet, E. A., da Silva, F. H. L., and Wadman, W. J. (2001). Sodium currents in isolated rat CA1 pyramidal and dentate granule neurones in the post-status epilepticus model of epilepsy. *Neuroscience*, 105(1):109–120.

Kim, J., Jung, S.-C., Clemens, A. M., Petralia, R. S., and Hoffman, D. A. (2007). Regulation of dendritic excitability by activity-dependent trafficking of the A-type K^+ channel subunit Kv4.2 in hippocampal neurons. *Neuron*, 54(6):933–947.

Kitamura, K., Judkewitz, B., Kano, M., Denk, W., and Häusser, M. (2008). Targeted patch-clamp recordings and single-cell electroporation of unlabeled neurons in vivo. *Nat Methods*, 5(1):61–67.

Koch, C. (1999). *Biophysics of computation: Information processing in single neurons*. Oxford University Press.

Koch, C., Poggio, T., and Torre, V. (1982). Retinal ganglion cells: a functional interpretation of dendritic morphology. *Philos Trans R Soc Lond B Biol Sci*, 298(1090):227–263.

Kole, M. H. P., Ilschner, S. U., Kampa, B. M., Williams, S. R., Ruben, P. C., and Stuart, G. J. (2008). Action potential generation requires a high sodium channel density in the axon initial segment. *Nat Neurosci*, 11(2):178–186.

Kron, M. M., Zhang, H., and Parent, J. M. (2010). The developmental stage of dentate granule cells dictates their contribution to seizure-induced plasticity. *J Neurosci*, 30(6):2051–2059.

Langmoen, I. A. and Andersen, P. (1983). Summation of excitatory postsynaptic potentials in hippocampal pyramidal cells. *J Neurophysiol*, 50(6):1320–1329.

Larimer, P. and Strowbridge, B. W. (2009). Representing information in cell assemblies: persistent activity mediated by semilunar granule cells. *Nat Neurosci*, 13(2):213–222.

Larkum, M. E., Nevian, T., Sandler, M., Polsky, A., and Schiller, J. (2009). Synaptic integration in tuft dendrites of layer 5 pyramidal neurons: a new unifying principle. *Science*, 325(5941):756–760.

Larkum, M. E., Watanabe, S., Nakamura, T., Lasser-Ross, N., and Ross, W. N. (2003). Synaptically activated Ca^{2+} waves in layer 2/3 and layer 5 rat neocortical pyramidal neurons. *J Physiol*, 549:471–488.

Larkum, M. E., Zhu, J. J., and Sakmann, B. (1999). A new cellular mechanism for coupling inputs arriving at different cortical layers. *Nature*, 398(6725):338–341.

Lawrence, J. J. and McBain, C. J. (2003). Interneuron diversity series: containing the detonation—feedforward inhibition in the CA3 hippocampus. *Trends Neurosci*, 26(11):631–640.

Leranth, C. and Hajszan, T. (2007). Extrinsic afferent systems to the dentate gyrus. *Prog Brain Res*, 163:63–84.

Leutgeb, J. K., Leutgeb, S., Moser, M.-B., and Moser, E. I. (2007a). Pattern separation in the dentate gyrus and CA3 of the hippocampus. *Science*, 315(5814):961–966.

Leutgeb, J. K., Leutgeb, S., Tashiro, A., Moser, E. I., and Moser, M.-B. (2007b). The encoding of novelty in the dentate gyrus and CA3 network. In *Society for Neuroscience Meeting Abstracts*.

Leutgeb, J. K. and Moser, E. I. (2007). Enigmas of the dentate gyrus. *Neuron*, 55(2):176–178.

Leutgeb, S., Leutgeb, J. K., Moser, M.-B., and Moser, E. I. (2005). Place cells, spatial maps and the population code for memory. *Curr Opin Neurobiol*, 15(6):738–746.

Li, L. S. (2007). Fluorescence probes for membrane potentials based on mesoscopic electron transfer. *Nano Lett*, 7(10):2981–2986.

Li, X. and Ascoli, G. A. (2006). Computational simulation of the input-output relationship in hippocampal pyramidal cells. *J Comput Neurosci*, 21(2):191–209.

Lipowsky, R., Gillessen, T., and Alzheimer, C. (1996). Dendritic Na^{+} channels amplify EPSPs in hippocampal CA1 pyramidal cells. *J Neurophysiol*, 76(4):2181–2191.

Liu, S. and Shipley, M. T. (2008). Intrinsic conductances actively shape excitatory and inhibitory postsynaptic responses in olfactory bulb external tufted cells. *J Neurosci*, 28(41):10311–10322.

Liu, Y. B., Lio, P. A., Pasternak, J. F., and Trommer, B. L. (1996). Developmental changes in membrane properties and postsynaptic currents of granule cells in rat dentate gyrus. *J Neurophysiol*, 76(2):1074–1088.

London, M. and Segev, I. (2001). Synaptic scaling in vitro and in vivo. *Nat Neurosci*, 4(9):853–855.

Lorente de Nó, R. (1934). Studies on the structure of the cerebral cortex II. Continuation of the study of the ammonic system. *J Psychol Neurol*, 46:113–177.

Lorente de Nó, R. (1935). The summation of impulses transmitted to the motoneurons through different synapses. *Am J Physiol*, 113:524–528.

Losonczy, A. and Magee, J. C. (2006). Integrative properties of radial oblique dendrites in hippocampal CA1 pyramidal neurons. *Neuron*, 50(2):291–307.

Losonczy, A., Makara, J. K., and Magee, J. C. (2008). Compartmentalized dendritic plasticity and input feature storage in neurons. *Nature*, 452(7186):436–441.

Lynch, M. A. (2004). Long-term potentiation and memory. *Physiol Rev*, 84(1):87–136.

Lømo, T. (1971). Patterns of activation in a monosynaptic cortical pathway: the perforant path input to the dentate area of the hippocampal formation. *Exp Brain Res*, 12(1):18–45.

Magee, J. C. (1998). Dendritic hyperpolarization-activated currents modify the integrative properties of hippocampal CA1 pyramidal neurons. *J Neurosci*, 18(19):7613–7624.

Magee, J. C. (1999). Dendritic I_h normalizes temporal summation in hippocampal CA1 neurons. *Nat Neurosci*, 2(6):508–514.

Magee, J. C. (2001). Dendritic mechanisms of phase precession in hippocampal CA1 pyramidal neurons. *J Neurophysiol*, 86(1):528–532.

Magee, J. C. and Cook, E. P. (2000). Somatic EPSP amplitude is independent of synapse location in hippocampal pyramidal neurons. *Nat Neurosci*, 3(9):895–903.

Magee, J. C. and Johnston, D. (1995a). Characterization of single voltage-gated Na^+ and Ca^{2+} channels in apical dendrites of rat CA1 pyramidal neurons. *J Physiol*, 487 (Pt 1):67–90.

Magee, J. C. and Johnston, D. (1995b). Synaptic activation of voltage-gated channels in the dendrites of hippocampal pyramidal neurons. *Science*, 268(5208):301–304.

Major, G., Polsky, A., Denk, W., Schiller, J., and Tank, D. W. (2008). Spatiotemporally graded NMDA spike/plateau potentials in basal dendrites of neocortical pyramidal neurons. *J Neurophysiol*, 99:2584–2601.

Markram, H. and Sakmann, B. (1994). Calcium transients in dendrites of neocortical neurons evoked by single subthreshold excitatory postsynaptic potentials via low-voltage-activated calcium channels. *Proc Natl Acad Sci U S A*, 91(11):5207–5211.

Marr, D. (1971). Simple memory: a theory for archicortex. *Philos Trans R Soc Lond B Biol Sci*, 262(841):23–81.

Mayer, M. L., Westbrook, G. L., and Guthrie, P. B. (1984). Voltage-dependent block by Mg^{2+} of NMDA responses in spinal cord neurones. *Nature*, 309(5965):261–263.

McDermott, C. M., Hardy, M. N., Bazan, N. G., and Magee, J. C. (2006). Sleep deprivation-induced alterations in excitatory synaptic transmission in the CA1 region of the rat hippocampus. *J Physiol*, 570:553–565.

McHugh, T. J., Jones, M. W., Quinn, J. J., Balthasar, N., Coppari, R., Elmquist, J. K., Lowell, B. B., Fanselow, M. S., Wilson, M. A., and Tonegawa, S. (2007). Dentate gyrus NMDA receptors mediate rapid pattern separation in the hippocampal network. *Science*, 317(5834):94–99.

McNaughton, B. L. and Morris, R. G. M. (1987). Hippocampal synaptic enhancement and information storage within a distributed memory system. *Trends Neurosci*, 10:408–415.

Megias, M., Emri, Z., Freund, T. F., and Gulyás, A. I. (2001). Total number and distribution of inhibitory and excitatory synapses on hippocampal ca1 pyramidal cells. *Neuroscience*, 102(3):527–540.

Mel, B. (1992). NMDA-based pattern discrimination in a modeled cortical neuron. *Neural Comput*, 4:502–517.

Mel, B. W. (1993). Synaptic integration in an excitable dendritic tree. *J Neurophysiol*, 70(3):1086–1101.

Mennerick, S., Chisari, M., Shu, H.-J., Taylor, A., Vasek, M., Eisenman, L. N., and Zorumski, C. F. (2010). Diverse voltage-sensitive dyes modulate $GABA_A$ receptor function. *J Neurosci*, 30(8):2871–2879.

Migliore, M., Hoffman, D. A., Magee, J. C., and Johnston, D. (1999). Role of an A-type K^+ conductance in the back-propagation of action potentials in the dendrites of hippocampal pyramidal neurons. *J Comput Neurosci*, 7(1):5–15.

Migliore, M. and Shepherd, G. M. (2002). Emerging rules for the distributions of active dendritic conductances. *Nat Rev Neurosci*, 3(5):362–370.

Mittelstaedt, M.-L. and Mittelstaedt, H. (1980). Homing by path integration in a mammal. *Naturwissenschaften*, 67:566–567.

Molter, C. and Yamaguchi, Y. (2008a). Entorhinal theta phase precession sculpts dentate gyrus place fields. *Hippocampus*, 18(9):919–930.

Molter, C. and Yamaguchi, Y. (2008b). Impact of temporal coding of presynaptic entorhinal cortex grid cells on the formation of hippocampal place fields. *Neural Netw*, 21(2–3):303–310.

Mori, M., Abegg, M. H., Gähwiler, B. H., and Gerber, U. (2004). A frequency-dependent switch from inhibition to excitation in a hippocampal unitary circuit. *Nature*, 431(7007):453–456.

Mori, M., Gähwiler, B. H., and Gerber, U. (2007). Recruitment of an inhibitory hippocampal network after bursting in a single granule cell. *Proc Natl Acad Sci USA*, 104(18):7640–7645.

Moser, E. I., Kropff, E., and Moser, M.-B. (2008). Place cells, grid cells, and the brain's spatial representation system. *Annu Rev Neurosci*, 31:69–89.

Moser, E. I. and Moser, M.-B. (2008). A metric for space. *Hippocampus*, 18(12):1142–1156.

Mouginot, D., Bossu, J. L., and Gähwiler, B. H. (1997). Low-threshold Ca^{2+} currents in dendritic recordings from Purkinje cells in rat cerebellar slice cultures. *J Neurosci*, 17(1):160–170.

Müller, C., Beck, H., and Remy, S. (2010). Feedback inhibitory control of excitatory signal integration in CA1 pyramidal neurons during theta-patterned pyramidal neuron firing. In *FENS Forum Abstracts*.

Muñoz, M. D., Núñez, A., and García-Austt, E. (1990). In vivo intracellular analysis of rat dentate granule cells. *Brain Res*, 509(1):91–98.

Narayanan, R. and Johnston, D. (2008). The h channel mediates location dependence and plasticity of intrinsic phase response in rat hippocampal neurons. *J Neurosci*, 28(22):5846–5850.

Nauta, W. J. H. and Feirtag, M. (1988). *Neuroanatomie. Eine Einführung.* Spektrum Akademischer Verlag.

Nettleton, J. S. and Spain, W. J. (2000). Linear to supralinear summation of AMPA-mediated EPSPs in neocortical pyramidal neurons. *J Neurophysiol*, 83(6):3310–3322.

Nevian, T., Larkum, M. E., Polsky, A., and Schiller, J. (2007). Properties of basal dendrites of layer 5 pyramidal neurons: a direct patch-clamp recording study. *Nat Neurosci*, 10(2):206–214.

Nimchinsky, E. A., Sabatini, B. L., and Svoboda, K. (2002). Structure and function of dendritic spines. *Annu Rev Physiol*, 64:313–353.

Nusser, Z. (2000). AMPA and NMDA receptors: similarities and differences in their synaptic distribution. *Curr Opin Neurobiol*, 10(3):337–341.

Nusser, Z. (2009). Variability in the subcellular distribution of ion channels increases neuronal diversity. *Trends Neurosci*, 32(5):267–274.

Nusser, Z. and Mody, I. (2002). Selective modulation of tonic and phasic inhibitions in dentate gyrus granule cells. *J Neurophysiol*, 87(5):2624–2628.

O'Keefe, J. and Dostrovsky, J. (1971). The hippocampus as a spatial map. Preliminary evidence from unit activity in the freely-moving rat. *Brain Res*, 34(1):171–175.

Palmer, L. M. and Stuart, G. J. (2009). Membrane potential changes in dendritic spines during action potentials and synaptic input. *J Neurosci*, 29(21):6897–6903.

Papp, G., Witter, M. P., and Treves, A. (2007). The CA3 network as a memory store for spatial representations. *Learn Mem*, 14(11):732–744.

Patton, P. E. and McNaughton, B. (1995). Connection matrix of the hippocampal formation: I. The dentate gyrus. *Hippocampus*, 5(4):245–286.

Pernia-Andrade, A. and Jonas, P. (2009). Synaptic activity in patch-clamp recorded dentate gyrus granule cells in vivo. In *Society for Neuroscience Meeting Abstracts*.

Poirazi, P., Brannon, T., and Mel, B. W. (2003). Pyramidal neuron as two-layer neural network. *Neuron*, 37(6):989–999.

Poirazi, P. and Mel, B. W. (2001). Impact of active dendrites and structural plasticity on the memory capacity of neural tissue. *Neuron*, 29(3):779–796.

Polsky, A., Mel, B. W., and Schiller, J. (2004). Computational subunits in thin dendrites of pyramidal cells. *Nat Neurosci*, 7(6):621–627.

Poolos, N. P. and Kocsis, J. D. (1990). Dendritic action potentials activated by NMDA receptor-mediated EPSPs in CA1 hippocampal pyramidal cells. *Brain Res*, 524(2):342–346.

Rall, W. (1962). Theory of physiological properties of dendrites. *Ann N Y Acad Sci*, 96:1071–1092.

Rall, W. and Rinzel, J. (1973). Branch input resistance and steady attenuation for input to one branch of a dendritic neuron model. *Biophys J*, 13(7):648–687.

Rapp, P. R. and Gallagher, M. (1996). Preserved neuron number in the hippocampus of aged rats with spatial learning deficits. *Proc Natl Acad Sci USA*, 93(18):9926–9930.

Remy, S., Csicsvari, J., and Beck, H. (2009). Activity-dependent control of neuronal output by local and global dendritic spike attenuation. *Neuron*, 61(6):906–916.

Remy, S. and Spruston, N. (2007). Dendritic spikes induce single-burst long-term potentiation. *Proc Natl Acad Sci USA*, 104(43):17192–17197.

Riazanski, V., Becker, A., Chen, J., Sochivko, D., Lie, A., Wiestler, O. D., Elger, C. E., and Beck, H. (2001). Functional and molecular analysis of transient voltage-dependent K^+ currents in rat hippocampal granule cells. *J Physiol*, 537:391–406.

Rinzel, J. and Rall, W. (1974). Transient response in a dendritic neuron model for current injected at one branch. *Biophys J*, 14(10):759–790.

Rolls, E. T. and Kesner, R. P. (2006). A computational theory of hippocampal function, and empirical tests of the theory. *Prog Neurobiol*, 79(1):1–48.

Rose, G., Diamond, D., and Lynch, G. S. (1983). Dentate granule cells in the rat hippocampal formation have the behavioral characteristics of theta neurons. *Brain Res*, 266(1):29–37.

Sacconi, L., Mapelli, J., Gandolfi, D., Lotti, J., O'Connor, R. P., D'Angelo, E., and Pavone, F. S. (2008). Optical recording of electrical activity in intact neuronal networks with random access second-harmonic generation microscopy. *Opt Express*, 16(19):14910–14921.

Scharfman, H. E. (1995). Electrophysiological evidence that dentate hilar mossy cells are excitatory and innervate both granule cells and interneurons. *J Neurophysiol*, 74(1):179–194.

Schiller, J., Major, G., Koester, H. J., and Schiller, Y. (2000). NMDA spikes in basal dendrites of cortical pyramidal neurons. *Nature*, 404(6775):285–289.

Schiller, J. and Schiller, Y. (2001). NMDA receptor-mediated dendritic spikes and coincident signal amplification. *Curr Opin Neurobiol*, 11(3):343–348.

Schiller, J., Schiller, Y., Stuart, G., and Sakmann, B. (1997). Calcium action potentials restricted to distal apical dendrites of rat neocortical pyramidal neurons. *J Physiol*, 505:605–616.

Schmidt-Hieber, C., Jonas, P., and Bischofberger, J. (2004). Enhanced synaptic plasticity in newly generated granule cells of the adult hippocampus. *Nature*, 429(6988):184–187.

Schmidt-Hieber, C., Jonas, P., and Bischofberger, J. (2007). Subthreshold dendritic signal processing and coincidence detection in dentate gyrus granule cells. *J Neurosci*, 27(31):8430–8441.

Schmidt-Hieber, C., Jonas, P., and Bischofberger, J. (2008). Action potential initiation and propagation in hippocampal mossy fibre axons. *J Physiol*, 586(7):1849–1857.

Schwindt, P. C. and Crill, W. E. (1995). Amplification of synaptic current by persistent sodium conductance in apical dendrite of neocortical neurons. *J Neurophysiol*, 74(5):2220–2224.

Seress, L. (1988). Interspecies comparison of the hippocampal formation shows increased emphasis on the regio superior in the Ammon's horn of the human brain. *J Hirnforsch*, 29(3):335–340.

Seress, L. and Frotscher, M. (1990). Morphological variability is a characteristic feature of granule cells in the primate fascia dentata: a combined Golgi/electron microscope study. *J Comp Neurol*, 293(2):253–267.

Seress, L. and Mrzljak, L. (1987). Basal dendrites of granule cells are normal features of the fetal and adult dentate gyrus of both monkey and human hippocampal formations. *Brain Res*, 405(1):169–174.

Shepherd, G. M., Brayton, R. K., Miller, J. P., Segev, I., Rinzel, J., and Rall, W. (1985). Signal enhancement in distal cortical dendrites by means of interactions between active dendritic spines. *Proc Natl Acad Sci USA*, 82(7):2192–2195.

Si, B. and Treves, A. (2009). The role of competitive learning in the generation of DG fields from EC inputs. *Cogn Neurodyn*, 3(2):177–187.

Sjöström, P. J., Rancz, E. A., Roth, A., and Häusser, M. (2008). Dendritic excitability and synaptic plasticity. *Physiol Rev*, 88(2):769–840.

Sjulson, L. and Miesenböck, G. (2008). Rational optimization and imaging in vivo of a genetically encoded optical voltage reporter. *J Neurosci*, 28(21):5582–5593.

Skaggs, W. E., McNaughton, B. L., Wilson, M. A., and Barnes, C. A. (1996). Theta phase precession in hippocampal neuronal populations and the compression of temporal sequences. *Hippocampus*, 6(2):149–172.

Smith, M. A., Ellis-Davies, G. C. R., and Magee, J. C. (2003). Mechanism of the distance-dependent scaling of Schaffer collateral synapses in rat CA1 pyramidal neurons. *J Physiol*, 548:245–258.

Softky, W. (1994). Sub-millisecond coincidence detection in active dendritic trees. *Neuroscience*, 58(1):13–41.

Solstad, T., Moser, E. I., and Einevoll, G. T. (2006). From grid cells to place cells: a mathematical model. *Hippocampus*, 16(12):1026–1031.

Spigelman, I., Yan, X. X., Obenaus, A., Lee, E. Y., Wasterlain, C. G., and Ribak, C. E. (1998). Dentate granule cells form novel basal dendrites in a rat model of temporal lobe epilepsy. *Neuroscience*, 86(1):109–120.

Spruston, N. and Johnston, D. (1992). Perforated patch-clamp analysis of the passive membrane properties of three classes of hippocampal neurons. *J Neurophysiol*, 67(3):508–529.

Spruston, N., Schiller, Y., Stuart, G., and Sakmann, B. (1995). Activity-dependent action potential invasion and calcium influx into hippocampal CA1 dendrites. *Science*, 268(5208):297–300.

Squire, L. R., Stark, C. E. L., and Clark, R. E. (2004). The medial temporal lobe. *Annu Rev Neurosci*, 27:279–306.

Stabel, J., Ficker, E., and Heinemann, U. (1992). Young CA1 pyramidal cells of rats, but not dentate gyrus granule cells, express a delayed inward rectifying current with properties of I_Q. *Neurosci Lett*, 135(2):231–234.

Staley, K. J., Otis, T. S., and Mody, I. (1992). Membrane properties of dentate gyrus granule cells: comparison of sharp microelectrode and whole-cell recordings. *J Neurophysiol*, 67(5):1346–1358.

Strecker, T. and Heinemann, U. (1993). Redistribution of K^+ channels into dendrites is unlikely to account for developmental down regulation of A-currents in rat dentate gyrus granule cells. *Neurosci Lett*, 164(1–2):209–212.

van Strien, N. M., Cappaert, N. L. M., and Witter, M. P. (2009). The anatomy of memory: an interactive overview of the parahippocampal-hippocampal network. *Nat Rev Neurosci*, 10(4):272–282.

Stuart, G., Spruston, N., Sakmann, B., and Häusser, M. (1997). Action potential initiation and backpropagation in neurons of the mammalian CNS. *Trends Neurosci*, 20(3):125–131.

Takahashi, H. and Magee, J. C. (2009). Pathway interactions and synaptic plasticity in the dendritic tuft regions of CA1 pyramidal neurons. *Neuron*, 62(1):102–111.

Tamamaki, N. (1997). Organization of the entorhinal projection to the rat dentate gyrus revealed by Dil anterograde labeling. *Exp Brain Res*, 116(2):250–258.

Tamamaki, N. and Nojyo, Y. (1993). Projection of the entorhinal layer II neurons in the rat as revealed by intracellular pressure-injection of neurobiotin. *Hippocampus*, 3(4):471–480.

Tamás, G., Szabadics, J., and Somogyi, P. (2002). Cell type- and subcellular position-dependent summation of unitary postsynaptic potentials in neocortical neurons. *J Neurosci*, 22(3):740–747.

Thompson, L. T. and Best, P. J. (1989). Place cells and silent cells in the hippocampus of freely-behaving rats. *J Neurosci*, 9(7):2382–2390.

Toni, N., Laplagne, D. A., Zhao, C., Lombardi, G., Ribak, C. E., Gage, F. H., and Schinder, A. F. (2008). Neurons born in the adult dentate gyrus form functional synapses with target cells. *Nat Neurosci*, 11(8):901–907.

Treves, A. and Rolls, E. T. (1992). Computational constraints suggest the need for two distinct input systems to the hippocampal CA3 network. *Hippocampus*, 2(2):189–199.

Trommald, M. and Hulleberg, G. (1997). Dimensions and density of dendritic spines from rat dentate granule cells based on reconstructions from serial electron micrographs. *J Comp Neurol*, 377(1):15–28.

Turner, R. W., Meyers, D. E., and Barker, J. L. (1989). Localization of tetrodotoxin-sensitive field potentials of CA1 pyramidal cells in the rat hippocampus. *J Neurophysiol*, 62(6):1375–1387.

Ujfalussy, B., Kiss, T., and Érdi, P. (2009). Parallel computational subunits in dentate granule cells generate multiple place fields. *PLoS Comput Biol*, 5(9):e1000500.

Valiante, T. A., Abdul-Ghani, M. A., Carlen, P. L., and Pennefather, P. (1997). Analysis of current fluctuations during after-hyperpolarization current in dentate granule neurones of the rat hippocampus. *J Physiol*, 499:121–134.

Vervaeke, K., Hu, H., Graham, L. J., and Storm, J. F. (2006). Contrasting effects of the persistent Na^+ current on neuronal excitability and spike timing. *Neuron*, 49(2):257–270.

Vuksic, M., Turco, D. D., Orth, C. B., Burbach, G. J., Feng, G., Müller, C. M., Schwarzacher, S. W., and Deller, T. (2008). 3D-reconstruction and functional properties of GFP-positive and GFP-negative granule cells in the fascia dentata of the Thy1-GFP mouse. *Hippocampus*, 18(4):364–375.

Wei, D. S., Mei, Y. A., Bagal, A., Kao, J. P., Thompson, S. M., and Tang, C. M. (2001). Compartmentalized and binary behavior of terminal dendrites in hippocampal pyramidal neurons. *Science*, 293(5538):2272–2275.

Wen, Q., Stepanyants, A., Elston, G. N., Grosberg, A. Y., and Chklovskii, D. B. (2009). Maximization of the connectivity repertoire as a statistical principle governing the shapes of dendritic arbors. *Proc Natl Acad Sci USA*, 106(30):12536–12541.

West, M. J., Slomianka, L., and Gundersen, H. J. (1991). Unbiased stereological estimation of the total number of neurons in the subdivisions of the rat hippocampus using the optical fractionator. *Anat Rec*, 231(4):482–497.

Williams, R. S. and Matthysse, S. (1983). Morphometric analysis of granule cell dendrites in the mouse dentate gyrus. *J Comp Neurol*, 215(2):154–164.

Williams, S. R. and Stuart, G. J. (2000). Site independence of EPSP time course is mediated by dendritic I_h in neocortical pyramidal neurons. *J Neurophysiol*, 83(5):3177–3182.

Williamson, A., Spencer, D. D., and Shepherd, G. M. (1993). Comparison between the membrane and synaptic properties of human and rodent dentate granule cells. *Brain Res*, 622(1–2):194–202.

Wilson, C. J. and Park, M. R. (1989). Capacitance compensation and bridge balance adjustment in intracellular recording from dendritic neurons. *J Neurosci Methods*, 27(1):51–75.

Wong, R. K., Prince, D. A., and Basbaum, A. I. (1979). Intradendritic recordings from hippocampal neurons. *Proc Natl Acad Sci USA*, 76(2):986–990.

Ye, G.-L., Yi, S., Gamkrelidze, G., Pasternak, J. F., and Trommer, B. L. (2005). AMPA and NMDA receptor-mediated currents in developing dentate gyrus granule cells. *Brain Res Dev Brain Res*, 155(1):26–32.

Zhang, L., Valiante, T. A., and Carlen, P. L. (1993). Contribution of the low-threshold T-type calcium current in generating the post-spike depolarizing afterpotential in dentate granule neurons of immature rats. *J Neurophysiol*, 70(1):223–231.

Zhou, W.-L., Yan, P., Wuskell, J. P., Loew, L. M., and Antic, S. D. (2008). Dynamics of action potential backpropagation in basal dendrites of prefrontal cortical pyramidal neurons. *Eur J Neurosci*, 27(4):923–936.

C. Contributions

The double branch experiments (fig. 3.14) were performed by Dr. Stefan Remy.